Quantitative Hemodynamics using Magnetic Resonance Imaging, Computational Fluid Dynamics and Physics-informed Neural Network

DISSERTATION

to acquire the doctoral degree in mathematics and natural science
"Doctor rerum naturalium"
at the Georg-August-Universität Göttingen

in the doctoral degree program Physics

of Georg-August University School of Sciences (GAUSS)

submitted by

Dandan Ma
from Hegang, China
Göttingen, 2023

Thesis Advisory Committee:

Prof. Dr. Martin Uecker
Institute of Diagnostic and Interventional Radiology
University Medical Center Göttingen

Prof. Dr. Ulrich Parlitz
Biomedical Physics Group
Max Planck Institute of Dynamics and Self-Organization

Prof. Dr. Susann Boretius
Functional Imaging Laboratory
German Primate Center

Members of the Examination Board:

Reviewer : **Prof. Dr. Martin Uecker**
Second Reviewer : **Prof. Dr. Stefan Klumpp**
Institute for Dynamics of Complex Systems
Georg August University of Göttingen

Further members of the Examination Board:

Prof. Dr. Jörg Enderlein
III Institute of Physics
Georg August University of Göttingen

Prof. Dr. Andreas Dillmann
Institute of Aerodynamics and Flow Technology
German Aerospace Center
Prof. Dr. Ulrich Parlitz
Prof. Dr. Susann Boretius
Date of the oral examination: 03.05.2023

Contents

List of Abbreviations

CVD	Cardiovascular Diseases
MRI	Magnetic Resonance Imaging
RF	Radiofrequency
FID	Free Induction Decay
PC MRI	Phase Contract MRI
CFD	Computational Fluid Dynamics
NSE	Navier Stokes Equations
DNS	Direct Numerical Simulation
RANS	Reynolds Averaged Navier Stokes
LES	Large Eddy Simulation
LBM	Lattice Boltzmann Method
PINN	Physics Informed Neural Network
BC	Boundary Condition
CoA	Coarctation of Aorta
WSS	Wall Shear Stress
CT	Computed Tomography
US	Ultra Sound
ESS	Endothelial Shear Stress
ML	Machine Learning
NN	Neural Network
PINN	Physics-Informed Neural Network
PDE	Partial Differential Equation
AD	Automatic Differentiation
AME	Adaptive Moment Estimation
CAs	Cerebral Aneurysms

AAAs	Abdominal Aortic Aneurysms
TKE	Turbulence Kinetic Energy
SGS	Subgrid-scale

Chapter 1

Introduction

Up to 17 million people worldwide die from cardiovascular disease (CVD) each year, accounting for approximately 31% of global deaths [87]. Research on the mechanisms of CVD as well as new treatments involves many disciplines such as physics, medicine, biology, and computer. In this dissertation, I focus on arterial hemodynamics using aortic flow as an example. New strategies combining fluid physics, medical imaging, computer science and neural network (NN) are proposed, to improve our understanding of hemodynamics and guide personalized stenting in aortic coarctation.

In this introductory chapter, I firstly present an overview of hemodynamics (Section 1.1), and then summarize its corresponding methodologies (Section 1.2). Section 1.3 describes the arterial hemodynamics related diseases and provides a literature review over the state-of-the art. Finally, Section 1.4 gives the structure of this work.

1.1 Hemodynamics

The cardiovascular system, consisting of the arteries, veins, heart, capillaries and flowing blood, is shown in Figure 1.1. It is considered to be a closed circulatory vascular system, hence the name circulatory system. The cardiovascular system supplies oxygen, hormones, and nutrients to the body's organs and tissues through blood flow, and transports waste products from tissue metabolism to the excretory organs. This circulatory system is the basis for the body's environmental homeostasis, metabolism and maintenance of normal life activities [110]. In recent years, CVD, including heart disease and vascular disease, are threatening human health and have become the leading cause of human death worldwide [106, 84]. Thus, the study of CVD has attracted increasing attention [130, 77]. The three-dimensional and multi-scale nature of the structure of the cardiovascular system, and blood flow therein, are very complex. Blood flow in the body is usually laminar. However, in some cases, such as narrow vessels or ventricular chambers with complex shapes that result in a relatively low critical Reynolds number (Re), blood flow may undergo transition from laminar to turbulent or even become fully turbulent.

Hemodynamics refers to the dynamics of blood flow. It is the study of the causes, conditions, states and various influences of blood flow in the circulatory system

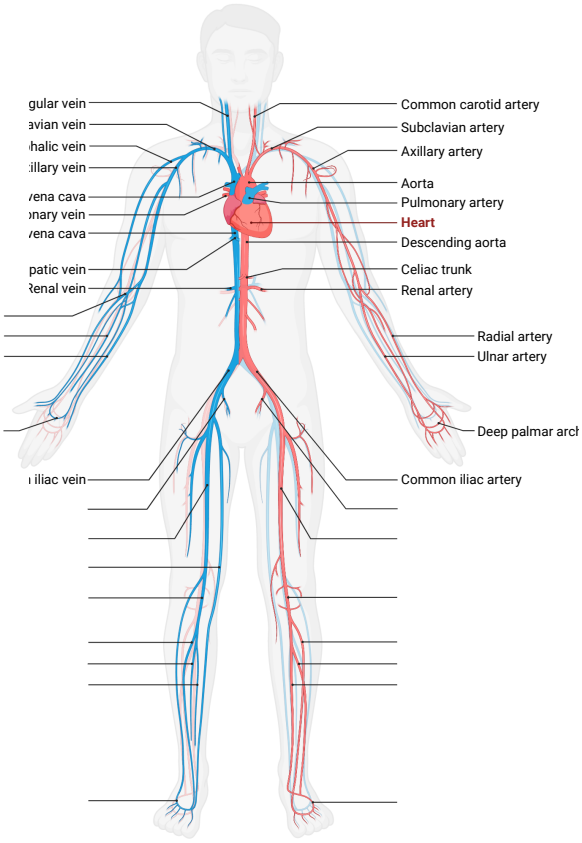

FIGURE 1.1: A sketch of the human circulatory system.

based on fluid mechanics. It is very useful in understanding blood flow patterns, their physiological significance and the relation to diseases [92, 114]. The circulatory system has many characteristics compared to other general hydrodynamic systems. First, the heart is a complex "pump" controlled by the neurohumoral system, which periodically pumps blood into arteries and then delivers it to various organs of the body through flexible tubes with many branches. Secondly, blood is a suspension containing a large number of blood cells, and in most arteries it exhibits the characteristics of a non-Newtonian viscous fluid. From a fluid dynamics perspective, hemodynamics is the study of the flow parameters (flow rate, velocity, pressure, pattern, viscosity, etc.) of the human circulatory system under physiological and pathological conditions [133]. Hemodynamics can be specifically divided into arterial system hemodynamics, cardiac hemodynamics, venous system hemodynamics, and microcirculatory hemodynamics.

1.2 Methodologies

Traditional quantitative methods for measuring hemodynamics include two main categories: experimental measurements and numerical modeling. In recent years, due to the development of modern computers, Machine Learning (ML) has been used as a third category by some researchers. Here, I provide a brief introduction to

these methods. More details, especially their physical and mathematical basis, can be found in Chapter 2.

- **Experimental Measurements**

  In addition to invasive measurement methods, such as measuring pulse pressure in the artery by inserting a cannula or catheter, here I focus on non-invasive measurement methods using medical imaging techniques, especially magnetic resonance imaging (MRI).

  Several non-invasive methods have been used to provide reliable structural information of cardiovascular system and blood flow therein. They are ultrasound (US), computed tomography (CT), MRI and digital subtraction imaging (DSA). Therein, MRI is one of the safe, fast and accurate clinical diagnostic methods. The biggest advantage of MRI over regular X-rays or CT is that it does not cause any harm to the human body. As a result, MRI is now widely used for diagnosis, therapeutic process monitoring and biomedical research [65, 73].

  In terms of blood flow measurements, on the one hand, the observation of in vitro flow characteristics using particle imaging velocimetry (PIV) can be applied in experiments with realistic structural models of normal and diseased blood vessels obtained by three-dimensional printing of vascular models [54, 100, 9]. On the other hand, quantitative measurements of blood flow can also be performed by MRI, in addition to obtaining anatomical information. Phase contrast MRI (PC MRI) measures blood flow using the phase changes produced by blood flow and is widely used in the study of cardiovascular diseases [71, 118]. By using some post-processing techniques, blood flow can be visualized locally and globally. In addition, some other hydrodynamic metrics such as velocity, pressure drop, wall shear stress (WSS) and energy loss can be calculated from the blood flow data. This can be of great value for physicians to guide the treatment of some cardiovascular diseases [33, 97]. However, flow MRI still has some limitations, generally caused by experimental techniques and post-processing tools. For example, the images contain acquisition noise and limited spatio-temporal resolution, which will affect the accuracy of quantitative blood flow analysis. In particular, the errors occurring near the blood-vessel boundary can bias the calculation of WSS, which is determined by the velocity gradient near the vessel wall. In addition, the timing of the measurements still needs to be optimized [26, 135, 105].

- **Numerical Modeling**

  With the rapid development of high performance computers, numerical modeling, especially computational fluid dynamics (CFD) has been widely adopted in the study of hemodynamics.

In CFD, the governing equations of blood flow are solved numerically, with realistic geometric boundaries based on medical images [86, 112, 111]. As CFD can provide high fidelity flow information, it has been adopted for hemodynamic studies. However, the accuracy of numerical results obtained by CFD depends on many factors, such as geometry, model pre-processing, mesh generation, numerical methods, boundary conditions, turbulence models, and post-processing of simulation results. In general, CFD for hemodynamics is time consuming and requires specialized knowledge. On the other hand, CFD-based hemodynamic studies sometimes use flow information obtained by MRI as boundary conditions. Therefore, the accuracy of flow MRI data is also a decisive condition for the numerical solution of blood flow.

- **Machine Learning**

  In recent years, ML has been considered as a new avenue for hemodynamic studies. For example, it can provide accurate physical models for CFD and evaluate automatically arterial hemodynamic characteristics. NN-based medical image segmentation and automatic generation of high-quality computational meshes have addressed the drawbacks of traditional CFD simulation in terms of difficult and time-consuming pre-processing [67, 126, 48, 143]. Using CFD results as training data, the trained NN can accomplish rapid estimation of the flow distribution and the pressure in the thoracic aorta [66].

  However, due to the complexity of the circulatory system structure and the uncertainty of the blood flow conditions, to build data-driven NN is challenging in personalized medicine, especially when the training samples are limited. Alternatively, Raissi et al. [102] proposed physics-informed NN (PINN). It solves flow problems within a NN framework by approximating reference training data and satisfying the basic flow governing equations. Compared to CFD, PINN does not require precise boundary conditions or even exact geometry, thus shows flexibility in hemodynamic studies. Some researchers have extended and refined PINN, making it capable of handling more complex flows. For example, Xu et al. [142] extended PINN for turbulent flow by introducing an artificial viscosity in the parameterized governing equations and demonstrated the capability of PINN in data assimilation. PINN is gradually being used in conjunction with traditional techniques for hemodynamic studies. Raissi et al. [61] used flow MRI data for arterial blood pressure prediction with PINN. In addition, the correlation between blood flow velocity, pressure and vessel cross-sectional area is illustrated in a one-dimensional model. Gao et al. [37] predicted two-dimensional blood flow and further verified that PINN can effectively improve image quality by comparing the velocity magnitude obtained from CFD.

On the one hand, these three categories of methods can be validated against each other to demonstrate their validity. On the other hand, **based on the strengths and**

weaknesses of these methods, they can be coupled and used simultaneously for hemodynamic studies. This is the main idea of this dissertation.

1.3 Arterial System Hemodynamics

This subsection provides a review of arterial hemodynamic studies using the methods mentioned above.

In the cardiovascular system, lesions of the arterial system often occur in the cerebral arteries, the heart, the left coronary artery and various parts of the aorta (such as the bifurcation, the ascending and descending segments of the aorta). Common arterial system hemodynamic disorders include atherosclerosis, aneurysms, and stenosis. The suggested treatments for arterial system include stenting and bypass graft surgery [120, 39]. In recent years, hemodynamic studies in normal and pathological states, using experimental measurement, CFD modeling and NN, have become a focus of interest.

Atherosclerosis (AS) is a disease in which "yellow atheromatous" lipids are deposited in the inner walls of the arteries, causing damage to the vessel walls and narrowing of the arteries. By determining the relationship between plaque formation and progression in atherosclerosis, a deeper understanding of the psychophysiology of coronary artery disease has been achieved, offering the opportunity for highly selective preemptive interventions in the future [20, 19, 132]. Stone et al. obtained the flow field by solving the basic equations of fluid dynamics in arterial anatomy reconstructed from images obtained by US and angiography. By assessing endothelial shear stress (ESS), progressive atherosclerosis and outward remodeling were found in areas of low ESS, and outward remodeling occurred in areas of increased ESS [123]. Strecker et al. investigated the relationship between carotid geometric parameters and WSS in patients at high risk for cardiovascular disease. In vivo evaluation of three-dimensional fluid structures obtained at the carotid bifurcation by flow MRI revealed that the geometric parameters of the carotid bifurcation can effectively help physicians diagnose carotid plaque production in patients [124]. Ziegler et al. investigated MRI data from patients with atherosclerosis at the carotid bifurcation and studied the relationship between WSS, turbulent kinetic energy (TKE) near the vessel wall, and vessel geometry. It was concluded that there was a strong correlation between WSS and TKE, while the diameter and bifurcation angle of the vessel had little effect on TKE [145].

An aneurysm is an enlargement of the arterial wall due to a lesion or injury to the arterial wall. It is an arterial lesion that occurs anywhere in the arterial system, such as the cerebral arteries, the main arteries of the limbs, the aorta, and the carotid arteries, and is characterized by a swollen, pulsating mass [130, 18, 52, 29, 89]. Basombrio et al. proposed that the non-Newtonian properties of blood plaid a very critical role in accomplishing the modeling of aneurysms, especially in the slower velocity region. And, several non-Newtonian models have been proposed

and widely used in the simulation of cerebral aneurysm blood flow [10]. Cebral et al. qualitatively investigated the correlation of complex flow patterns in cerebral aneurysms with prior aneurysm rupture by using qualitative analysis within cerebral aneurysms obtained from images [18]. Nixon et al. showed through computer simulations that abnormal levels of WSS contributed to the formation and development of intracranial aneurysms. In addition, disturbed blood flow and low WSS have been found to make patients more susceptible to extracranial atherosclerosis, such as carotid artery disease [77]. Meng et al. surgically created new branches in the carotid vessels of dogs. In vivo angiography and CFD simulations were performed to observe blood flow at the point of bifurcation. Proliferative and destructive remodeling was observed, and flow regions with high gradients of WSS and high WSS were found to be high risk factors for aneurysmal remodeling [74]. Katsuyuki et al. evaluated the relationship between hemodynamic parameters (WSS and relative wall strain) and aneurysm structure based on intra-aortic pressure conduction, periaortic US flowmetry, and WSS. It was found that high flow rates stimulated the proliferation of endothelial and smooth muscle cells in experimental medium rat aneurysms, which in turn may enhance aortic integrity and limit aneurysm development [47]. White et al. performed numerical simulations of blood flow within the patient's aneurysm at rest and during exercise. Based on three geometric models of the patient's aorta obtained by MRI, they identified areas of low flow and even stagnant blood flow within the aneurysm, which were reduced during the patient's exercise [139, 32]. Raissi et al. completed a quantitative hemodynamic study of a patient-specific three-dimensional intracranial aneurysm using PINN, with the concentration field generated by CFD data as data constraint. The flow field predicted by PINN was found to match the reference field in such a complex geometric model [101]. Arzani et al. [6] completed the prediction of hemodynamics and WSS near the vessel wall within the framework of PINN in an idealized aneurysm model, using a small amount of flow fields obtained by CFD as constraint data.

The treatment of atherosclerosis and aneurysms, as well as other diseases that cause localized narrowing of the arteries, can often be achieved by improving the flow path through stenting or bypass grafting [5, 28, 38]. Brindise et al. performed an experimental study of the hemodynamics at the coronary bifurcation of the stent in vitro. Velocity measurements were performed using PIV on three types of stent implanted vessels and hemodynamic parameters were calculated to assess the effect of different stents on blood flow [15]. Frauenfelder et al. quantitatively studied the hemodynamics of abdominal aortic aneurysms before and after stenting. In the numerical simulations, the fluid structure interaction (FSI) technique was used by considering the interaction between the deformed vessel wall and the blood flow, i.e. solving the fluid equation and the solid equation in each time step. It was verified that the streamline under experimental and numerical matched. In the aorta after stent placement, numerical simulations showed a reduction in WSS and a decrease in turbulence [35]. Tsukui et al. established an in vitro test rig to assess the

effectiveness of long-term distal anastomoses and discussed blood flow patterns. CFD was used to simulate hemodynamics in the distal anastomotic stoma based on the 3D geometry reconstructed from CT scan. A longer distal anastomosis technique was identified to reduce blood flow energy loss due to factors such as smaller angles and smooth graft curvature [134].

1.4 Structure of the Dissertation

Among the methods mentioned in Section 1.2, MRI, CFD and PINN have been used to study hemodynamics. As listed in Section 1.3, most of these studies have used only one of them. Of these, MRI allows direct access to flow field and geometric information; however, it has difficulties in measuring complex flows such as flow with recirculation and turbulent flow, and cannot be used to predict surgical outcomes. CFD allows direct solution of the physical equations and can be used for in silico experiment, but requires accurate input of boundary and initial conditions. PINN is constrained by both data and physical equations; it is still under development and needs validation, especially for hemodynamics.

By combining experimental measurement, numerical modeling and physical principles, particularly MRI, CFD and PINN, with each other, we can take advantages of each method. As a result, we can more effectively quantify hemodynamics and predict the outcome of surgical protocols.

In this dissertation, I propose two strategies that combine fluid physics, medical imaging, computer modeling, and PINN, and apply them to image-based in silico stent implantation (Chapter 3) and aortic blood flow prediction (Chapter 4), as shown in Figure 1.2. More details are as follows:

In Chapter 2, physical principles of MRI, CFD and PINN are described. These methods are further merged and implemented in studies of hemodynamics in Chapter 3 and Chapter 4.

In Chapter 3, a new strategy, combining MRI and CFD, for personalized stent intervention in aortic coarctation is proposed. To validate the accuracy of CFD, I firstly perform numerical simulations using different turbulence modeling methods and compare the numerical results with experimental data from flow MRI. The validated CFD method is further used to study the blood flows within virtually deformed aortic geometries, and to guide stent implantation.

In Chapter 4, a new strategy to accomplish blood flow prediction by combing MRI and PINN is proposed. This strategy overcomes the weaknesses of MRI and CFD for hemodynamics that emerged in Chapter 3. Prediction of both laminar and turbulent blood flows with PINN in 3D printed idealized and realistic aortic geometries are performed. Flow data and geometric information from the MRI are considered as inputs of the training. The effectiveness of the strategy for blood flow prediction is also discussed.

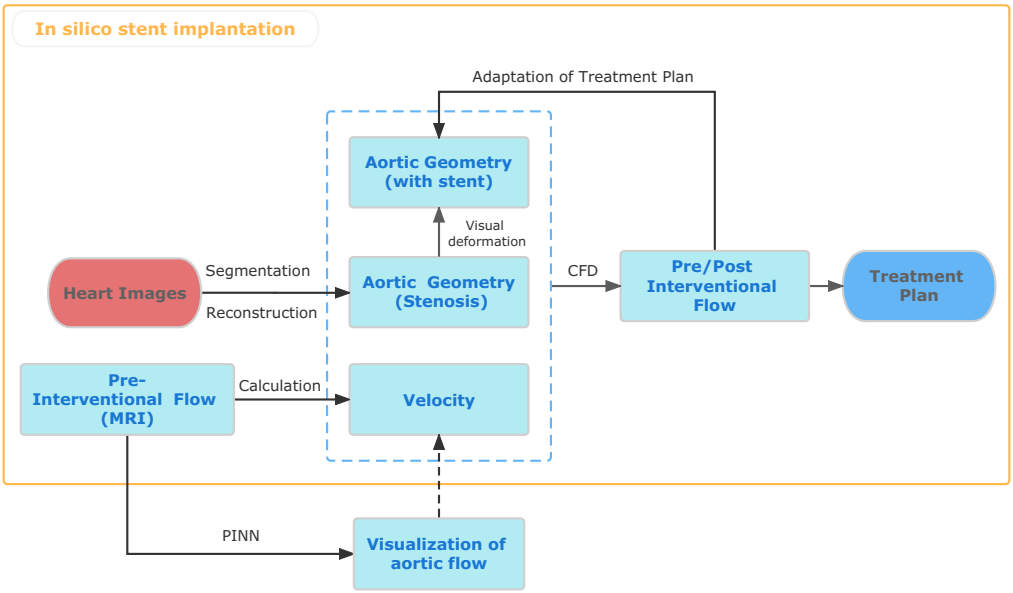

FIGURE 1.2: The main structure of this dissertation. Combing fluid physics, medical imaging, numerical modeling and NN, this dissertation focuses on the quantitative understanding of hemodynamics and its application in stent planning. Two main parts were completed. The first one is virtual stent implantation (in the yellow box), while the second one is image-based aortic hemodynamic prediction with PINN.

Finally, Chapter 5 summarizes the conclusions of the present dissertation and provides an outlook for future work.

Chapter 2

Principle of Hemodynamic Methodologies

As mentioned in Chapter 1, three methods, including experimental measurement (MRI), numerical modeling (CFD) and machine learning (PINN) are involved in this study. This chapter describes these methods from a physical point of view, providing the theoretical basis for Chapters 3 and 4. Section 2.1 describes the principles of MRI, PC MRI and introduces the experimental setups. Section 2.2 outlines the governing equations for fluid flows, numerical approaches for turbulence modeling, and the lattice Boltzmann method (LBM) used for CFD simulations. Section 2.3 describes PINN based on machine learning and neural network, and introduces the optimization algorithms and auto differentiation (AD) used in PINN.

2.1 Magnetic Resonance Imaging

This section is based on Refs. [141, 137, 125]. It is a general introduction of MRI and PC MRI.

2.1.1 Basics of MRI

MRI is a technique based on the interaction of nuclear magnetic moments generated by nuclear spins with an external magnetic field, and it pertains to the theory of nuclear magnetic resonance (NMR). In clinical studies, hydrogen nuclei (positively charged protons) are commonly used because they are abundant in the human body.

The spin of each hydrogen proton generates a small magnetic field, and the relationship between the magnetic moment $\boldsymbol{\mu}$ and the spin angular momentum $\boldsymbol{J}$ is

$$\boldsymbol{\mu} = \gamma \boldsymbol{J} \tag{2.1}$$

where γ is the gyromagnetic ratio. Due to the thermal random motion, the direction of the spin is random. The sum of the magnetic moments of all hydrogen nuclei forms the net magnetization vector in MRI. When there is no external magnetic field, the net magnetization vector is zero. When the proton is placed in a static external magnetic field, the proton spins can be aligned parallel or anti-parallel to the external

field, corresponding to the low and high energy states, respectively. The energies E_p in low energy state and E_{anti-p} high energy state in are:

$$E_p = -\gamma\frac{\hbar}{2}B_0, E_{anti-p} = \gamma\frac{\hbar}{2}B_0 \tag{2.2}$$

where $\hbar = h/2\pi$ and h is Planck's constant. B_0 is the strength of the external magnetic field.

In thermodynamic equilibrium, more spins will be in low energy state, creating macroscopic magnetization $\boldsymbol{M}$ in the same direction as the external field. The magnitude of $\boldsymbol{M}$ is

$$|\boldsymbol{M}| = \frac{\gamma^2\hbar^2 N_s}{4K_b T}B_0 \tag{2.3}$$

here K_b, N_s and T represent the Boltzmann constant, the number of spins and the temperature respectively. This shows that the magnitude of $\boldsymbol{M}$ is proportional to N_s and B_0.

In addition, the proton will move like a gyroscope around the direction of the external magnetic field, which is called precession and satisfies Larmor's law:

$$\omega_0 = \gamma B_0 \tag{2.4}$$

where ω_0 is the precession frequency.

- **Excitation**

  If a radiofrequency (RF) field $\boldsymbol{B_1}$ is added to excite the spins, which has the same frequency ω_0 as the proton, NMR occurs. The addition of $\boldsymbol{B_1}$, on the one hand, causes the transfer of energy and the proton jumps from the low energy level to the high energy state, causing a subsequent decrease in the longitudinal magnetic field strength. Taking Figure 2.1 as an example, the flip angle describing the rotation of the magnetization vector, is:

  $$\alpha = \gamma\int_0^{T_{RF}} B_1(t)dt \tag{2.5}$$

  where T_{RF} is the duration of pulse and the direction of $\boldsymbol{B_1}$ is perpendicular to z axis. After the application of RF, the component M_{xy} of the magnetized in $x-y$ plane precesses around the z axis. An oscillating signal, also known as an MRI signal, is induced by a magnetic field that varies with time. It is received and further used to detect and quantify the density of proton spin.

- **Relaxation**

  When the RF pulse disappears, the resonant hydrogen protons slowly return to their original orientation and amplitude, i.e., the thermal equilibrium state. This process is called "relaxation".

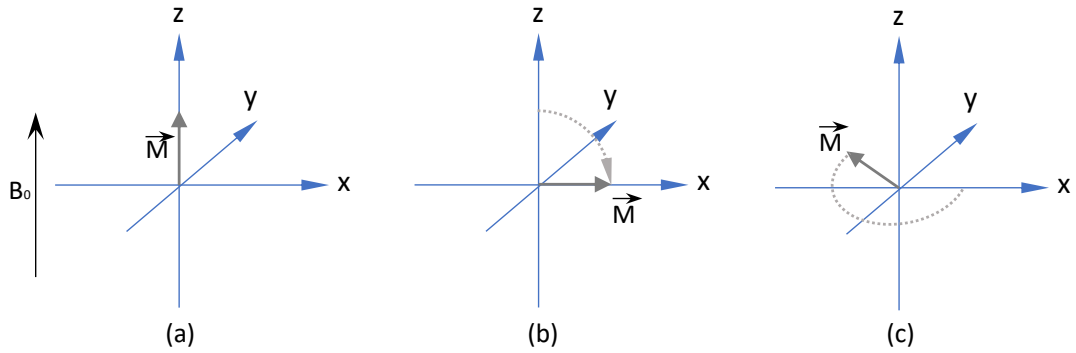

FIGURE 2.1: Schematic diagram of RF pulsed NMR experiment. (a), (b) and (c) represent "Equilibrium", "Excitation" and "Precession", respectively

The macroscopic magnetization $\boldsymbol{M} = (M_x, M_y, M_z)$ during excitation and relaxation can be expressed as Bloch equation:

$$\frac{d}{dt}\boldsymbol{M} = \gamma \boldsymbol{M} \times \boldsymbol{B} + \begin{pmatrix} -\frac{1}{T_2} M_x \\ -\frac{1}{T_2} M_y \\ \frac{M_{eq} - M_z}{T_1} \end{pmatrix} \tag{2.6}$$

where T_1, T_2 are the spin-lattice relaxation time and the spin-spin relaxation time respectively. They describe the relaxation of the longitudinal (z axis) magnetization and the loss of transversal ($x - y$ plane) magnetization. $M_\perp$ is introduced for the magnetization in $x - y$ plane, after RF excitation, the changes of magnetization according to:

$$M_z(t) = M_{eq}(1 - e^{-t/T_1}) \tag{2.7}$$

$$M_\perp(t) = M_{eq} e^{-t/T_2} \tag{2.8}$$

where M_{eq} is the equilibrum magnetization. In addition to the energy exchange with the environment, the decrease of the transverse magnetization is also influenced by the energy changes between spins, so that T_2 is smaller than T_1. Due to the dependence of T_1 and T_2 on individual materials, they can be used to differentiate human tissues in clinical MRI.

If two-dimensional or three-dimensional imaging is to be achieved, signals from different spatial locations need to be differentiated. Thus spatial encoding is introduced and performed by using additional gradient fields in addition to the main magnetic field. For example, applying gradient fields $G_x(t)$, $G_y(t)$ in the x and y direction, Larmor frequency and the transverse magnetization become:

$$\omega_\perp = \gamma \boldsymbol{G}(t) \cdot \boldsymbol{r} = \gamma(xG_x(t) + yG_y(t)) \tag{2.9}$$

$$M_{\perp}(\boldsymbol{r},t) = M_0(\boldsymbol{r}) \cdot e^{-i(\omega_0 t + \phi(\boldsymbol{r},t))} \tag{2.10}$$

here, the phase evolution ϕ is related to the time integral of the gradient field $\boldsymbol{G}$:

$$\phi(\boldsymbol{r},t) = \gamma \int_0^t \boldsymbol{G}(\tau)d\tau \cdot \boldsymbol{r} = 2\pi \boldsymbol{k}(t) \cdot \boldsymbol{r} \tag{2.11}$$

here, $\boldsymbol{k}(t)$ is the k-space trajectory:

$$\boldsymbol{k}(t) := \frac{\gamma}{2\pi} \int_0^t \boldsymbol{G}(\tau)d\tau \tag{2.12}$$

In MRI, the transverse magnetization is integrated and the real-valued signal detected by the coil is calculated in the entire volume.

$$\mathbb{R}\int M_{\perp}(\boldsymbol{r},t)d\boldsymbol{r} = \mathbb{R}\int M_{\perp}(\boldsymbol{r},0)e^{-2\pi i \boldsymbol{k}\cdot\boldsymbol{r}}e^{-i\omega_0 t}d\boldsymbol{r} \tag{2.13}$$

By quadrature demodulation, $e^{-i\omega_0 t}$ is removed. Assuming that the initial magnetization $M_{\perp}(\boldsymbol{r},0)$ is proportional to the spin density $\rho(\boldsymbol{r},0)$, the MRI-received signal $S(t)$ can be written:

$$S(t) = a \cdot \int \rho(\boldsymbol{r})e^{-2\pi i \boldsymbol{k}(\boldsymbol{t})\cdot\boldsymbol{r}}d\boldsymbol{r} \tag{2.14}$$

where a is a constant. Equation 2.14 shows that $S(t)$ associated with the Fourier transform of $\rho(\boldsymbol{r})$(the proton density).

2.1.2 Phase Contrast MRI

The basic principle of PC MRI is to use the proportional relationship between velocity and phase difference to achieve quantitative measurements of the blood flow velocity. In Equation 2.11, $\boldsymbol{r}$ can be defined as:

$$\boldsymbol{r} = \boldsymbol{r}_0 + \boldsymbol{v}_r\tau + \frac{1}{2}\boldsymbol{a}_r\tau^2 + \dots \tag{2.15}$$

where $\boldsymbol{r}_0$, $\boldsymbol{v}_r$ and $\boldsymbol{a}_r$ are the initial position, velocity and acceleration of the spin respectively.

When only the static and y-direction spins are considered, Equation 2.11 can be written as follows:

$$\phi = \gamma y_0 \int_0^t G_y(\tau)d\tau + \gamma v_y \int_0^t G_y(\tau)\tau d\tau + \gamma\frac{a_y}{2}\int_0^t G_y(\tau)\tau^2 d\tau \cdots \tag{2.16}$$

It can be simplified to:

$$\phi = \gamma(y_0 M_0 + v_y M_1) \tag{2.17}$$

where M_0 and M_1 are zeroth-moment and first-moment of the y-gradient.

When a bipolar velocity-encoded gradient is applied, as shown in Figure 2.2, the gradient area of the waveform is zero at the zeroth moment, i.e., $M_0 = 0$. And M_1 is

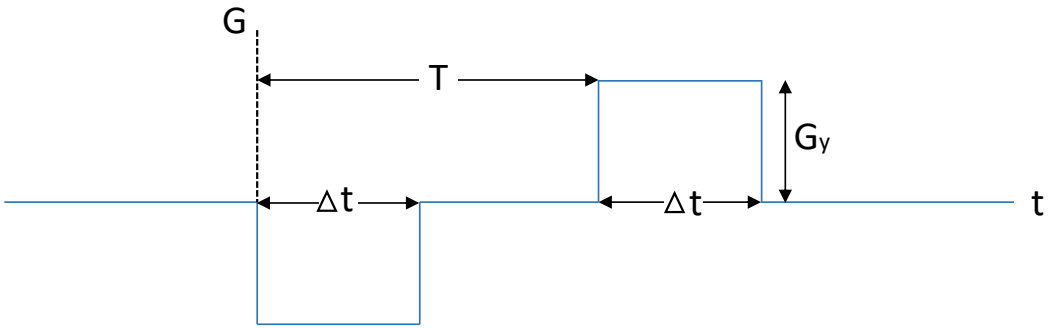

FIGURE 2.2: Schematic diagram of bipolar velocity coding gradient. It consists of two lobes of equal area and opposite polarity.

calculated by

$$M_1 = \int_0^{\triangle t} -G_y \tau d\tau + \gamma v_y \int_T^{T+\triangle t} G_y \tau d\tau = G_y \triangle tT \tag{2.18}$$

Introducing the area of a single gradient lobe $A = G \triangle t$, the phase difference is obtained by Equations 2.17 and 2.18

$$\phi = \gamma AT\boldsymbol{v} \tag{2.19}$$

To ensure that the range of the phase difference is from $-\pi$ to π (by toggling the gradient waveform), the encoding velocity v_{enc} is introduced. It represents the maximum measurable velocity.

$$v_{enc} = \frac{\pi}{\gamma \left| \Delta M_1 \right|} \tag{2.20}$$

where $\Delta M_1 = M_1 - (-M_1) = 2AT$. Moreover, the signal-to-noise ratio of the measured velocity SNR_v can be described by:

$$SNR_v = \frac{\pi}{2} \frac{v}{v_{enc}} SNR \tag{2.21}$$

here, SNR represents the signal-to-noise ratio of the image.

In clinical applications, blood flow measurements in the circulatory system are mainly accomplished using 2D PC MRI or 4D PC MRI.

- **2D PC MRI**

  Two-dimensional PC MRI (2D PC MRI) is performed to image one or more single slices at different moments. Each time only one specific layer is stimulated, usually chosen perpendicular to the vessel section. Based on 2D PC MRI data, the calculate cardiac outputs (regurgitant flow, reflux flow, fractional flow, and the ratio of pulmonary to circulating blood flow in cases of congenital or acquired heart disease) can be calculated.

- **4D PC MRI**

  Four-dimensional PC MRI (4D PC MRI) allows the simultaneous encoding of three mutually perpendicular dimensions at different moments. This technique enables the dynamic display of blood flow, which can be used for hemodynamic characterization of the heart and aorta. For example, by measuring velocity of blood flow in different directions at different locations, it is possible to calculate the mechanical parameters of blood flow (e.g. flow, regurgitant fraction) and to assess the blood flow energy and shear in the vessel wall. On the other hand, by displaying blood flow at different moments of the cardiac cycle, details of flow patterns, such as eddy or turbulent flow, and other complex blood flows can be observed.

Both 2D PC MRI and 4D PC MRI can be used to measure blood flows in the human body, but with their own limitations. First, 4D PC MRI is more convenient to obtain the time-varyiReng three-dimensional velocity field. Second, compared to 2D PC MRI, 4D PC MRI scans are somewhat more time consuming, taking 10-15 minutes, a time that depends on heart rate and respiratory control frequency. In contrast, 2D PC MRI is generally faster, usually less than 2-5 minutes.

2.1.3 Experimental setups

In this subsection, three phantoms used in this dissertation are described. Flows in these phantoms were measured using a MRI scanner Magnetom Skyra 3T (Siemens Healthineers, Erlangen, Germany) and the experimentally obtained flow data were utilized in Chapters 3 and 4.

- **Phantom of Normal Vessel**

  The flow in this phantom is used to represent low *Re* laminar flow in an idealized normal vessel geometry. The dark gray phantom, 20 cm in length and 40 mm in outer diameter, is located in a channel as shown in Figure 2.3. Water from the pump flows into the channel from its left side through two small inlet holes. A blue sponge is used to disperse the incoming water across the cross section of the channel. Water flow coming out of the sponge is uniform, and develops into laminar within the straws (each with diameter 5 mm).

- **3D printed Phantoms**

  The other phantoms with complex geometries, representing an idealized stenotic vessel and two patient specific aortas, were obtained by 3D printing. 3D printing, also known as additive manufacturing, is a technique for building objects layer by layer using bonded materials based on digital model files. The printing process is as follows: first, the desired geometry is designed and saved to an STL file in which the surface of the object is approximated by a large number of triangles. The model is then "split" into several layers in order to guide the printer to print layer by layer.

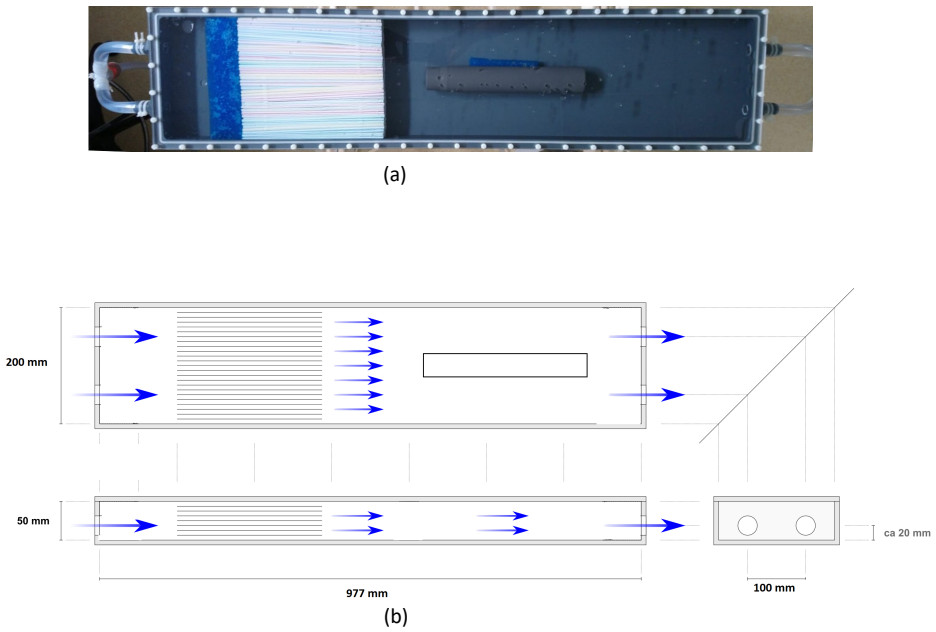

FIGURE 2.3: The display of the phantom for a normal vessel [2]. (a) photo of the flow channel; (b) the dimensions of the channel are 977 × 200 × 50 mm. The blue arrows show the flow direction.

The 3D printed phantoms in this dissertation and the corresponding printer used are shown in Figure 2.4.

The idealized stenotic vessel phantom was designed with Meshmixer [113] and printed using Ultimaker 2 Extended+. This printer uses crafting fused filament technology, with maximal printing dimension 323 × 223 × 305 mm, different layer resolution (0.2 mm, 0.1mm, 0.06 mm and 0.04mm) and printing speed (30-350 mm/s).

Two realistic aortic geometries were created by segmentation and reconstruction based on images from MRI. Particularly, the aortic region was selected based on gray value in the MRI slices, then multiple slices were stacked to a three dimensional geometry. Both geometries were printed with biocompatible MED610 as material using the Stratasys' high-end 3D laser printer Connex 3, with maximal printing dimension 340 × 340 × 200 mm and different layer resolution (0.03 mm or 0.016 mm). This printer works on the principle that tiny layers of liquid photopolymer are sprayed by a print head onto the building tray and then instantly cured with ultraviolet light. The layers are then built up to form a model.

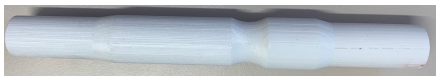

Outer surface

Inner surface

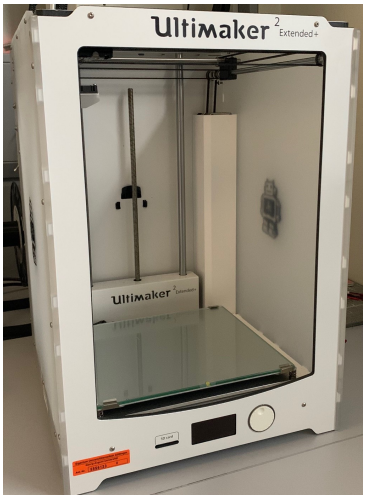

Outer surface

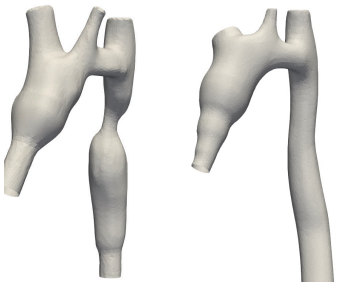

Inner surface

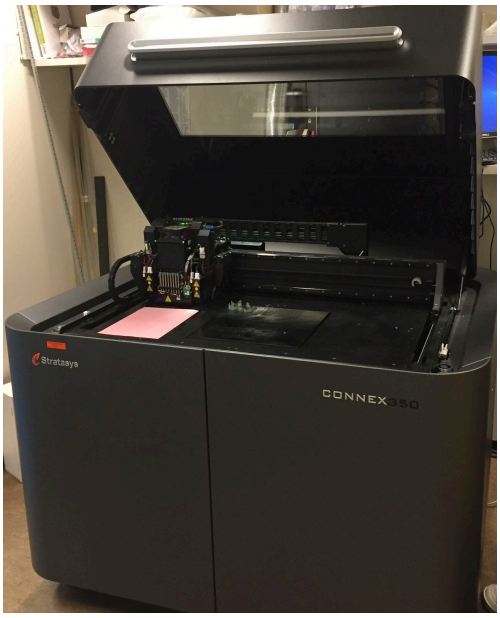

FIGURE 2.4: 3D printed phantoms and the corresponding printers used. Top, a straight pipe with stenosis; bottom, two aortic geometries. For each phantom, the inner surface was created based on specified dimensions or image segmentation, while the outer surface was obtained by extruding the inner surface to a given thickness for the purpose of 3D printing. More details of the phantoms are provided in Chapters 3 and 4.

2.2 Computational Fluid Dynamics

In CFD, several methods, such as the finite difference method, finite element method, and finite volume method, have been developed to resolve the governing equations of fluid flows, i.e. the Navier-Stokes Equations (NSE). In this dissertation, I used the LBM, considering its advantage in parallelization and modeling of flows with complex geometry. Here I first introduce the fluid governing equations, then list the methods for modeling turbulence, and finally provide a brief introduction to the LBM. This section is based on Refs. [78, 63, 11]. It is a general introduction of CFD.

2.2.1 The Governing Equations of Fluid Flows

In physics, based on the principles of conservation of mass, momentum and energy, the macroscopic motion of a flow can be described by the following governing equations.

- **Continuity equation**

  First, the fluid satisfies the law of conservation of matter in the process of flow. The law of conservation of mass is that the total mass of a system remains constant, no matter what changes the system evolve. And the Reynolds' transport equation is:

  $$\frac{D}{Dt}\int\limits_{V(t)} \rho dV = \int\limits_{V(t)} [\frac{\partial \rho}{\partial t} + \bigtriangledown \cdot (\rho \boldsymbol{u})] dV = 0 \tag{2.22}$$

  where D/Dt is the material derivative, V is the volume of fluid, ρ is the fluid density, and $\boldsymbol{u}$ is the velocity vector of fluid. The left side of the equation indicates the full derivative of the mass of the system with respect to time. In order to keep the integration constant zero in any region $V(t)$, the continuity equation, also called the mass conservation equation, is obtained:

  $$\frac{\partial \rho}{\partial t} + \rho \bigtriangledown \cdot \boldsymbol{u} = 0 \tag{2.23}$$

  For an incompressible fluid, such as the blood, the fluid density ρ remains constant. So the continuity equation for an incompressible fluid is simplified to

  $$\bigtriangledown \cdot \boldsymbol{u} = 0 \tag{2.24}$$

- **Momentum equation**

  According to Newton's second law, the rate of change of the total momentum of a system is equal to the sum of the total mass force acting on the system and the total surface force acting on the surface. That is

  $$\frac{D}{Dt}\int\limits_{V(t)} (\rho \boldsymbol{u}) dV = \int\limits_{V(t)} \rho \boldsymbol{F} dV + \int\limits_{A(t)} \boldsymbol{\sigma} \cdot \boldsymbol{n} dA \tag{2.25}$$

here σ is the mass force, $\boldsymbol{F}$ is a stress tensor, and $\boldsymbol{n}$ is the normal vector of the surface. According to Reynolds' second transport equation and Gauss's formula, it can be written:

$$\int_{V(t)} \rho \frac{D\boldsymbol{u}}{Dt} dV = \int_{V(t)} \rho \boldsymbol{F} dV + \int_{V(t)} \bigtriangledown \cdot \boldsymbol{\sigma} dV \tag{2.26}$$

Thus, the differential form of the momentum equation is obtained:

$$\rho \frac{D\boldsymbol{u}}{Dt} = \rho \boldsymbol{F} + \bigtriangledown \cdot \boldsymbol{\sigma} \tag{2.27}$$

Combined with continuity equation, the conservative form of momentum equation is:

$$\frac{\partial(\rho \boldsymbol{u})}{\partial t} + \bigtriangledown \cdot (\rho c u \boldsymbol{u}) = \rho \boldsymbol{F} + \bigtriangledown \cdot \boldsymbol{\sigma} \tag{2.28}$$

Introducing the constitutive equation, the stress tensor is:

$$\boldsymbol{\sigma} = -p\boldsymbol{I} + 2\mu \boldsymbol{S} + \mu^{'}(\bigtriangledown \cdot \boldsymbol{u})\boldsymbol{I} \tag{2.29}$$

where p, $\boldsymbol{I}$ are static pressure of fluid and the second-order unit tensor, respectively. μ and $\mu^{'}$ are the dynamic viscosity and the second coefficient of viscosity. For the same fluid at a certain temperature, μ and $\mu^{'}$ are constant. $\boldsymbol{S}$ is the strain rate tensor and defined as $\boldsymbol{S} = \frac{1}{2}\left[\bigtriangledown \boldsymbol{u} + (\bigtriangledown \boldsymbol{u})^T\right]$.

Bring Equation 2.29 into Equation 2.27, another form of the momentum conservation equation is obtained:

$$\frac{\partial(\rho \boldsymbol{u})}{\partial t} + \bigtriangledown \cdot (\rho \boldsymbol{u}\boldsymbol{u}) = \rho \boldsymbol{F} - \bigtriangledown p + \bigtriangledown \cdot [\mu(\bigtriangledown \boldsymbol{u} + (\bigtriangledown \boldsymbol{u})^T)] + \bigtriangledown(\mu^{'} \bigtriangledown \cdot \boldsymbol{u}) \tag{2.30}$$

Equation 2.30 is called Navier-Stokes equations (NSE).

- **Energy equation**

  If there is heat transfer, the first law of thermodynamics must be considered in the fluid flow process. According to the first law of thermodynamics, in a system, the change in internal energy depends on the work done by external forces and the heat transfer. Therefore, when studying the energy conservation of fluid systems, the changes of kinetic energy and internal energy must be considered:

$$\frac{D}{Dt} \int_{V(t)} \rho(\varepsilon + \frac{1}{2}\boldsymbol{u}^2) dV = \int_{V(t)} \rho \boldsymbol{F} \cdot \boldsymbol{u} dV + \int_{A(t)} (\boldsymbol{n} \cdot \boldsymbol{\sigma}) \cdot \boldsymbol{u} dA + \int_{V(t)} \rho Q u dV - \int_{A(t)} \boldsymbol{q} \cdot \boldsymbol{n} dA \tag{2.31}$$

In the formula, Q represents the increase of heat per unit mass of fluid caused by factors such as radiation or chemical energy release, $-\int_{A(t)} \boldsymbol{q} \cdot \boldsymbol{n} dA$ represents the heat increment caused by heat conduction, and the negative sign represents that the heat retention direction is opposite to the direction $\boldsymbol{n}$ of the outer normal to the surface of the volume. The internal energy equation after introducing the dissipation function Φ is

$$\frac{\partial(\rho\varepsilon)}{\partial t} + \bigtriangledown \cdot (\rho\varepsilon \boldsymbol{u}) = -p \bigtriangledown \cdot \boldsymbol{u} + \bigtriangledown \cdot (\lambda \bigtriangledown T) + \Phi + \rho Q \tag{2.32}$$

Equations 2.23, 2.30, 2.43 form the governing equations of fluid flow. For 3D problems, there are seven equations in total and seven unknown parameters (density ρ, three velocity components, pressure p, internal energy ε, temperature T), thus the system of equations is closed.

For incompressible fluids such as blood, the density is constant and the continuity and momentum equations contain four unknown parameters (three components of $\boldsymbol{u}$, and p). Moreover, fluid flow and heat transfer are not coupled, thus can be solved separately.

2.2.2 Numerical Approaches for Modeling Turbulent Flow

Turbulent flow is irregular and multiscale flow, generally three-dimensional and unsteady, with strong diffusivity and dissipation. Turbulent flows consist of a composition of rotating vortices on different scales, which are random in their distribution, size and direction of the rotation axis. The large-scale vortices cause low frequency pulsations, which are mainly affected by the boundary conditions. small-scale vortices cause high frequency pulsations, which are mainly determined by the viscous forces. Vortices of different scales form relatively small-scale vortices after rupture. In a fully developed turbulent region, the scale of fluid vortices can vary continuously. Through the interaction between large-scale vortices and small-scale vortices, the energy in the main flow is gradually transferred to the vortices in small-scale. Finally, mechanical energy is converted into thermal energy due to the continuous disappearance of small-scale vortices.

Despite the complexity of turbulent motion, the aforementioned governing equations are still applicable to turbulent flows. However, the strong transient and nonlinear characteristics of turbulent flow make it very challenging to accurately describe the full details of turbulence. Therefore, mathematical approaches for different simplifications of turbulence have emerged.

In general, computational approaches for turbulence fall into two main categories: direct simulation simulations and non-direct simulations (scale-resolved simulations, Reynolds time-averaged simulations).

- **Direct numerical simulation (DNS)**

DNS directly solve the governing equations of turbulent flow with different numerical methods. This means that the flow must be resolved in all range of spatial and temporal scales. All spatial scales of turbulence, from the smallest dissipative scale (Kolmogorov scale, η) to the integral scale (L) must be solved in a computational grid. The number of grid points (N^3) required for three-dimensional DNS is related to the Reynolds number Re of the flow [88]:

$$N^3 \geq Re^{2.25} \tag{2.33}$$

In addition, the number of time-integration steps (L/η) is proportional to

$$\frac{L}{\eta} \sim Re^{0.75} \tag{2.34}$$

Since the number of floating-point operations used to perform the simulation grows with the number of time steps and the number of grid points, the growth rate of the number of operations is known from the above equation as Re^3.

DNS is a useful tool in basic studies of turbulence, and regarded as as "numerical experiment" and "golden standard". On the other hand, it is computationally expensive, even for low Re problems. Based on this, other simplified turbulence models have been proposed.

- **Large eddy simulation (LES)**

  LES is a kind of non-direct simulation. The basic concept of LES is to solve the flow field by accurately solving the motion of turbulent flows at all scales larger than a certain one. LES can capture large-scale effects and the coherent structure of non-stationary processes and non-equilibrium processes, which is not possible with Reynolds time-averaged simulations. In addition, LES greatly saves computational consumption compared to DNS that solves all turbulence scales [96, 108].

  LES is filtered in space and time by using a filter $\varphi(\boldsymbol{x}, t)$, which is defined as:

$$\overline{\varphi(\boldsymbol{x}, t)} = \int_{-\infty}^{\infty} \int_{-\infty}^{\infty} \varphi(\boldsymbol{r}, \tau) M(\boldsymbol{x} - \boldsymbol{r}, t - \tau) d\tau d\boldsymbol{r} \tag{2.35}$$

  where M is the filter convolution kernel. For incompressible flows, the scalar form of continuity equation and NSE are filtered to obtain the incompressible continuity equation filtered:

$$\frac{\partial \overline{u_i}}{\partial x_i} = 0, \tag{2.36}$$

$$\frac{\partial \overline{u}_i}{\partial t} + \overline{u}_j \frac{\partial (\overline{u}_i)}{\partial x_j} = -\frac{1}{\rho} \frac{\partial \overline{p}}{\partial u_i} + \nu \frac{\partial^2 \overline{u}_i}{\partial x_j \partial x_j} - \frac{\partial \tau_{ij}}{\partial x_j} \tag{2.37}$$

where $\overline{p}$ is the filtered pressure and $\overline{u}$ is the filtered velocity. $\tau_{ij} = \overline{u_i u_j} - \overline{u}_i \overline{u}_j$, known as subgrid-scale (SGS) stress, reflects the effect of small-scale vortex motion on the equations of motion. The SGS stress is unknown, and the mathematical expression of the SGS stress needs to be constructed using the relevant physical model. For example, considering that the kinetic energy dissipation on the subgrid scale is similar to molecular diffusion, τ is modeled as:

$$\tau_{ij} - \frac{1}{3}\tau_{kk}\delta_{ij} = -2\nu_t \overline{S}_{ij} \tag{2.38}$$

where ν_t is the turbulent viscosity; $\overline{S}_{ij} = \frac{1}{2}(\frac{\partial \overline{u}_i}{\partial x_j} + \frac{\partial \overline{u}_j}{\partial x_i})$ is the strain rate tensor. In Chapter 3, I used the Smagorinsky-Lilly SGS model [116] for aortic flow simulation. This model is based on the assumption that generation and dissipation of energy are in equilibrium on small scales. It models the vortex viscosity as:

$$\nu_t = C \triangle^2 \sqrt{2\bar{S}_{ij}\bar{S}_{ij}} = C \triangle^2 \left|\bar{S}\right| \tag{2.39}$$

where $\triangle$ is the grid size and C is a constant.

- **Reynolds-averaged Navier–Stokes (RANS)**

  The RANS is different from DNS and LES. RANS is the governing equation for the mean variable of the flow field and is based on the theoretical assumption that the fluid variables in turbulent flow, such as velocity, pressure, etc., can be decomposed into two parts: a mean value (time averaged) and a pulsating value. It is a statistical averaging of the governing equations, ignoring the turbulent pulsations at each scale and calculating only the mean motion, thus reducing the spatial and temporal resolution as well as the computational effort. In RANS, the continuity and momentum equations for incompressible flows can be written as follow:

$$\frac{\partial(u_i)}{\partial x_i} = 0, \tag{2.40}$$

$$\frac{\partial(u_i)}{\partial t} + \frac{\partial(u_j u_i)}{\partial x_j} = -\frac{1}{\rho}\frac{\partial p}{\partial u_i} + \frac{1}{\rho}\frac{\partial \sigma_{ij}}{\partial x_j} + \frac{\partial(-u_i^{'}u_j^{'})}{\partial x_i}. \tag{2.41}$$

  where u_i is the Reynolds average velocity component, $u_i^{'}$ is the pulsation velocity, σ_{ij} is the stress tensor. $-\rho u_i^{'}u_j^{'}$ is called Reynolds stress and determined by the pulsation velocity.

  Although RANS can largely reduce computational consumption, it has some drawbacks. The unknown term Reynolds stress needs to be solved by developing a turbulence model, which relies on a combination of theory and

empirical formula. To establish a closed set of equations describing the averaged flow quantities, several model assumptions based on the RANS equations and the pulsation equations have been proposed. Examples are the two-equation model, the single-equation model and the zero-equation model (algebraic model). In addition, the closed equations need to be adjusted to the nature and results of the large-scale pulsations and the boundary conditions of the flow.

2.2.3 Lattice Boltzmann Method

The LBM was used for CFD simulations in this dissertation.

- **Boltzmann equation and Maxwell distribution**

  Besides the aforementioned macroscopic governing equations, fluid flow can also be governed by the mesoscopic Boltzmann equation, which describes the statistical behaviour of fluid particles based on kinetic theory. The fluid particles can move and collide with each other. The probability of each particle being in a certain state is described by the distribution function f, which is related to spatial location $\boldsymbol{r}(x, y, z)$ and particle velocity $\boldsymbol{\xi}(\xi_x, \xi_x, \xi_z)$. At time t and location $\boldsymbol{r}$, the number of particle per unit volume n is

  $$n = \int f(\boldsymbol{r}, \boldsymbol{\xi}, t) d\xi \tag{2.42}$$

  The change in the number of particles is due to particle motion and collision. For individual particle, $(\partial f/\partial t)_{motion}$ is caused by particle motion. $F = m\boldsymbol{a}$ is expressed as the external force applied to the particle, where m is the particle mass. Then $(\partial f/\partial t)_{motion}$ can be expressed as

  $$(\frac{\partial f}{\partial t})_{motion} = -\xi \cdot \frac{\partial f}{\partial r} - \boldsymbol{a} \cdot \frac{\partial f}{\partial \xi}, \tag{2.43}$$

  Introducing $\Omega(f) = (\partial f/\partial t)_{collision}$ for particle number change resulted from particle collision, and $\partial f/\partial t$ the total change in the number of particles during time interval dt, one gets the Boltzmann equation:

  $$\frac{\partial f}{\partial t} + \boldsymbol{\xi} \cdot \frac{\partial f}{\partial \boldsymbol{r}} + \boldsymbol{a} \cdot \frac{\partial f}{\partial \boldsymbol{\xi}} = \Omega(f) \tag{2.44}$$

  To simplify the formula, normally only two-body collision is considered. Even then, it is very hard to get an analytical solution to the Boltzmann equation. For the gas with one single component without external force, the Boltzmann equation can be solved with the equilibrium distribution, which is called the Maxwell distribution:

  $$f^{eq} = n\frac{1}{(2\pi RT)^{d/2}} exp[-\frac{(\boldsymbol{\xi} - \boldsymbol{u})^2}{2RT}] \tag{2.45}$$

where $1/n$, T and $\boldsymbol{u}$ are the macroscopic fluid density, temperature, and velocity, respectively. $\boldsymbol{\xi} - \boldsymbol{u}$ is the peculiar velocity (random velocity), R is the gas constant, d is the dimension. Although the Maxwell distribution is based on the assumption of a single-component monoatomic gas, it can also be applied to the case of diatomic polyatomic gases [31].

- **Boltzmann-BGK equation and lattice Boltzmann equation**

  It should be mentioned that the macroscopic governing equations, e.g. the NSE, can be recovered from the mesoscopic Boltzmann equation. Thus one can numerical model fluid flows by solving the Boltzmann equation. The main difficulty in solving the Boltzmann equation lies in the collision term, mainly due to its nonlinearity. Bhatnager, Gross and Krook proposed to replace this nonlinear collision term in the Boltzmann equation with a simple and linear operator, as shown in Equation 2.46. Their assumptions are: the collision-based effect is to change f so that it approximates the equilibrium distribution f^{eq}; the change rate is proportional to $f^{eq} - f$; v is a constant independent of particle velocity $\boldsymbol{\xi}$. So, one gets

$$\Omega_f = v\left[f^{eq}(\boldsymbol{r}, \boldsymbol{\xi}) - f(\boldsymbol{r}, \boldsymbol{\xi}, t)\right] \tag{2.46}$$

  Substitute Equation 2.46 into Equation 2.44, one gets the Boltzmann-BGK equation

$$\frac{\partial f}{\partial t} + \boldsymbol{\xi} \cdot \frac{\partial f}{\partial \boldsymbol{r}} + \boldsymbol{a} \cdot \frac{\partial f}{\partial \boldsymbol{r}} = v\left[f^{eq}(\boldsymbol{r}, \boldsymbol{\xi}) - f(\boldsymbol{r}, \boldsymbol{\xi}, t)\right] \tag{2.47}$$

  Therefore, $\boldsymbol{u}$, T in f^{eq} are the macroscopic parameters (density, velocity and temperature) obtained by the velocity distribution function. Since the equilibrium distribution function varies with time and space, it is called the local equilibrium distribution function. The collision time $\tau_0 = \frac{1}{v}$ is also called relaxation time, indicating the time interval between two collisions.

  To numerically solve it, the Boltzmann-BGK equation is further discretized in the space of velocity, time and space. Accordingly, the Lattice Boltzmann Method (LBM) is generated [42, 115]. The Boltzmann-BGK equation is firstly discretized in the velocity space. Since the details of particle motion do not significantly affect the macroscopic motion of the fluid, instead of random movements, the particles are forced to move/stream along specified directions with given discrete velocities (lattice). The particle velocity $\boldsymbol{\xi}$ and distribution function f are then represented by $\{e_0, e_1, \cdots, e_N\}$ and $\{f_0, f_1, \cdots, f_N\}$, respectively. Here $\boldsymbol{e}_i$ is the discrete velocity of a lattice; $f_i = f_i(\boldsymbol{r}, \boldsymbol{e}_i, t)$; $i = 0, 1, \cdots, N$ with N the total number of discrete velocities of a lattice. Then the Boltzmann equation is discretized in both space and time, with spatial resolution $\boldsymbol{e_i}\delta_t$ and temporal resolution δ_t. We finally get the lattice Boltzmann equation with BGK

operator and external force:

$$f_i(\boldsymbol{r}+\boldsymbol{e}_i\delta_t, t+\delta_t) - f_i(\boldsymbol{r},t) = -\frac{1}{\tau}\left[f_i(\boldsymbol{r},t) - f_i^{eq}(\boldsymbol{r},t)\right] + \delta_t F_i(\boldsymbol{r},t) \tag{2.48}$$

where, dimensionless relaxation time $\tau = \tau_0/\delta_t$.

Space discretization and time discretization are not independent and can be linked by the discrete velocity of the particles. This feature provides the conditions for dividing the motion of particles in physical space into the processes of streaming and collision.

- **Lattice Boltzmann model**

  Three components of the discrete velocity model (lattice), the equilibrium distribution function and the evolution equation make up the lattice Boltzmann model [140]. To develop a LBM model, the first step is to derive the constraints for the equilibrium distribution function f^{eq} so that the corresponding macroscopic equations can be recovered from the Boltzmann equation. Then a suitable discrete velocity model (lattice) is selected and the equilibrium state distribution function is determined based on the equations obtained from the model through the constraints. The $DdQm$ lattices [98] are the most popular ones used in the LBM community. Here d and m represent the dimension and the number of discrete velocities, respectively. The equilibrium distribution function f^{eq} adopted in a $DdQm$ lattice reads

$$f_i^{eq} = \rho\omega_i\left[1 + \frac{\boldsymbol{e}_i\cdot\boldsymbol{u}}{c_s^2} + \frac{(\boldsymbol{e}_i\cdot\boldsymbol{u})^2}{2c_s^4} - \frac{u^2}{2c_s^2}\right] \tag{2.49}$$

  where ω_i is weight factor and c_s is the lattice speed of sound. Macroscopic parameters such as density ρ and velocity $\boldsymbol{u}$ can be obtained via the following formulas:

$$\sum_i f_i^{eq} = \rho, \tag{2.50}$$

$$\sum_i f_i^{eq}\boldsymbol{e}_i = \rho\boldsymbol{u}, \tag{2.51}$$

  The D3Q19 lattice, as shown in Figure 2.5, is one of the commonly used lattices for 3D fluid flows. Its discrete velocity, weight factor and sound speed are listed in Table 2.1. The D3Q19 lattice is also adopted in this dissertation, for simulations with the LBM.

- **Boundary treatment**

  Boundary conditions play a very important role in fluid mechanics. For example, for steady state problems, when a system reaches its stability, the flow field is mainly determined by the boundary conditions. In addition, boundary

TABLE 2.1: The weight factors and discrete velocities in the D3Q19 lattice.

i	0	1	2	3	4	5	6	7	8	9	10	11	12	13	14	15	16	17	18
ω_i	$\frac{1}{3}$	$\frac{1}{18}$	$\frac{1}{18}$	$\frac{1}{18}$	$\frac{1}{18}$	$\frac{1}{18}$	$\frac{1}{18}$	$\frac{1}{36}$	$\frac{1}{36}$	$\frac{1}{36}$	$\frac{1}{36}$	$\frac{1}{36}$	$\frac{1}{36}$	$\frac{1}{36}$	$\frac{1}{36}$	$\frac{1}{36}$	$\frac{1}{36}$	$\frac{1}{36}$	$\frac{1}{36}$
c_{ix}	0	+1	-1	0	0	0	0	+1	-1	+1	-1	0	0	+1	-1	+1	-1	0	0
c_{iy}	0	1	2	3	4	5	6	7	8	9	10	11	12	13	14	15	16	17	18
c_{iz}	0	0	0	0	0	+1	-1	0	0	+1	-1	+1	-1	0	0	-1	+1	-1	+1

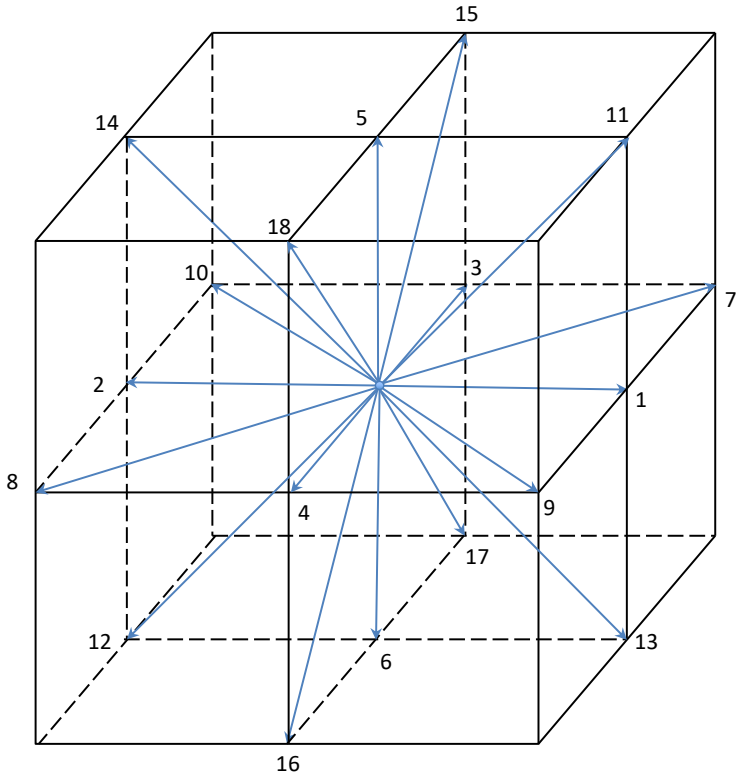

FIGURE 2.5: The D3Q19 lattice.

treatment is very critical in the LBM, and they have a great impact on the accuracy, computational efficiency and computational stability of numerical modeling. During simulation, the distribution functions in the main flow domain are obtained after each time step, but the distribution functions at the boundary nodes are unknown. Therefore, it is necessary to determine the corresponding distribution functions at the boundary nodes based on known boundary conditions on the macroscopic scale. Here, I explain the treatment of the complex boundaries used for the simulations in Chapter 3. Without external force, the lattice Boltzmann Equation 2.48 reads

$$f_i(\boldsymbol{r}+\boldsymbol{e}_i\delta_t, t+\delta_t) - f_i(\boldsymbol{r},t) = -\frac{1}{\tau}\left[f_i(\boldsymbol{r},t) - f_i^{eq}(\boldsymbol{r},t)\right] \tag{2.52}$$

The above equation represents the two processes of particle movement: collision and streaming. During the collision process, fluid particles at the same node collide with each other. f_i^+ is the distribution function after the collision:

$$f_i^+(\boldsymbol{r},t) - f_i(\boldsymbol{r},t) = -\frac{1}{\tau}\left[f_i(\boldsymbol{r},t) - f_i^{eq}(\boldsymbol{r},t)\right] \tag{2.53}$$

During the streaming process, fluid particles move along the grid lines in different directions and migrate to the neighboring nodes $\boldsymbol{r}+\boldsymbol{e}_i\delta_t$. This leads to

$$f_i(\boldsymbol{r}+\boldsymbol{e}_i\delta_t, t+\delta_t) = f_i^+(\boldsymbol{r},t), \tag{2.54}$$

For example, in Figure 2.6, $\boldsymbol{e}_i$ is a discrete velocity of fluid particle pointing to the boundary node, and $\boldsymbol{e}_{\bar{i}} = -\boldsymbol{e}_i$ is the discrete velocity in the opposite direction. The unknown distribution function $f_{\bar{i}}^+$ on the boundary node $\boldsymbol{r}_b$ moves along $\boldsymbol{e}_{\bar{i}}$ into the fluid node $\boldsymbol{r}_f$. The expression is

$$f_{\bar{i}}(\boldsymbol{r}_f = \boldsymbol{r}_b + \boldsymbol{e}_{\bar{i}}\delta_t, t+\delta_t) = f_{\bar{i}}^+(\boldsymbol{r}_b, t) \tag{2.55}$$

Several boundary schemes [34, 14] have been introduced to obtain $f_{\bar{i}}^+(\boldsymbol{r}_b,t)$ or $f_{\bar{i}}(\boldsymbol{r}_f, t+\delta_t)$.

An extrapolation scheme was proposed by Guo et al. to deal with curved boundaries in the LBM [40]. Such boundary treatment is adopted in the simulations in this dissertation, and will be introduced briefly. The basic idea of this scheme is to divide the distribution function at a boundary node into two parts: equilibrium state $f_{\bar{i}}^{+,eq}(\boldsymbol{r}_b,t)$ and non-equilibrium state $f_{\bar{i}}^{+,neq}(\boldsymbol{r}_b,t)$.

$$f_{\bar{i}}^+(\boldsymbol{r}_b,t) = f_{\bar{i}}^{+,eq}(\boldsymbol{r}_b,t) + f_{\bar{i}}^{+,neq}(\boldsymbol{r}_b,t) \tag{2.56}$$

The equilibrium part is replaced by a virtual equilibrium distribution function, and the non-equilibrium part is obtained by interpolating the non-equilibrium

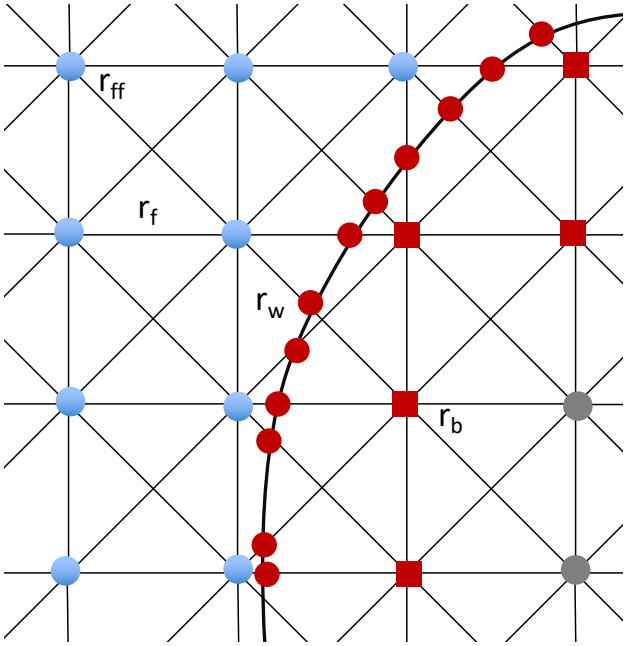

FIGURE 2.6: The Schematic of node types on complex boundaries. The black curve represents the actual physical boundary, with red dots the intersection of the physical boundary and the grid lines. The blue circular dots, red square dots and gray circular dots represent the fluid nodes, boundary nodes, and solid nodes, respectively.

part of the adjacent fluid nodes. Specifically

$$f_{\bar{i}}^{+,eq}(\boldsymbol{r}_b, t) = f_{\bar{i}}^{eq}(\rho_b, \boldsymbol{u}_b, t) \tag{2.57}$$

where ρ_b and $\boldsymbol{u}_b$ are defined as bellow:

if $q \geq q_c$, $\rho(\boldsymbol{r}_b) = \rho(\boldsymbol{r}_f)$, $\boldsymbol{u}_b = \frac{\boldsymbol{u}_w + (q-1)\boldsymbol{u}_f}{q}$,

if $q < q_c$, $\rho(\boldsymbol{r}_b) = \rho(\boldsymbol{r}_f)$, $\boldsymbol{u}_b = \frac{\boldsymbol{u}_w + (q-1)\boldsymbol{u}_f}{q} + (1-q)\frac{2\boldsymbol{u}_w + (q-1)\boldsymbol{u}_{ff}}{q}$.

The non-equilibrium part is obtained by interpolating the distribution function on the fluid node:

if $q \geq q_c$, $f_{\bar{i}}^{+,neq}(\boldsymbol{r}_b, t) = f_{\bar{i}}(\boldsymbol{r}_f, t) - f_{\bar{i}}^{eq}(\boldsymbol{r}_f, t)$,

if $q < q_c$, $f_{\bar{i}}^{+,neq}(\boldsymbol{r}_b, t) = q[f_{\bar{i}}(\boldsymbol{r}_f, t) - f_{\bar{i}}^{eq}(\boldsymbol{r}_f, t)] + (1-q)[f_{\bar{i}}(\boldsymbol{r}'_{ff}, t) - f_{\bar{i}}^{eq}(\boldsymbol{r}_{ff}, t)]$.

In the formula, $q_c \in (0, 1)$ is the judgment condition of the interpolation format. Such boundary treatment has second-order accuracy in space and time,

and good numerical stability [40].

- **LBM based LES**

  As described in Section 2.2.2, the Smagorinsky model is based on the assumption of eddy viscosity, and the turbulent viscosity correction is defined as

$$\nu_t = C \triangle^2 \sqrt{2\bar{S}_{ij}\bar{S}_{ij}} \tag{2.58}$$

  here, C is the Smagorinsky constrant, which depends on the physical problem. In LBM, $\bar{S}_{ij}$ can be calculated based on the distribution function:

$$\bar{S}_{ij} = -\frac{3}{2e^2\rho(\tau+\tau_{SGS})\delta_t}\sum e_{ki}e_{kj}(f_k - f_k^{eq}) \tag{2.59}$$

  where τ_{SGS} is eddy relaxation time. The total relaxation time, which determines the speed of approaching local equilibrium, can be expressed as

$$\tau_{total} = \tau + \tau_{SGS} \tag{2.60}$$

  And, the relationship between viscosity coefficients and relaxation times are

$$\nu_{total} = \frac{e^2\delta_t}{6}(2\tau_{total} - 1) \tag{2.61}$$

$$\nu = \frac{e^2\delta_t}{6}(2\tau - 1) \tag{2.62}$$

  where ν_{total} is the effective viscosity coefficient. Then, based on Equations 2.60-2.62, τ_{SGS} is calculated:

$$\tau_{SGS} = \frac{3\nu_t}{e^2\delta_t} = \frac{3\nu_t}{e^2\delta_t}(C\triangle)^2\sqrt{2\bar{S}_{ij}\bar{S}_{ij}} = -\frac{9(C\triangle)^2}{2e^2\rho}(\tau+\tau_{SGS})\delta_t^2\sqrt{2\prod_{ij}\prod_{ij}} \tag{2.63}$$

  where $\prod_{ij}\prod_{ij} = \sum e_{ki}e_{kj}(f_k - f_k^{eq})$. In equidistant square grids($\Delta = \Delta_x = \Delta_y = \Delta_z$), the total relaxation time can be written:

$$\tau_{total} = \tau + \tau_{SGS} = \frac{\tau + \sqrt{\tau^2 + 18(C\triangle)^2\sqrt{2\prod_{ij}\prod_{ij}}/(e^4\rho\delta_t^2)}}{2} \tag{2.64}$$

  Finally, the LBM based LES (Smagorinsky model) can be given:

$$f_i(\boldsymbol{r}+\boldsymbol{e}_i\delta_t, t+\delta_t) - f_i(\boldsymbol{r},t) = -\frac{1}{\tau_{total}}\left[f_i(\boldsymbol{r},t) - f_i^{eq}(\boldsymbol{r},t)\right] \tag{2.65}$$

2.3 Machine Learning and Physics Informed Neural Network

As described in Chapter 1, PINN is a novel technique that can be used for hemodynamic studies based on the basic governing equations of fluids and ML. A brief overview of ML, particularly NN, is provided in Section 2.3.1. Then PINN, and optimizer and AD used in PINN, are provided in Section 2.3.2. This section is based on Refs. [55, 61, 58, 17, 107].

2.3.1 Machine Learning and Neural Network

Machine learning (ML) is an important part of artificial intelligence. This technology guides computers to learn from data and then use "experience" to improve its performance. In the learning process, machines discover correlations and patterns from large data sets through continuous training, and then make the best predictions and decisions based on the results of data analysis. Data are an important part of machine learning. Generally the more data used for learning, the more accurate the predictions will be. Three types of ML [55], namely supervised learning, unsupervised learning and reinforcement learning, are described below:

- **Supervised learning**

  The machine learns from existing samples. Supervised learning models consist of data pairs ("input" and "output"), where the output is labeled with the desired value. By applying the algorithm, the system is able to compile the training data and start identifying relevant similarities, differences and other logical points until it is able to predict the results autonomously.

- **Unsupervised learning**

  The machine needs to study the input data itself (most of which is unlabeled and unstructured) and start using all the relevant, accessible "intuition" and "experience" to connect things together. For machines, "experience" depends on the input and the amount of data available.

- **Reinforcement learning**

  Reinforcement learning, unlike supervised and unsupervised learning, works by constantly interacting with the environment, by trial and error, and finally by accomplishing a specific goal. In Reinforcement learning, the labels for training data are not needed, while the feedback from the environment is needed at each step of the action, and continuously adjusts the behavior of the training object based on the feedback.

Neural network (NN) is one of machine learning algorithms that mimics the structure and function of a biological NN. It is computed by connecting a large number of artificial neurons for estimating or approximating functions. In most cases, an artificial NN can change its internal structure in response to external information,

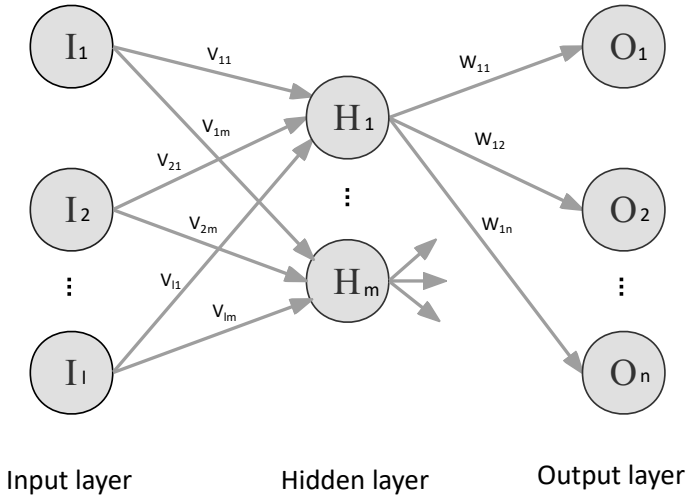

FIGURE 2.7: A multi-layer feed-forward NN. I_i are the input neurons; H_j are the hidden neurons; O_k are the hidden neurons; H_{ij} are the weights of the input of the hidden layer; W_{jk} are the weights of the output of the hidden layer.

which is an adaptive system. A common multi-layer structured feed-forward network consists of three parts, as shown in Figure 2.7.

- **The input layer**

  It is where large amount of nonlinear input information is received by neurons.

- **The hidden layer**

  It is the connection layer between the input and output layers and consists of single or multiple hidden layers. The role is to take the features of the input data and abstract them to another dimensional space to present their more abstracted features that are better able to be divided linearly.

- **The output layer**

  It is the last layer of the NN where the input from the last hidden layer is received and the result is output.

The process of building a model by correcting the weights of each layer through the training samples is called training algorithm. Different learning methods have different network models and structures.

2.3.2 Physics Informed Neural Network

As mentioned earlier, data is very important to NN. Based on the amount of data, there are three possible categories of physical problems: big data system, some data

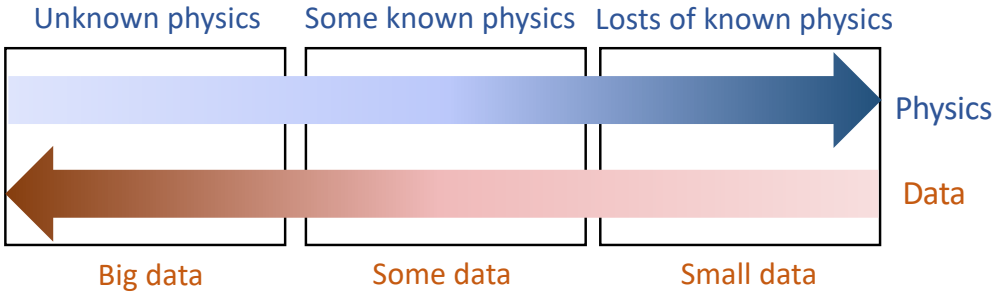

FIGURE 2.8: Relation of data-driven and physical principles. Diagram modified from [58].

system, and small data system, as shown in Figure 2.8. In the big data system, there is no need to model the physics principles and a data-driven approach may be the most effective. In small data system, it is assumed that we have all the physics principles and less data information, such as the initial and/or boundary conditions, thus numerical modeling or analytical analysis can be considered. The most common is the intermediate system, where some data and some physical principles are known and some parameter values in Partial differential equations (PDE) may be missing. Therefore, there is a need for a new approach to machine learning with sparse data and available mathematical models, combining data-driven methods and physical principles, thus integrating experimental and numerical methods into the same model.

In 2019, Kissas et al. proposed physics-informed neural network (PINN), which combine constraints on existing data with governing equations so that training approximates both the training data and the physically informative PDE. The specific way to implement the equation constraints is to use the automatic differentiation (AD) tool in TensorFlow [1] to estimate the residuals of the equations. The loss of the residuals is updated in each iteration and added to the loss function of the NN. During the training process, the NN minimizes the total loss function containing the data error and the residuals of the equations to achieve a final training result that satisfies both the data and the physical laws [61, 27].

The general form of the PDE in the space-time domain solved by PINN is:

$$F(u(z);\lambda) = f(z), z \in \Omega, \Omega \subset R^N \tag{2.66}$$

$$B(u(z)) = b(z), z \in \partial\Omega \tag{2.67}$$

where $z = [x_i \dots x_{n-1}; t]$. F is general nonlinear differential operator and f is a function that identifies the problem data, $u(-)$ is the potential solution, λ is the parameters of PDE. $B(-)$ is the boundary condition or/and initial condition and b is the boundary function.

The architecture of PINN is given in Figure 2.9. It can be seen that PINN consists

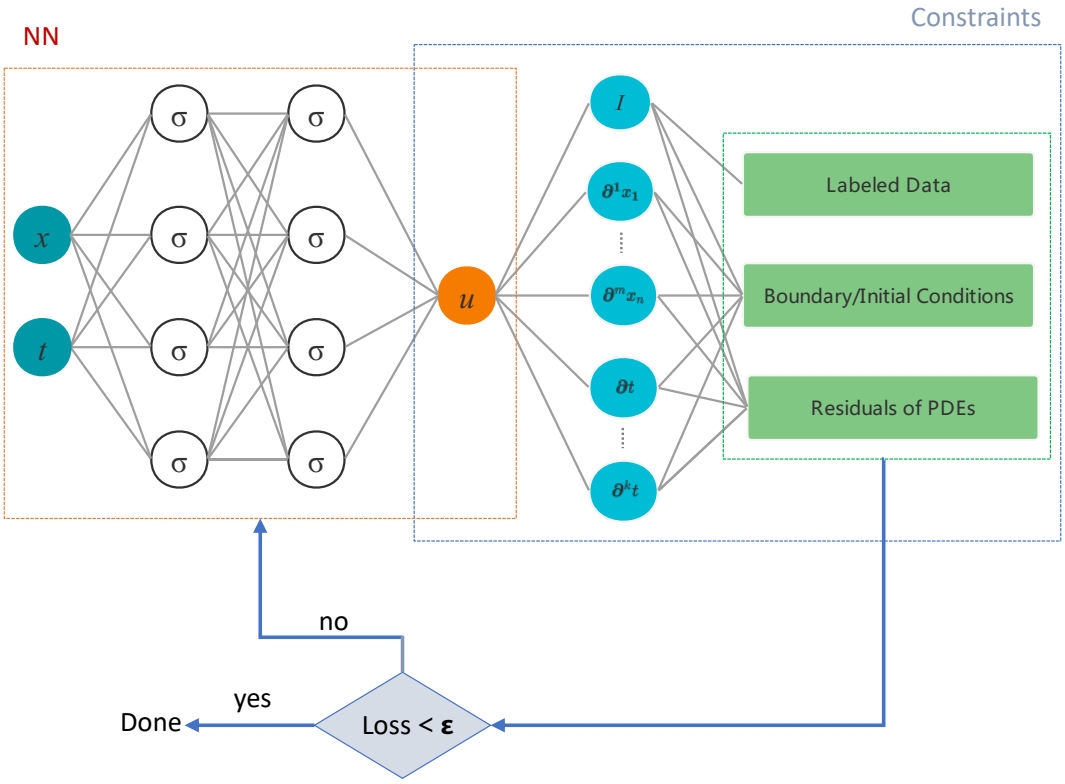

FIGURE 2.9: The architecture of PINN. The NN and constraints are shown in red and blue boxes, respectively.

of a NN on the left and constraint (data constraint and PDE constraint) on the right. In the NN part, the inputs are x and t, while the output is u. This network represents the mapping of inputs x, t and output u from points to unknown solutions, where σ is the activation function that enhances the nonlinearity of NN, giving it the ability to describe and approximate highly nonlinear problems. In the constraint part, the total loss function (consisting of the loss of the labeled data, the loss of the boundary or initial conditions, and the deviation of the PDE) is computed and give feedback to the NN.

The total loss in PINN is minimized using the optimizer and the parameters of NN are obtained based on the learning rate. More details are given below.

Optimizer

In NN, optimization algorithms can help us to minimize an objective function (such as loss function). The weights and biases can be considered as internal learnable parameters of the NN, which are used to calculate the output values and learn and update them in the direction of the optimization scheme to minimize the losses. Gradient descent is briefly introduced in the following, as one of the most commonly used optimization algorithms in NN.

- **Stochastic gradient descent**

  Stochastic gradient descent (SGD) updates the model parameters by searching the minimum value to control the variance and eventually converge the model. The formula for updating the parameters is:

$$\theta_{t+1} = \theta_t - \eta \bigtriangledown_\theta J(\theta) \tag{2.68}$$

  where η, $J(\theta)$ and $\bigtriangledown_\theta J(\theta)$ represent the learning rate, the loss function and the gradient of $J(\theta)$.

  Despite the many achievements of SGD optimization algorithms, there are still some thorny issues that need to be addressed. For example, first, the choice of the appropriate learning rate is very critical. Second, the learning rate is constant during training and is the same for all parameters in the NN. Finally, it is easy to fall into a large number of local optimal solutions or saddle points during the optimization of highly non-convex error functions. Several other methods have been proposed to address these issues.

- **Momentum method**

  The momentum method is proposed to accelerate SGD by guiding in the relevant direction and slowing down the oscillations in the non-relevant direction. This is achieved by adding the coefficient vector of one update step to the next update vector.

$$v_t = \gamma v_{t-1} + \eta \bigtriangledown_\theta J(\theta) \tag{2.69}$$

  The parameters are updated by $\theta_{t+1} = \theta_t - v_t$. The momentum term γ defaults to 0.9. Since the momentum term γ expands the update in the dimension where the gradient points in the same direction and shrinks the update in the dimension where the gradient direction changes. This avoids excessive parameter updates, accelerates orientation, converges stably, and reduces oscillations.

- **Adaptive gradient (Adagrad) and RMSprop**

  The Adagrad Gradient (Adagrad) method [51] is introduced for processing sparse data, and it makes it possible to have a set of adaptive adjustment of the learning rate for different problems by recording the forward direction and distance during each iteration, i.e., different parameters are required for different learning rates. On the basis of SGD, the regularizer is applied to Equation 2.69, so the update of the parameters is as follows:

$$G_t = \sum_0^t |\bigtriangledown_\theta J(\theta_t)|^2 \tag{2.70}$$

$$\theta_{t+1} = \theta_t - \frac{\eta}{\sqrt{G_t + \epsilon}} \bigtriangledown_\theta J(\theta_n) \tag{2.71}$$

where ϵ is a small constant to prevent the denominator from being zero. And G_t denotes the accumulation of squared gradients about the parameter θ_t.

The advantage of AdaGrad is that it makes more efficient use of information from small gradients and converges more efficiently than the standard SGD algorithm. However, the disadvantage of AdaGrad is that it requires a given initial global learning rate. Therefore, if the set global learning rate η is too large, it will lead to unstable optimization, while if η is too small, the learning rate may stall at the point of reaching the optimum.

Another adaptive learning rate method, RMSprop, was proposed to address the need for Adagrad's rapidly decreasing learning rate.

$$v_t = \gamma v_{t-1} + (\gamma - 1) \left[\bigtriangledown_\theta J(\theta_t)\right]^2, \tag{2.72}$$

$$\theta_{t+1} = \theta_t - \frac{\eta}{\sqrt{v_t + \epsilon}} \bigtriangledown_\theta J(\theta_t) \tag{2.73}$$

- **Adam**

The essence of the Adam algorithm [59] is the combination of the momentum method and the RMSProp algorithm. This algorithm comprehensively considers the attenuation average value of the first-order moment estimation, and modifies RMSProp with an adaptive learning rate.

$$m_t = \beta_1 m_{t-1} + (\beta_1 - 1) \bigtriangledown_\theta J(\theta_t) \tag{2.74}$$

$$v_t = \beta_2 v_{t-1} + (\beta_2 - 1) \left[\bigtriangledown_\theta J(\theta_t)\right]^2 \tag{2.75}$$

where m_t is the average value of the first-order moment gradient; v_t is the non-central difference value of the second-order moment gradient. The initial values are $m_0 = 0$ and $v_0 = 0$. At the initial stage of the iteration, m_t and v_t have a bias towards 0, resulting in β_1 and β_2 being close to one. Therefore, bias corrections for first-order and second-order momentum are required.

$$m_t^{'} = \frac{m_t}{1 - \beta_1} \tag{2.76}$$

$$v_t^{'} = \frac{v_t}{1 - \beta_2} \tag{2.77}$$

The above formula can be used to update the parameters, which gives rise to the Adam update rule:

$$\theta_{t+1} = \theta_t - \frac{\eta}{\sqrt{v_t^{'} + \epsilon}} m_t^{'} \tag{2.78}$$

It is recommended that $\beta_1 = 0.9$ and $\beta_2 = 0.999$ [107]. Since Adam performs well in practice compared to other adaptive learning methods, Adam was adopted as the optimization algorithm in Chapter 4.

Automatic Differentiation

In PINN, we have to solve the differential equations, which is the basis for implementing the physical constraints. This is done with the Automatic differentiation (AD).

In general, methods for solving differences in computer programs can be divided into four categories: Manual differentiation, Numerical differentiation, Symbolic differentiation and AD. Specifically, the manual differentiation is to first derive the formula for calculating the derivative of the objective function by hand based on the variables, and then program the implementation. This method is time-consuming and error-prone. Therefore, numerical differentiation and symbolic differentiation are often used. Numerical differentiation usually uses differences to compute an approximation of the derivative. And the result of symbolic differentiation is an expression of the derivative function. Symbolic differentiation is used to solve formulas in mathematics.

AD is an intermediate method between symbolic and numerical differentiation. As we know, numerical differentiation emphasizes direct substitution to solve the problem at the beginning, while symbolic differentiation emphasizes direct algebraic solution before final substitution. And in AD, symbolic differentiation is applied to basic functions, such as constant, exponential, power, trigonometric and logarithmic functions, and then numerical substitution is performed, preserving intermediate results, and finally applied to the whole function. It is quite flexible in its application and the differential solution process can be completely hidden from the user, so the method is widely used.

Chapter 3

In silico modeling for personalized stenting in coarctation

Patients with coarctation of the aorta may suffer from different CVD due to local stenosis and altered hemodynamics in the aorta. Stent intervention is a recommended treatment to reduce the pressure gradients and restore blood flow therein. However, a remaining challenge for physician is to select the optimal stent before treatment. In this chapter, a new strategy based on MRI and CFD for stent planning is presented. In Section 3.1, I focus on completing image-based in silico modeling for personalized stent implantation. The impact of turbulence modeling methods on the accuracy of fluid simulation is also discussed. Section 3.2 is a supplementary material on virtual aortic deformation.

3.1 In Silico Modeling for Personalized Stenting in Coarctation

The following is a reprint of the published article "Dandan Ma, Yong Wang, Mueed Azhar, Ansgar Adler, Michael Steinmetz, Martin Uecker. In silico modeling for personalized stenting in aortic coarctation. Engineering Applications of Computational Fluid Mechanics, 16(1), 2056-2073 (2022). doi: 10.1080/19942060.2022.2127912."

DM designed the project under the guidance of MU. Specifically, DM designed and conducted all experiments under the guidance of MU. MA and AA provided assistance during the experiments. With the help of YW, DM performed CFD simulations and analyzed the results. Patient images and medical theory support were provided by MS. DM wrote most of the manuscript, and all authors contributed to the preparation of the manuscript.

Layout and reference numbering are adjusted, and there ware no substantial changes in content.

Abstract

Stent intervention is a recommended therapy to reduce the pressure gradient and restore blood flow for patients with coarctation of the aorta (CoA). A remaining challenge for physician is to select the optimal stent before treatment. Here, we propose a framework for personalized stent intervention in CoA using in silico modeling, combining image-based prediction of the aortic geometry after stent intervention with prediction of the hemodynamics using computational fluid dynamics (CFD). Firstly, the blood flow in the aorta, whose geometry was reconstructed from magnetic resonance imaging (MRI) data, was numerically modeled using the lattice Boltzmann method (LBM). Both large eddy simulation (LES) and direct numerical simulation (DNS) were considered to adequately resolve the turbulent hemodynamics, with boundary conditions extracted from phase-contrast flow MRI. By comparing the results from CFD and 4D-Flow MRI in 3D-printed flow phantoms, we concluded that the LBM-based LES is capable of obtaining accurate aortic flow with acceptable computational cost. In silico stent implantation for a patient with CoA was then performed by predicting the deformed geometry after stent intervention and predicting the blood flow. By evaluating the pressure drop and maximum wall shear stress, an optimal stent is selected.

3.1.1 Introduction

Coarctation of the aorta (CoA) refers to a local narrowing of the aortic arch. It makes up 6 - 8% of all congenital heart diseases [99], and is often associated with other cardiovascular diseases, such as aortic arch hypoplasia, subaortic stenosis, ventricular and atrial septal defects [46, 104, 4]. The coarctation leads to high blood pressure and thus heart damage. Stent intervention, which is generally performed based on clinical experience without theoretical guidance, is a recommended therapy to reduce the pressure gradient and restore blood flow.

With increasing computational power, in silico modeling is emerging as a promising tool to help clinicians with intervention planning and to evaluate the outcome of therapies, such as stenting for intracranial aneurysm [144, 13], abdominal aortic aneurysm [8], and type-B aortic dissection [21, 53]. By taking personalized information as input, modeling also supports the design of patient-specific medical implants [72].

For in silico modeling of personalized stent intervention in CoA, a protocol for virtual geometry deformation [85] and a validated numerical method to accurately predict the blood flow in the aorta are required. Regardless of the erythrocytes, leukocytes, and platelets in blood, the flow in the aorta is normally modelled as Newtonian fluid [93] considering the relatively large Reynolds number Re, which is proportional to the flow velocity and aorta diameter and inversely proportional to the blood viscosity. Computational fluid dynamics (CFD) [127] plays an important role in biomedical engineering applications, such as drug delivery [3] and understanding of carotid stenosis [57, 56] and aortic dissection [25, 24]. Due to the personalized and complex 3D geometry and jet flows induced by heart contraction and local narrowing, laminar flow, turbulent flow and transition between them may coexist spatiotemporally [121, 64]. Thus, to accurately resolve such aortic flow, both turbulence and complex geometry should be considered in CFD simulations. Three approaches, including Reynolds-averaged Navier–Stokes equations (RANS), large eddy simulation (LES), and direct numerical simulation (DNS), are typically used for turbulence modeling. From RANS to DNS, both the accuracy and computational demand increases due to more and more details that need to be resolved.

So far, mainly RANS and LES were used to study aortic flow in literature [16]. With a transitional model, RANS was adopted to resolve flows in patient-specific thoracic aortic aneurysm by Tan et al. [128] and aortic dissection by Cheng et al. [25, 24]. Simulations were carried out using ANSYS CFX, a commercial finite volume-based solver. Kouseral et al. studied flow stability in a normal aorta using the same numerical method, and compared their numerical results with experimental data from in vivo magnetic resonance imaging (MRI) [62]. They concluded that the RANS based shear stress transport transitional model was capable of capturing the correct flow state when low inflow turbulence intensity (1.0%) was specified. Miyazaki et al. validated three CFD models for aortic flows in the aorta of a healthy adult and a child with double aortic arch [76]. Laminar, LES and the renormalization group

(RNG) k-ε model were considered and compared. Simulations were performed using another finite volume-based solver, ANSYS Fluent. Their results show that the RNG k-ε model has the highest correlation with data from 4D flow MRI. Recently, Manchester et al. used LES to study the blood flow in patient-specific aorta with aortic valve stenosis [68]. Here, the finite volume based open-source library OpenFOAM, was used. After investigating the fluctuating kinetic energy, wall shear stress (WSS) and energy loss, they concluded that turbulence played an important role in aortic hydrodynamics.

It should be noted that severe turbulence will be encountered in CoA due to a more complex geometry and larger Re, which might lead to higher requirements on the CFD method. The aforementioned conventional CFD methods are based on discretizations of macroscopic governing equations, such as the Navier-Stokes (NS) equations. Alternatively, the lattice Boltzmann method (LBM) is based on the mesoscopic Boltzmann equation and has multiple advantages, including simple handling of complex geometric shapes, ease of programming, and suitability for parallelization [63, 44, 23]. Therefore, the LBM is increasingly used for the simulation of turbulent flow [22] and biological fluid flows [136]. Hennt et al. simulated the unsteady blood flow in a patient-specific geometry with a moderate thoracic aortic coarctation, and demonstrated that the LBM based DNS was capable of resolving such complex flow [45]. Recently, Mirzaee et al. studied aortic flows for 12 patients with CoA using the LBM based LES, particularly with the Smagorinsky turbulence model [75]. A reasonable agreement for pressure drop between the numerical results and the catheter measurements was achieved. Nevertheless, to guide in silico stent intervention for CoA, a comprehensive validation for the LBM based LES for complex flow is still missing.

Since the 1970s and 1980s, MRI has become an important clinical and scientific tool that is widely used for diagnosis, monitoring of treatment procedures, and for biomedical research [70]. Compared with X-ray and computed tomography, one of the advantages of MRI is the use of non-ionizing radiation [73, 65]. In addition to obtaining anatomical information, MRI can also be used for quantitative flow measurements using phase-contrast imaging [80, 90, 118] including measurement of aortic blood flow [76, 109].

In this study, we developed a framework for personalized stent intervention in CoA using in silico modeling, combining CFD and image-based virtual geometry deformation. Such framework can provide the optimal stent plan based on flow simulations, before clinical intervention. A comprehensive validation of the LBM based LES for aortic flow was also performed. Geometries for a patient-specific aorta with CoA, before and after stent intervention, were considered and physical phantoms were created using 3D printing for use in MRI flow experiments. Flow measurements obtained with MRI scans were then used as boundary conditions for simulations. Obtained numerical results using LBM based LES and DNS were then compared with experimental 4D Flow data. To further validate the LBM based LES,

we also compared within vivo data. We demonstrated that LES is capable of accurately simulating complex aortic flow and further applied it for in silico stent implantation. Details of the methodology are given in Section 2. Numerical results and experimental measurements for aortic flows are presented and compared in Section 3. The application for stent selection is provided in Section 4. Discussion, limitations of the current work and future works can be found in Section 5. A conclusion is given in Section 6.

3.1.2 Methodology

MRI Experiments

The anatomical structure of the aorta and the flows therein were acquired by MRI, which provided realistic geometries and boundary conditions for CFD simulations. Comparison between CFD and phase-contrast flow MRI for flows in 3D-printed phantoms and in vivo aorta were performed respectively.

For the phantoms, the 3D anatomies of the heart and aorta of a 14-year-old patient with CoA, before and after stent intervention, were reconstructed from images obtained by a Magnetom Skyra 3T (Siemens Healthineers, Erlangen, Germany). The stent (diameter = 12 mm) used in this patient was a covered Cheatham-platinum (CP) stent made of platinum-iridium (NuMed, Orlando, USA). The sequence parameters are listed in Table 1. Using ITK-SNAP [91], the geometry that starts from the aortic root and ends above the diaphragm was segmented based on the grey values and exported as STL file. The main branches, such as the right subclavian, the left subclavian, the right carotid artery and the left carotid artery, were included. To have an uniform surface mesh, the generated geometries were then remeshed using Autodesk Meshmixer [113]. The schematic diagram of the experiment is shown in Figure 3.1. Two aortic models, including the pre-interventional and post-interventional geometries, were printed using the Stratasys' high-end 3D laser printer Connex 3 using biocompatible MED610 as material. The phantoms were connected to a pump. Forced water flows therein were then measured using 4D PC MRI [70, 33, 97]. The sequence parameters can be found in Table 1 and Table 2. Every case was measured three times with about 30 minutes per measurement. The averaged flow fields were then used for comparison.

For the in vivo validation, the aortic blood flow of a 3-year-old patient, was obtained using a 2D flow sequence instead of a 4D flow sequence, to reduce the duration of measurement. In the 2D measurement, the through-plane velocity of the flow was measured in two planes located in the ascending aorta and descending aorta respectively. All in vivo measurements were made with the use of ECG triggering and respiratory gating. The in vivo measurement was performed using the same MRI scanner as the phantom experiments and more details can be found in Table 3. For further CFD simulation, the aortic geometry was segmented and reconstructed using the same procedure as mentioned above.

TABLE 3.1: MRI sequences used for the flow-phantom study: In vivo MRI scans were performed pre and post intervention to obtain the anatomical structure. These geometries were used for 3D-printing a phantom then used for 4D-flow MRI measurements.

	Geometry (pre)	Geometry (post)
Sequence type	3D FLASH (TWIST)	3D T1 weighted FLASH
Acceleration	3×2	2×2
Matrix size	352×246	448×252
Number of slices	80	88
Slice thickness (mm)	1.30	1.20
Pixel size (mm^2)	1.02×1.02	0.89×0.89
Repetition time (ms)	2.75	3.70
Echo time (ms)	1.00	1.31
Flip angle (°)	20	25

TABLE 3.2: 4D-flow sequences used for the flow-phantom study.

	4D flow MRI (pre)	4D flow MRI (post)
Sequence type	3D Cartesian FLASH	3D Cartesian FLASH
Matrix size	384×504	416×364
Number of slices	144	144
Slice thickness (mm)	0.77	0.77
Pixel size (mm^2)	0.77×0.77	0.77×0.77
Repetition time (ms)	36.40	70.40
Echo time (ms)	4.61	7.46
Flip angle (°)	7	7
Velocity encoding (cm/s)	50	40

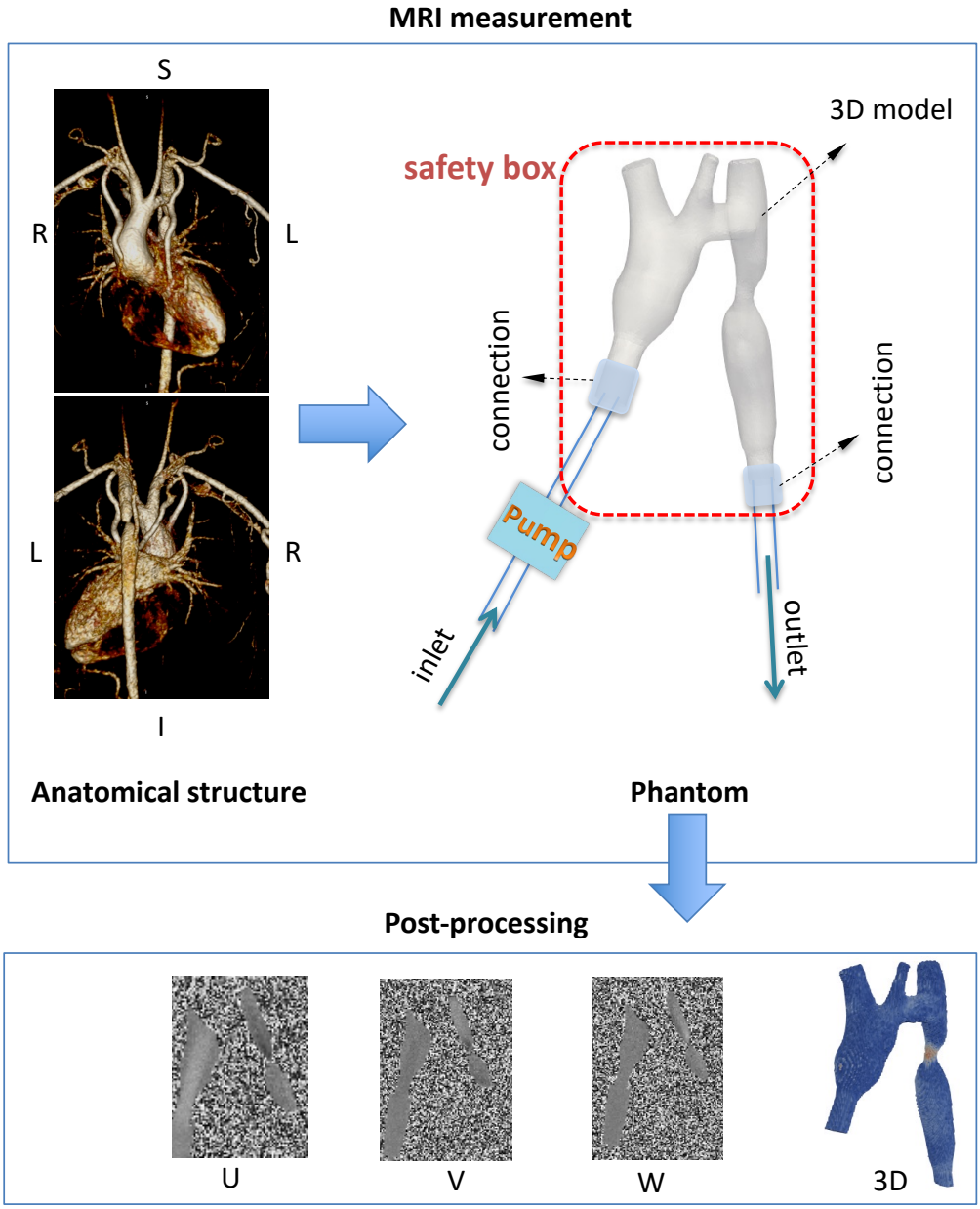

FIGURE 3.1: Schematic diagram of the phantom measurement. Top left: anatomical 3D structures of a heart and great vessels (with CoA) were segmented and reconstructed based on MRI images to obtain the geometry of the aorta. Top right: 4D-Flow MRI of 3D printed phantoms connected to a pump were performd for pre-interventional and post-interventional geometries. Bottom: 4D-Flow MRI yields three components (U, V, W) of the instantaneous flow velocity at each voxel.

TABLE 3.3: MRI sequences for geometry and 2D flow for in vivo validation.

	Geometry	2D flow MRI
Sequence type	3D T1 weighted FLASH	2D T1 weighted FLASH
Acceleration	3×2	2 × 2
Matrix size	320×260	192×119
Number of slices	88	30
Slice thickness (mm)	1.00	5.00
Pixel size (mm^2)	1.00×1.00	1.56×1.56
Repetition time (ms)	312.01	39.44
Echo time (ms)	1.64	2.67
Flip angle (°)	20	20
Velocity encoding (cm/s)	-	200

Numerical Modeling

The CFD simulations in this study were performed using the LBM, which is based on the kinetic theory, particularly the Boltzmann equation which describes the movements of fluid particles [63, 44, 23, 43]. For simulations, the space and time are discretized into finite nodes and time steps. Starting from an initial state, the configuration of the fluid particles at each time step evolves in two sub-steps, streaming and collision. During streaming, fluid particles at a node move to the neighbouring nodes along specified discrete directions as defined by the lattice. The streamed particles at a node collide with each other and change their velocity distribution functions [12]. For 3D flows, the most popular lattice is the D3Q19, which is used in this work.

Different operators, such as the single-relaxation time BGK [98] and the multi-relaxation-time (MRT) operators [30], can be used to approximate the particle collision. We chose the MRT operator due to its better numerical stability. The governing equation for the LBM with MRT operator reads

$$f_i\left(\boldsymbol{x}+\boldsymbol{e}_i\Delta t, t+\Delta t\right)-f_i(\boldsymbol{x},t)=\Lambda_{ij}(f_j^{eq}(\boldsymbol{x},t)-f_j(\boldsymbol{x},t)), \tag{3.1}$$

in which f_i is the particle velocity distribution function along the ith direction; $\boldsymbol{x}$ and t are the spatial coordinate and time respectively; Δt is time step; $\boldsymbol{e}_i$ is the discrete velocity of the lattice along the ith direction. The right-hand side of Equation (3.1) represents the collision process in momentum space. $\Lambda_{ij} = \boldsymbol{M}^{-1}\boldsymbol{S}\boldsymbol{M}$; $\boldsymbol{M}$ is a given transformation matrix for the lattice; $\boldsymbol{S}$ is a diagonal matrix. Macroscopic parameters, such as the fluid density, pressure and velocity, are moments of f_i.

The left-hand side and right-hand side of Equation (3.1) represent the streaming

and the collision processes respectively. The simplicity of this equation implies that the LBM is readily parallelizable as the non-local streaming is linear while the non-linear collision is local [63, 44, 23]. Thus, the LBM is increasingly used for turbulence modeling, especially DNS with high performance modern computers. Additionally, due to its particle feature, even with a simple Cartesian grid the LBM can resolve flow with complex geometry, such as the patient-specific aortas considered in this study.

The LBM based DNS and LES were investigated in this study, based on the open-source library Palabos [50]. DNS resolves the flow at all scales without empirical model in numerical experiments. As mentioned before, the calculation cost of DNS is very high especially for flows with large Reynolds number [79, 136]. Alternatively, LES explicitly solves large eddy current and implicitly calculates small eddies by using a sub-grid scale (SGS) model, thus balancing accuracy and computational cost. The Smagorinsky SGS model [117] was incorporated into the LBM in this study.

For all simulations, the inlet velocity with Poiseuille profile was specified at the ascending aorta. The flow rates were given based on MRI measurements and can be found in the following sections. Outlet boundary condition with a reference pressure was applied to the descending aorta. The curved aortic wall was assumed to be no-slip and treated with an extrapolation scheme [40].

3.1.3 Validation and Comparison

Phantom Experiments

The two phantoms filled with water were used in the MRI experiments and compared to CFD simulations of the same geometries. The main branch blood vessels were closed, to reduce their influence. Inlet and outlet of the geometries were extended artificially for the connection of the water pipe. Water is incompressible and Newtonian. Its density and kinematic viscosity are 1.0×10^3 kg/m^3 and 1.0×10^{-6}m^2/s, respectively. The averaged velocity at the inlet is 0.1 m/s. The geometries with triangular surface meshes are shown in Figure 3.2. Quantitatively, areas of the inlet planes and six specified cross sections, from ascending to descending aorta, are listed in Table 3.4. Locations of those sections can be found in the left panel of Figure 3.7.

First, a mesh independence test was performed. We considered at least four simulations with different spatial resolutions for each case, as shown in Figure 3.3 and Figure 3.4. The averaged kinetic energy $E = \frac{1}{2}\sum_{i=1}^{N} \mathbf{u}_i^2 / N$ in the whole computational domain was monitored. Therein, N is the number of lattices, $\mathbf{u}_i$ is the local velocity. Density (or mass) is almost constant thus not considered in the definition of E. A smooth temporal development of E can be found in all curves, as we gradually increased the inlet velocity from zero to the target value, for the purpose of better numerical stability. By comparing the curves after the statistical steady states and the corresponding computational costs, we chose the meshes with orange curves for

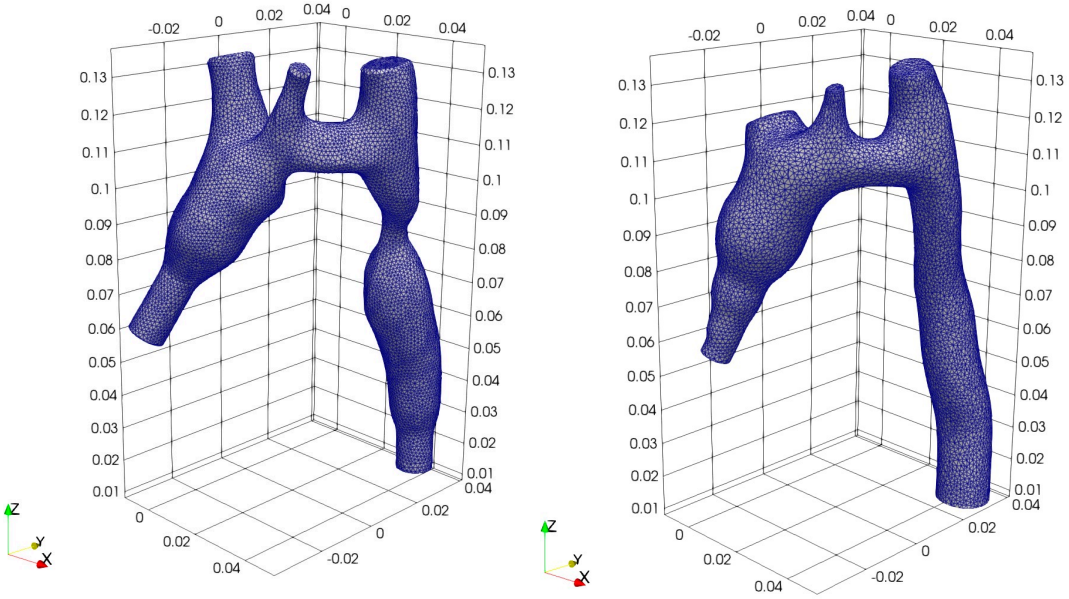

FIGURE 3.2: Aortic geometries with triangular surface meshes. Left: pre-interventional geometry; right: post-interventional one. Unit: m.

further simulations. In summary, 12.30 million (DNS) and 3.45 million (LES) lattice nodes were selected for the pre-interventional geometry and 5.12 million (DNS) and 1.25 million (LES) lattice nodes for the post-interventional one.

Due to the complex geometry, *e.g.* multiple plane curvatures and branches, blood flow in the patient-specific aorta is unsteady and complicated. Instantaneous velocity contours on a sagittal plane and a coronal plane in the pre-interventional geometry are given in Figture 3.5. Due to the relatively low temporal resolution of 4D flow MRI, here only results from DNS and LES are presented. It can be seen that the flow therein is turbulent. Because of the local narrowing in the stenosis, flow is accelerated in the pre-interventional geometry and the local Reynolds number on the stenosis plane is more than 2500. Jet flow, which leads to high blood pressure

TABLE 3.4: Areas of the specified aortic cross sections for geometries used in DNS.

	pre-interventional geometry	post-interventional geometry
Inlet (m^2)	9.404e-05	6.859e-05
No.1 (m^2)	4.175e-04	4.050e-04
No.2 (m^2)	8.625e-05	8.857e-05
No.3 (m^2)	1.380e-04	1.401e-04
No.4 (m^2)	2.725e-05	1.281e-04
No.5 (m^2)	2.544e-04	1.705e-04
No.6 (m^2)	2.4780e-04	1.194e-04

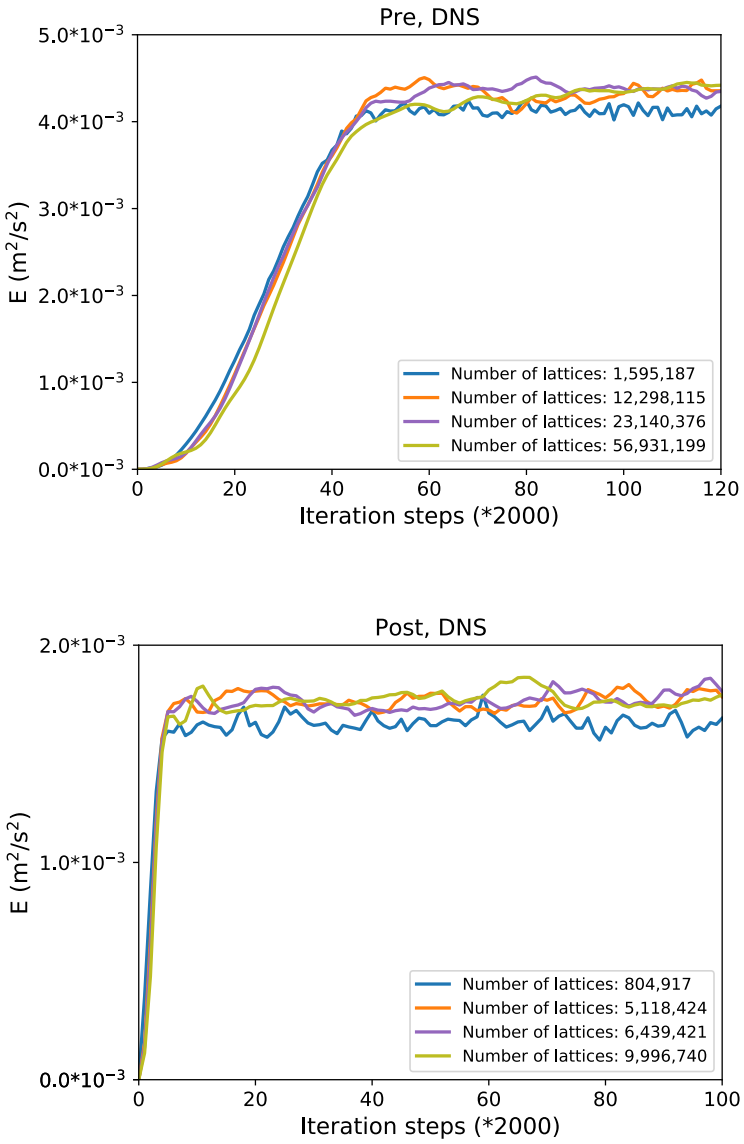

FIGURE 3.3: Mesh independence test (DNS). Time histories of the averaged kinetic energies in the aortic geometries. Top row is for the pre-interventional geometry; Bottom row is for the post-interventional geometry.

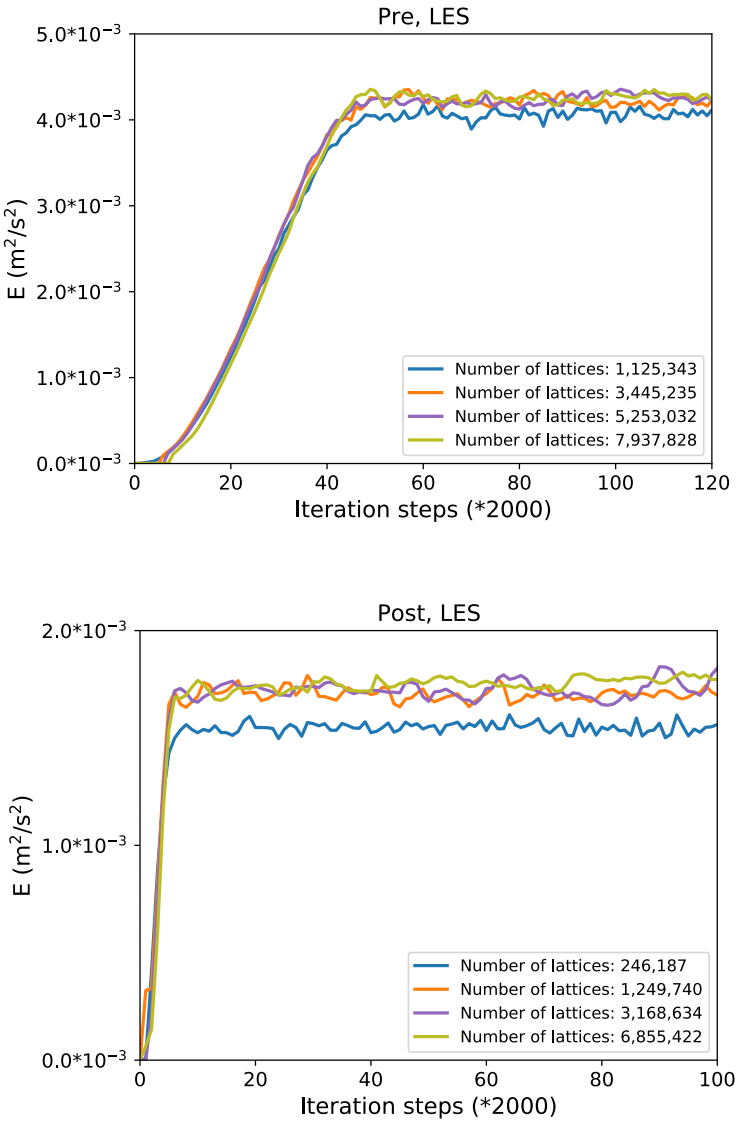

FIGURE 3.4: Mesh independence test (LES). Time histories of the averaged kinetic energies in the aortic geometries. Top is for the pre-interventional geometry; Bottom is for the post-interventional geometry.

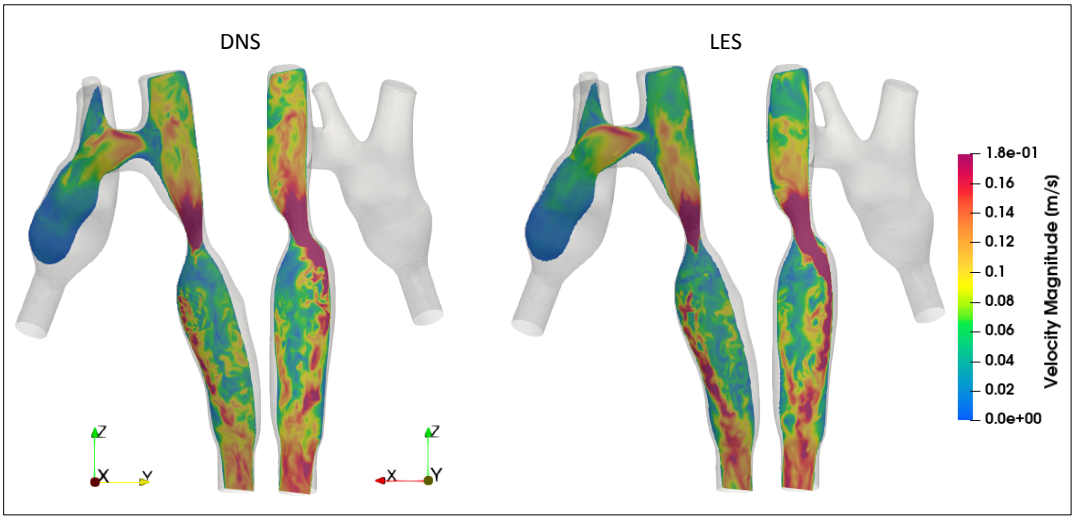

FIGURE 3.5: Instantaneous velocity contours on a sagittal plane and a coronal plane in the pre-interventional geometry of an aorta of a patient with CoA simulated by CFD. Left: DNS; right: LES.

and high wall shear stress (WSS), is observed. DNS provides more flow details due to higher spatial resolution.

As the flow is unsteady, temporal averaging was performed for both CFD and MRI results and the following comparison is based on the time-averaged flow fields. The main flow features can be found in Figture 3.6. The visualization of 3D streamlines and velocity vectors on the sagittal plane (insets) shows the complexity of the flow within the patient's aorta, especially where the stenosis occurs. Again, jet flow and recirculation are observed in the pre-interventional geometry in the streamlines and highlighted in the zoomed-in insets. Helical streamlines can also be found in all cases. For the MRI results, some streamlines start from the vessel wall as no-slip boundary condition is not guaranteed in MRI data. Nevertheless, all methods, including DNS, LES and MRI, resolved the main flow features. Moreover, as the aorta is deformed and flattened after stent implantation, the flow resistance in the post-interventional geometry is reduced. The pressure drop is reduced from 790 Pa (DNS) and 778 Pa (LES) to 9 Pa (DNS) and 8 Pa (LES), respectively. Those results indicate that stent implantation restored the aortic flow effectively.

Figure 3.7 presents quantitative comparison of mean velocity magnitude on six specified cross-sectional planes. These six planes, as shown in the left panel of Figture 3.7, represent the ascending, arch, pre-stenosis, on-stenosis, post-stenosis and descending of the aorta respectively. The mean velocity magnitude was calculated according to $\sum_{i=1}^{N} \sqrt{U_i^2 + V_i^2 + W_i^2} \ / N$, with N the number of points on a cross plane. It can be seen from the right panel of Figture 3.7 that the MRI results are a little larger than the numerical ones on planes Pre 2, Pre 3 and Pre 5. Using MRI results as reference, the relative deviations for LES and DNS are $4-28\%$ and $7-27\%$ respectively. Largest deviation can be found on Pre 5, mainly due to the difficulty for the MRI measurement induced by the recirculation after the stenosis. On Pre 4,

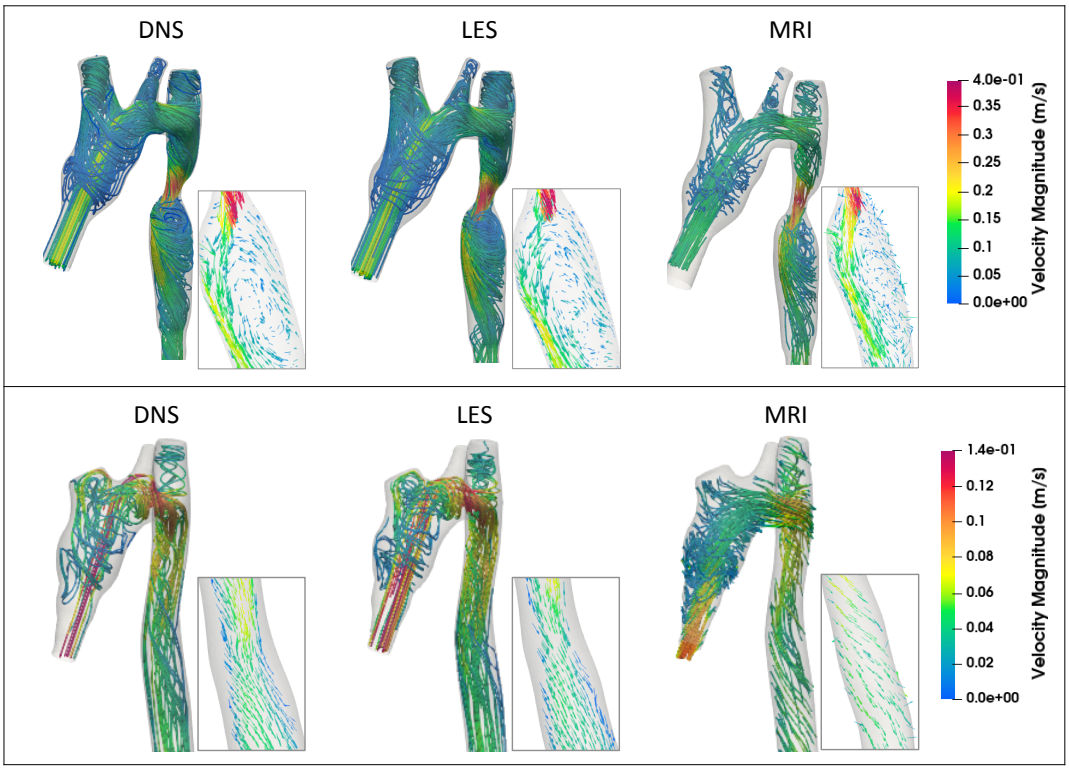

FIGURE 3.6: Streamlines of the flow computed with CFD simulations of the aorta compared to MRI measurements of the flow in the 3D-printed phantoms. The time-averaged flow is shown. The insets show the velocity vectors on the sagittal planes. Top: pre-interventional geometry; Bottom: post-interventional geometry.

MRI data is between the DNS (−4%) and LES (7%) ones. For the post-interventional geometry, CFD results agree with the experimental data well on all planes, with relative derivations less than 10%.

Velocity contours on those specified planes, in pre-interventional and post- interventional geometries, are given in Figures 3.8 and 3.9 respectively. Generally, flow patterns are qualitatively well-matched among LES, DNS and MRI for both geometries. Both LES and DNS provide more details and smoother fields due to higher spatial resolution compared with MRI. Discrepancy between the CFD results and MRI one is observed on Pre 4 and 5. We believe this is because of the complexity induced by the jet flow and recirculation after the stenosis, which is visualized in Figures 3.5 and 3.6. Nevertheless, the results from LES agree very well with those from DNS on all specified planes.

Velocities along the centerlines of the pre-interventional and post-interventional geometries were also compared. The centerline was extracted using the VMTK extension for 3D Slicer [94]. Since velocity in the pre-interventional geometry changes more acutely because of the stenosis, here only the results for pre-interventional geometry are presented. Discrete points along the centerline, starting from the ascending aorta after the artificial extension, are considered and can be found in the left panel of Figure 3.10. Velocity components and magnitude are given in the right panel. It can be seen that velocity components change sharply in the stenosis region which leads to a peak in the profiles of velocity magnitudes. Results from LES, DNS, and MRI agree with each other in most region of the aorta, except the coarctation. Similarly to Figure 3.8, discrepancy mainly happens in the MRI result around the stenosis, while good agreement between DNS and LES is always achieved. The flow

Based on the above comparisons, it can be concluded that CFD (LES and DNS) results agree with the data from 4D-Flow MRI. More information, such as pressure drop and WSS can be easily generated from the CFD results. Since LES needs less computational resources but provides acceptable accuracy, we conclude that LES is capable in resolving aortic flow and adopt it for the following research.

In vivo Validation

To further validate the numerical modeling, we also used in vivo measurements in addition to the phantom study. The patient-specific aortic flow was compared between LES and flow MRI. Considering the long measurement duration needed by 4D-Flow MRI [119], 2D flow MRI was used for the in vivo scans. Velocities, thus flow rates, on specified planes perpendicular to the main flow direction were measured with 2D phase-contrast flow MRI. The experimentally obtained flow rate on a plane in the acceding aorta is shown in the left panel of Figure 3.11. The two time instants, t_1 and t_2 during systole, were considered and their flow rates were used as inlet boundary condition for the LES simulations. The experimentally recorded velocity distributions in the descending aorta at these two instants were used for comparison.

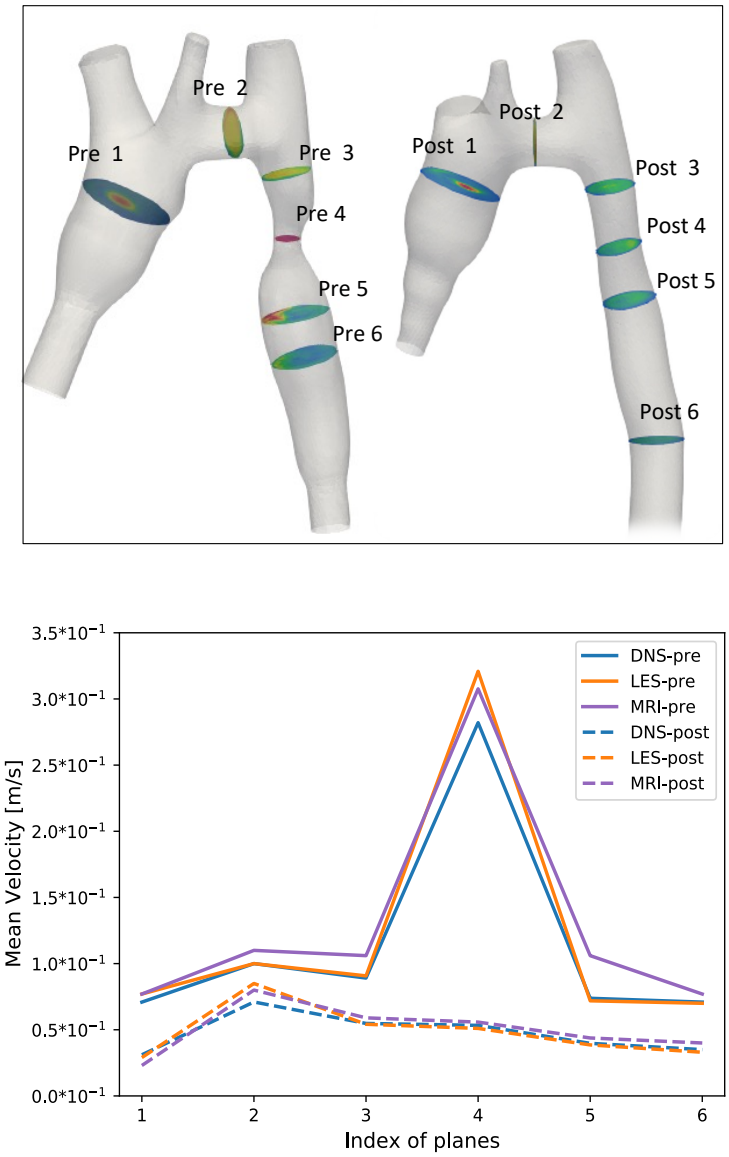

FIGURE 3.7: Comparison of mean velocity magnitude on specified planes for the pre-interventional and post-interventional aorta geometry. Left: six specified cross planes, including ascending, arch, pre-stenosis, on-stenosis, post-stenosis and descending of aorta. Right: The time-averaged mean velocities from 4D flow MRI and the CFD simulations.

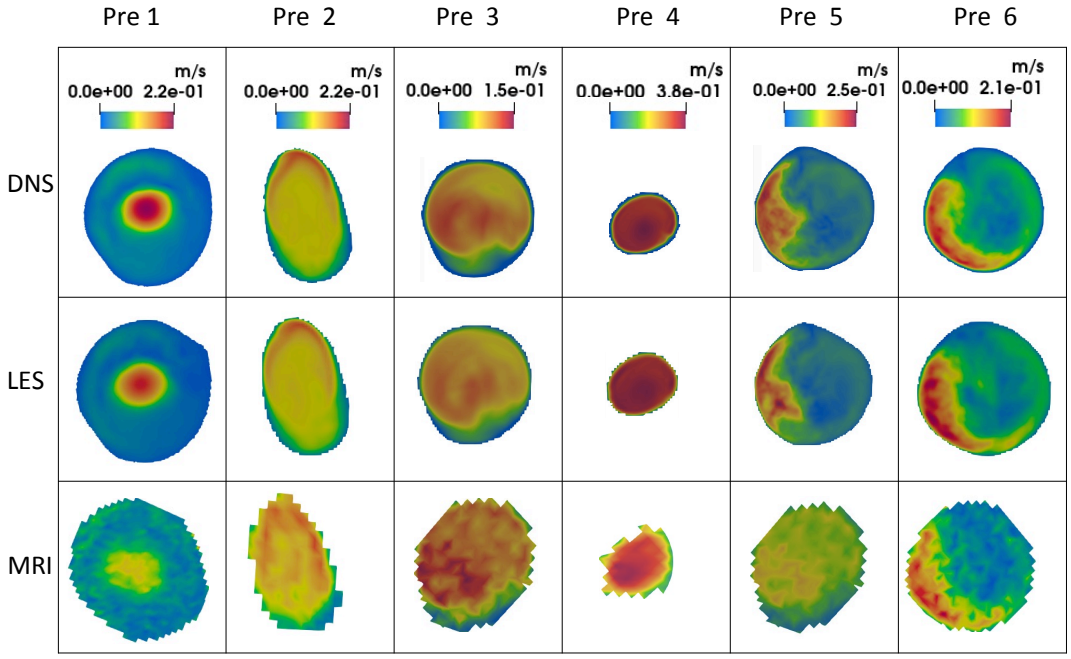

FIGURE 3.8: Flows in pre-interventional aorta. Velocity magnitude distributions were compared among CFD simulations and 4D Flow MRI on six planes as shown in Figure. 3.7. Time-averaged results.

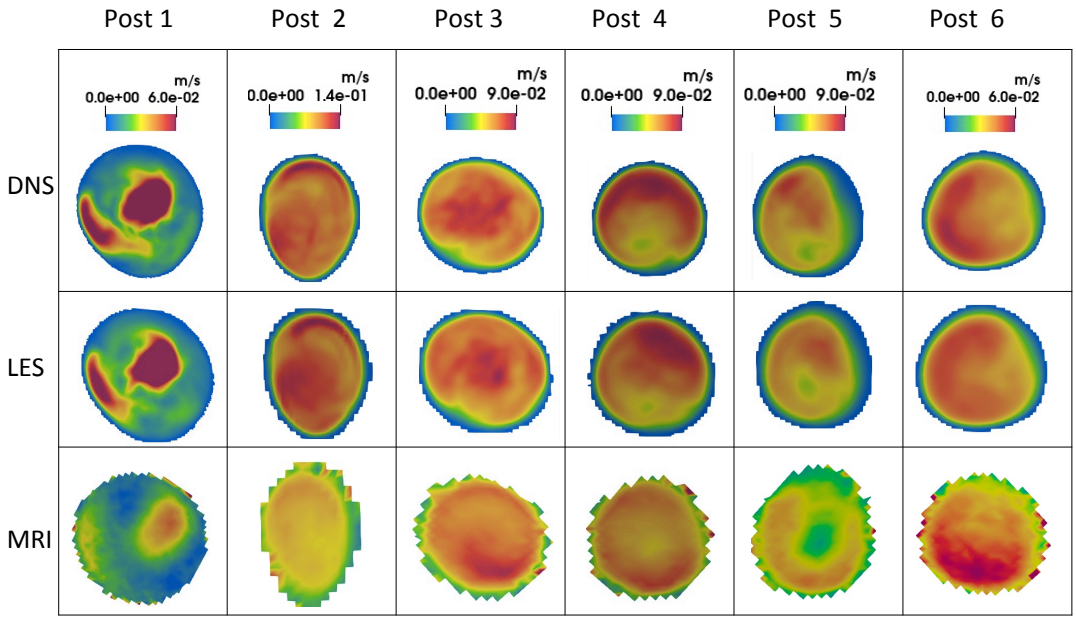

FIGURE 3.9: Flows in post-interventional aorta. Velocity magnitude distributions were compared among CFD simulations and 4D Flow MRI on six planes as shown in Figure 3.7. Time-averaged results.

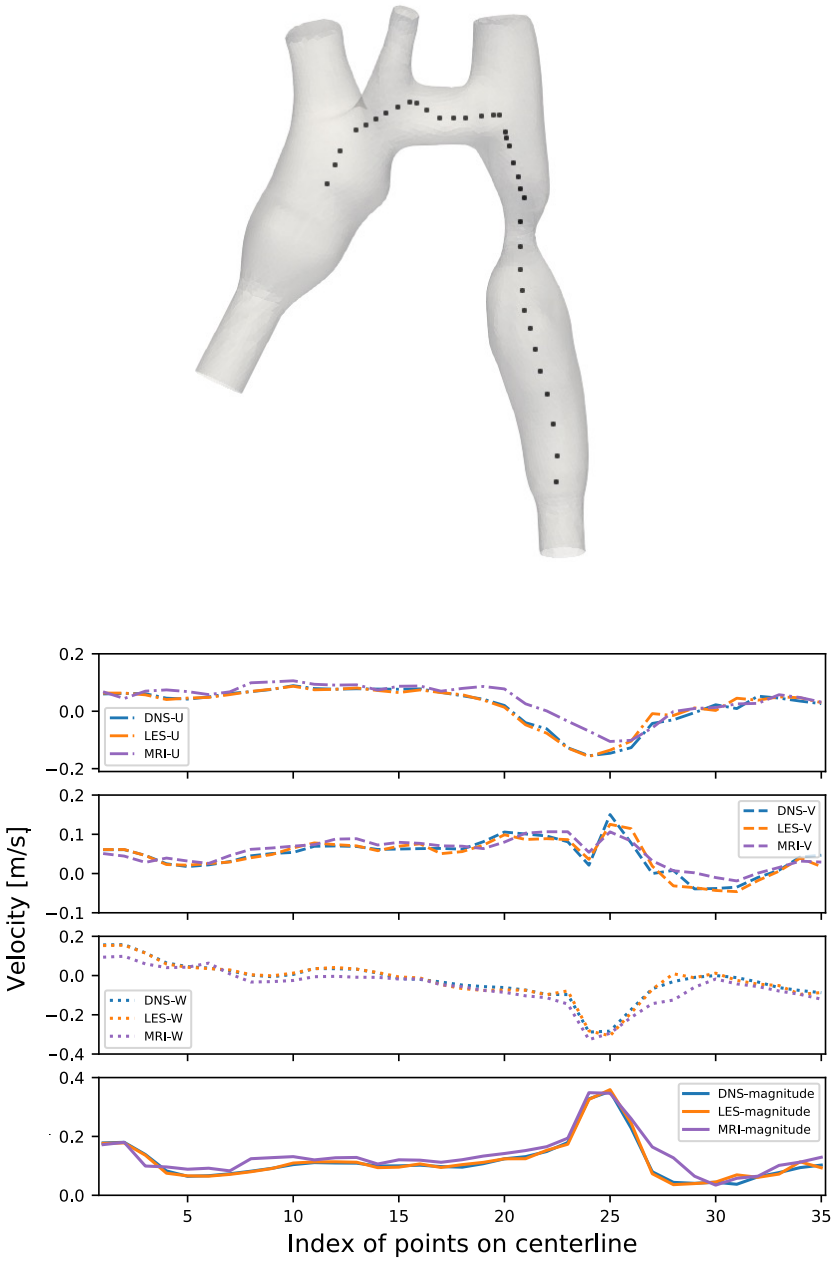

FIGURE 3.10: Comparison of flow velocity along the centerline of the pre-interventional aorta. Top: locations of the points starting from the ascending aorta. Bottom: from top to bottom, velocity components and magnitude. Time-averaged results.

In numerical simulations, the aortic geometry was segmented and reconstructed based on the MRI slices. The geometry extends from the aortic root to the descending aorta, and includes branch vessels as shown in Figure 3.11. Both the inlet and outlet planes were approximately circular after the geometry were remeshed and smoothed. We didn't consider the deformation of the aorta, or fluid-solid interaction, and assumed that the wall was not moving. A velocity profile based on the experimentally recorded flow rate was specified as inlet. Specifically, the flow rate Q_{in} was calculated according to $Q_{in} = \sum_{i=1}^{N} V_i \cdot S_i$. Here V_i is the pixel-velocity obtained from 2D flow MRI, S_i is the area of each pixel in the inlet plane, N is the total number of pixels in the inlet plane. A parabolic profile with the same amount of flow rate was then generated in Palabos as inflow boundary condition. A pressure boundary condition, with a specified reference pressure, was defined as outlet at the opening in the descending aorta, as velocity profile over there was unknown. Since the vessel branches were open in this test, the difference of flow rates between the inlet and outlet were assigned to the branches according to their cross areas [75, 95].

The time-averaged flow fields are given in the right panel of Figture 3.11. At t_1 (the instant with peak flow rate), the through-plane component of mean velocity from LES is 0.69 m/s, with relative deviation 8% in reference to the MRI result, 0.75 m/s. Similarly, at t_2, the through-plane component of mean velocities are 0.55 m/s (LES) and 0.49 m/s (MRI). Thus, good agreement between LES and MRI was achieved also in vivo. Moreover, LES with proper boundary condition could provide more flow details due to higher spatial resolution, as shown in both in vivo and phantom tests.

3.1.4 Application for Stent Selection

Geometry Deformation

The main motivation for silico stent implantation is to help clinicians to evaluate the surgical plans based on predicted results and to be able to select an optimal stent already before surgery. A fast virtual stenting approach proposed by Neugebauer et al. [85] was implemented in this work to generate virtually deformed geometries. Several parameters, such as the aorta bending resistance, aorta stiffness, stent stiffness, stent position and diameter were considered in this approach to represent the interaction between aorta and stent. The deformed geometry was then obtained based on the deformed centerline and deformed surface vertices, as shown in Figure 3.12 and 3.13.

A brief description of the procedure is given below. With image segmentation and reconstruction, one gets a STL file with triangular facets and vertices describing the aortic geometry. The original centerline L_{original}, obtained using the VMTK extension for 3D Slicer, is then modified to L_{deformed} according to

$$L_{\text{deformed}} = i \cdot L_{\text{original}} + (1 - i) \cdot L_{\text{reference}}, \tag{3.2}$$

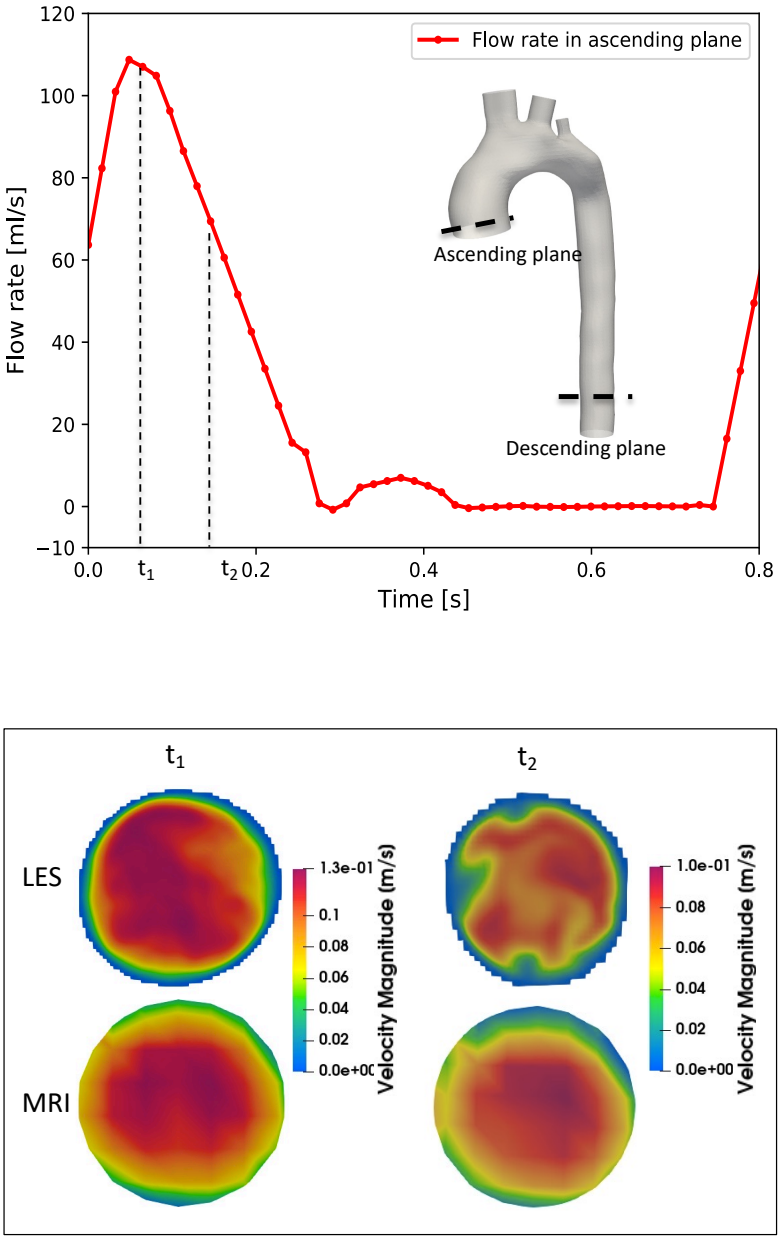

FIGURE 3.11: Comparison of in vivo aortic flow between LES and 2D flow MRI. Top: the experimentally recorded flow rate crossing the ascending plane; locations of the specified ascending plane and descending plane are given in the inset. Bottom: The through-plane component of velocity distributions on the descending plane at two different time instants during the cardiac cycle.

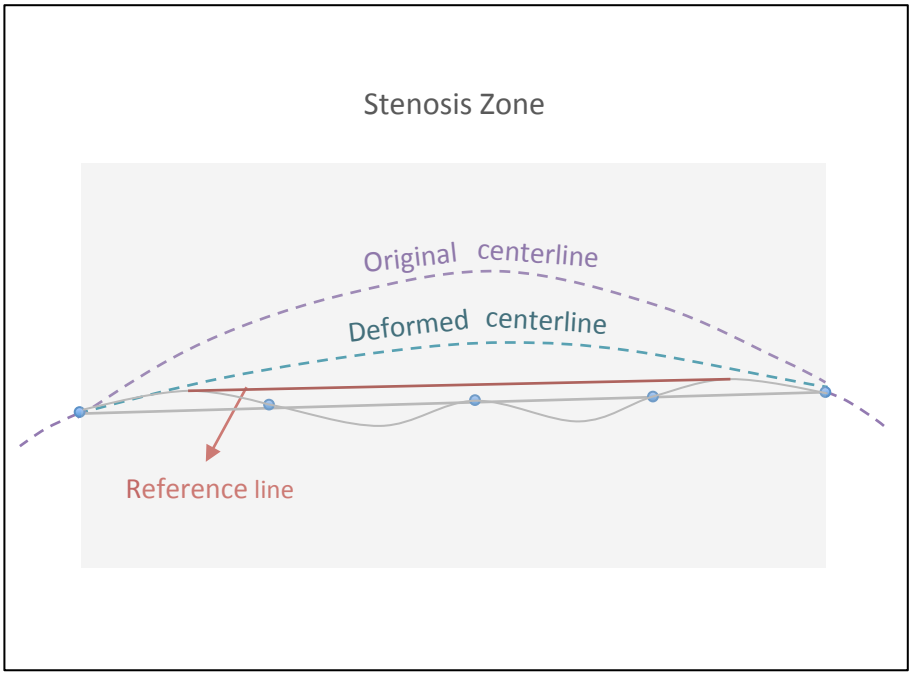

FIGURE 3.12: Virtual aortic deformation: the schematic diagram of geometrical centerline deformation.

As shown in Figure 3.12. Here $L_{\text{reference}}$ is a straight line closed by two splines, which ensure a smooth transition; $0 < i < 1$ is defined to represent the stiffness of stent and aorta, and the aorta bending resistance. The surface is then deformed based on the deformed centerline, as shown in Figure 3.13. A common orthogonal vector $\vec{v}_{\text{rotation}}$ is defined for both the original surface and the deformed one, and it reads

$$v_{rotation} = d_{original} \times v_{original} \tag{3.3}$$

for the original geometry. A vertex in the deformed surface can then be calculated based on

$$v_{deformed} = m \cdot (d_{deformed} \times v_{rotation}), \tag{3.4}$$

with m the scaling factor to adjust the diameter of aorta. More details can be found in [85] . Accordingly the deformed geometries after intervention with different stents are shown in Figure 3.14 and Figure 3.15.

More details can be found in Section 3.2

CFD Evaluation

The original pre-interventional geometry and its deformed versions can be found in Figure 3.14 and Figure 3.15. The deformed geometries were exported as STL files, which were remeshed and further imported into the CFD solver for flow simulation. The above validated LES was used to resolve the flows in the pre-interventional geometry and the virtually deformed ones. We used the same boundary conditions

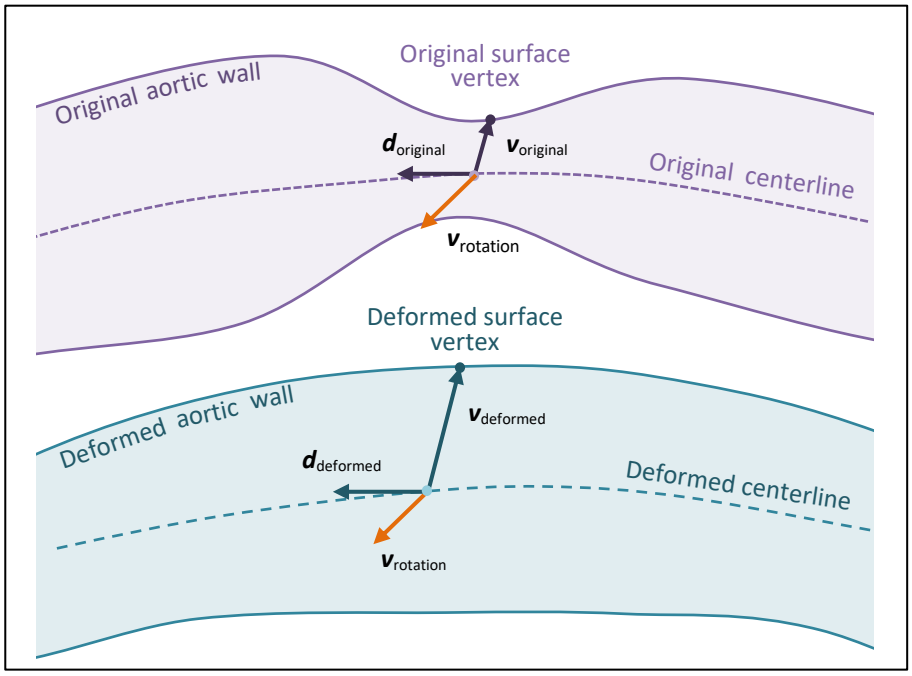

FIGURE 3.13: Virtual aortic deformation: the schematic diagram of geometrical surface vertex deformation.

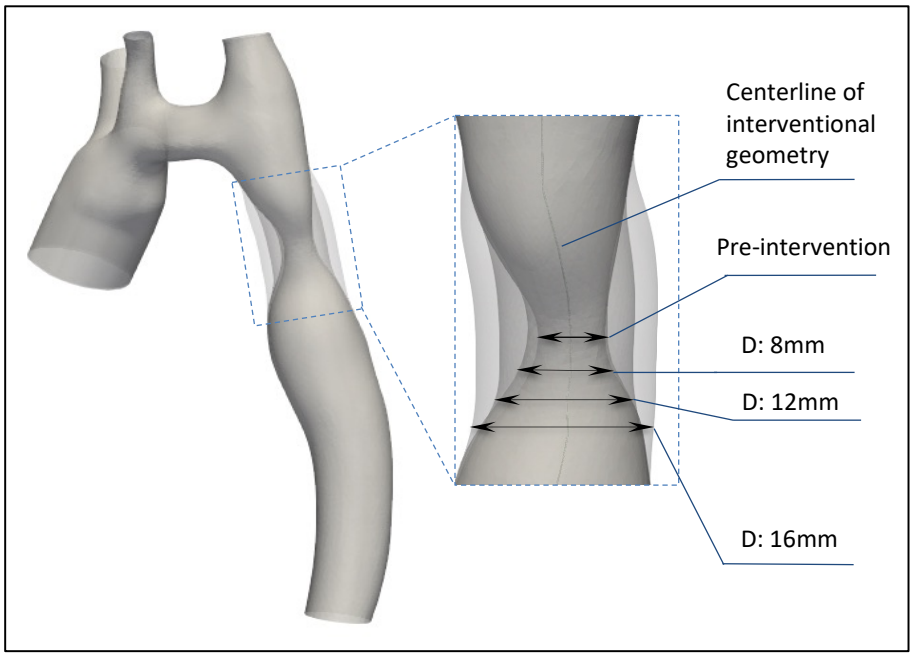

FIGURE 3.14: Virtual stent implantation: the visualization of geometrical deformation after visual stent implantation.

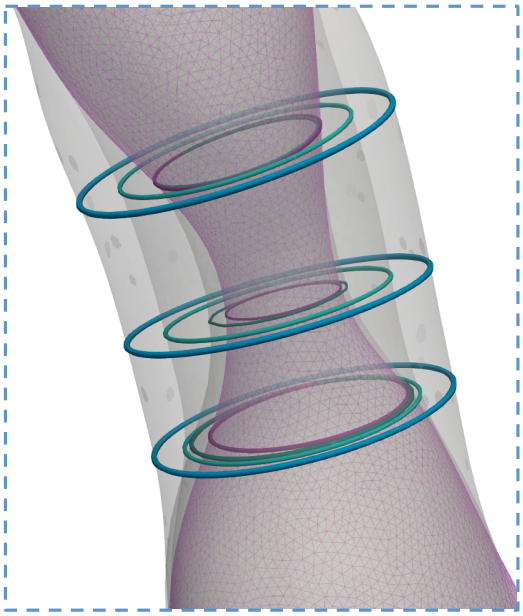

FIGURE 3.15: Virtual stent implantation: cross sections of the pre-interventional geometry, virtually deformed geometries with stent diameter 8 mm, 12 mm, and 16 mm respectively.

as mentioned in subsection 3.2, with flow rate 13.2 ml/s at the inlet. The numerically obtained results are presented in Figures 3.16 - 3.18.

The color coded streamlines in Figure 3.16 show that a stent with diameter 8 mm is inadequate to reduce the stenosis and jet flow with a large local flow still can be observed in the narrowing region. For stent diameter 12 mm or 16 mm, the jet flow disappears, with substantially reduced maximum velocity compared to the pre-interventional geometry. The velocity vectors, color coded with the velocity component W, on different cross sections are provided in Figure 3.17. It presents quantitative comparison of velocity distributions on on-stenosis planes within different geometries, as well as post-stenosis planes. On on-stenosis planes, the maximum velocities are 0.40 m/s, 0.35 m/s, 0.23 m/s and 0.11 m/s respectively, decreased significantly from the pre-interventional geometry to the deformed ones. On post-stenosis planes, the jet flow, which leads to locally high WSS, can be found in both the pre-interventional geometry and the deformed one with diameter 8 mm. A much more uniform on plane velocity distribution is achieved in the geometries with larger stent diameter.

The WSS distributions are given in Figure 3.18. WSS describes the mechanical force generated by blood flow on the vessel wall, thus plays an important role in chronic adaption and remodelling [49]. It is defined as $\tau_{y=0} = \mu \frac{\partial u}{\partial y} \mid_{y=0}$, where μ is the dynamic viscosity of the flow, u is the flow velocity along the wall and y is the height above the wall. As shown in Figure 3.18, high WSS is observed in the stenosis region in the pre-interventional geometry and the deformed one with stent diameter 8 mm. After the stenosis, high WSS is also found in a part of the descending aorta

FIGURE 3.16: Streamlines in the pre-interventional and virtually deformed aortas. Time-averaged results. From left to right: pre-interventional geometry, virtually deformed geometries with stent diameter 8 mm, 12 mm, and 16 mm respectively.

due to the impact of high-speed jet flow (see Figures 3.16 and 3.17 for reference). A stent with diameter 16 mm enlarges the stenosis most and therefor leads to the smallest WSS in the same region. However, as this stent is larger than the size of the aorta, it also leads to a relatively large WSS before the stent, compared to the case with stent diameter of 12 mm.

Stent Selection

To quantitatively compare the four cases with different stent diameter, the pressure drop and maximum WSS are given in Figure 3.19. It can be seen that the pressure drop is 119 Pa in the pre-surgical geometry, and is reduced to 34 Pa and 28 Pa in the geometry with stent diameter 12 mm and 16 mm respectively. For the maximum WSS on the aortic wall, the geometry with stent diameter 12 mm provides the smallest value, 1.07 Pa. It is understandable that a larger diameter stent results in less flow resistance thus smaller pressure drop, assuming that the aortic wall is always deformable. On the other hand, size of the aorta wall and its nonlinear response to possible strain should also be considered. If a stent is too large for the aorta, it is conceivable that in addition to flow there will be external mechanical force from the stent acting on the aortic wall.

Thus a stent with diameter 12 mm should be the optimal solution for the current patient-specific aorta, which agrees with the physicians' independent choice in this case.

We further compared the virtually deformed geometry based on this optimal stent with the post-interventional one reconstructed from MRI images in Figure 3.20. Centerlines for both geometries were obtained and the distance ($\leq$ 1.60 mm) between two centerlines is presented. Similarly, the spatial dependent diameters are

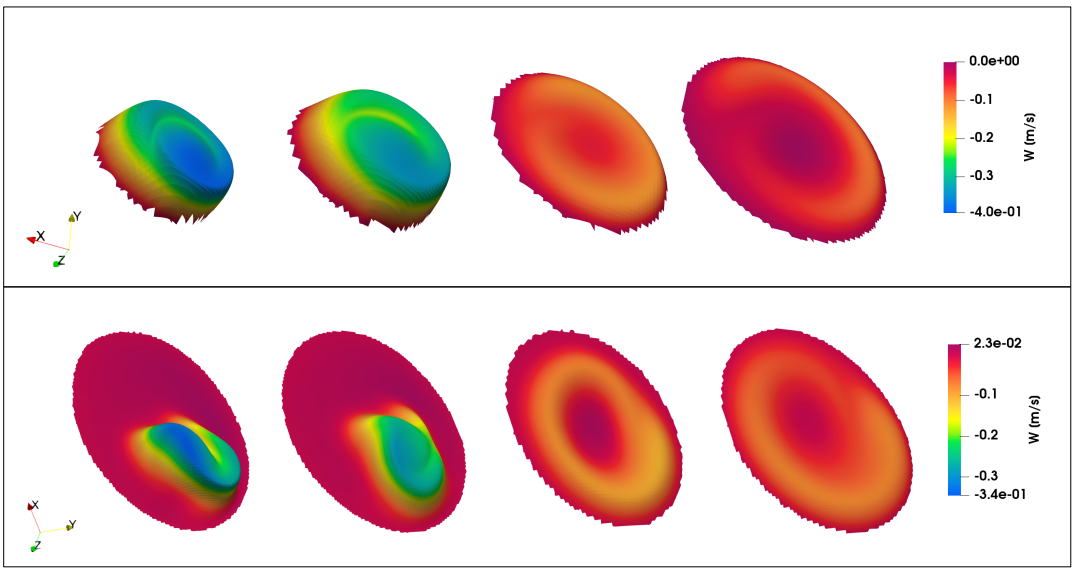

FIGURE 3.17: Velocity vectors, color coded with the component W, on different cross sections. Time-averaged results. Top, on-stenosis plane; bottom, post-stenosis plane. From left to right: pre-interventional geometry, virtually deformed geometries with stent diameter 8 mm, 12 mm, and 16 mm respectively.

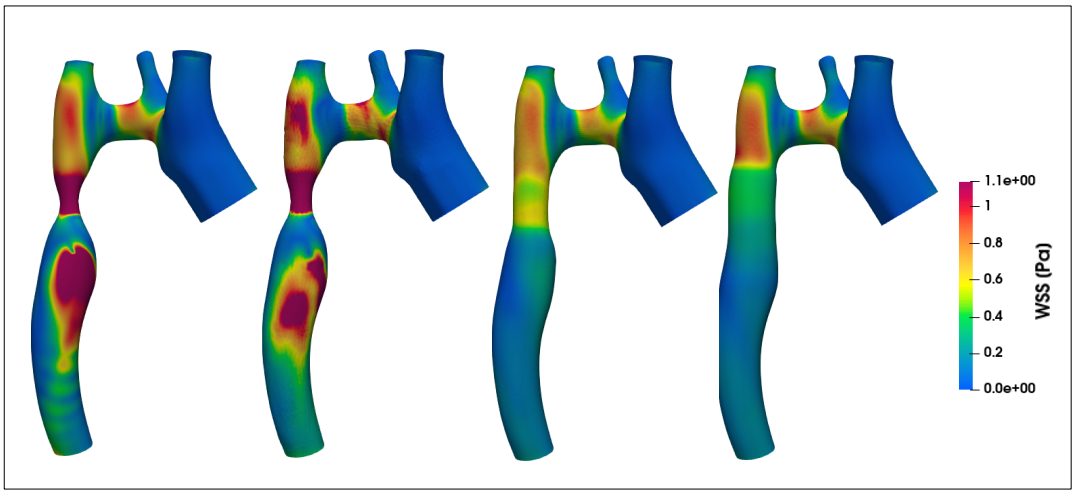

FIGURE 3.18: WSS on the pre-interventional and virtually deformed walls. Time-averaged results. From left to right: pre-interventional geometry, virtually deformed geometries with stent diameter 8 mm, 12 mm, and 16 mm respectively.

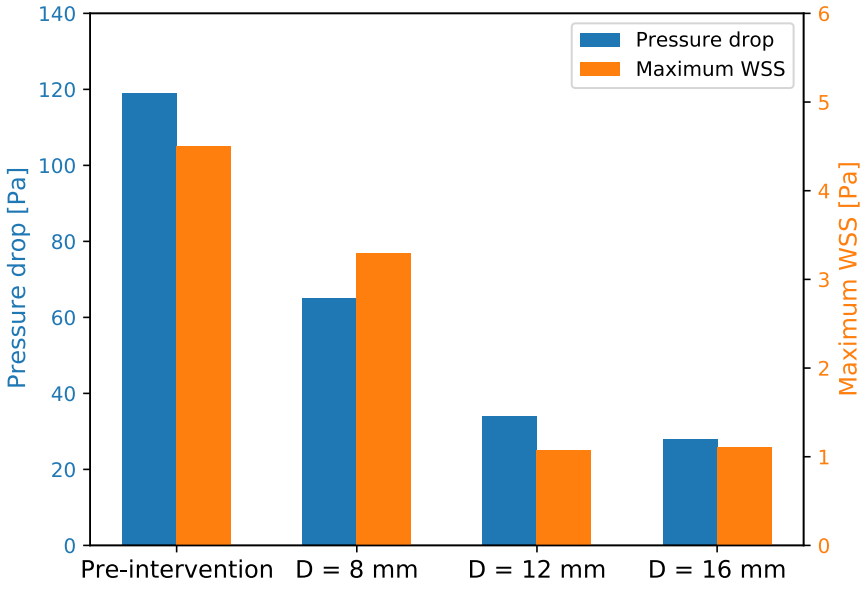

FIGURE 3.19: Quantitative comparison of pressure drop and maximum WSS in the aortas before and after deformation.

also given, with deviation less than 0.65 mm. It can be concluded that the virtually deformed geometry agrees with the clinically deformed one quantitatively. It should be noted that in this study the physicians chose a stent with diameter 12 mm independently and without input from the in silico modeling, which agrees with the prediction based on the combination of virtual geometry deformation and CFD simulation.

3.1.5 Discussion

Image-based in silico stent implantation [8, 21, 53, 85] and CFD [144, 13] together provide a new framework for stent planning and interventional procedure evaluation. Besides a protocol for virtual geometry deformation, a CFD method is needed to accurately resolve the flows in the aortic geometries. However, blood flow in patient-specific aorta is complicated [121, 64]. Laminar flow, turbulent flow and transition between them may coexist spatiotemporally. In our study, we firstly evaluated the accuracy of LES to predict such complicated flow. Two CFD methods, the LBM based LES and DNS, in cooperation with flow MRI, were considered. Both phantom and in vivo validations show that the LBM based LES, which keeps a balance between numerical accuracy and computational requirement, is a reasonable choice for resolving aortic flow. The validated LES was then used to predict the flows in virtually deformed geometries with different stent diameters. By comparing the flow fields, pressure drop, and maximum WSS, it was found that the optimal stent was the one with diameter 12 mm, which agrees with the physicians' independent choice.

To restore blood flow, in addition to numerical methods, accurate geometry and boundary conditions are also important. Based on MRI scans, aortic geometry can

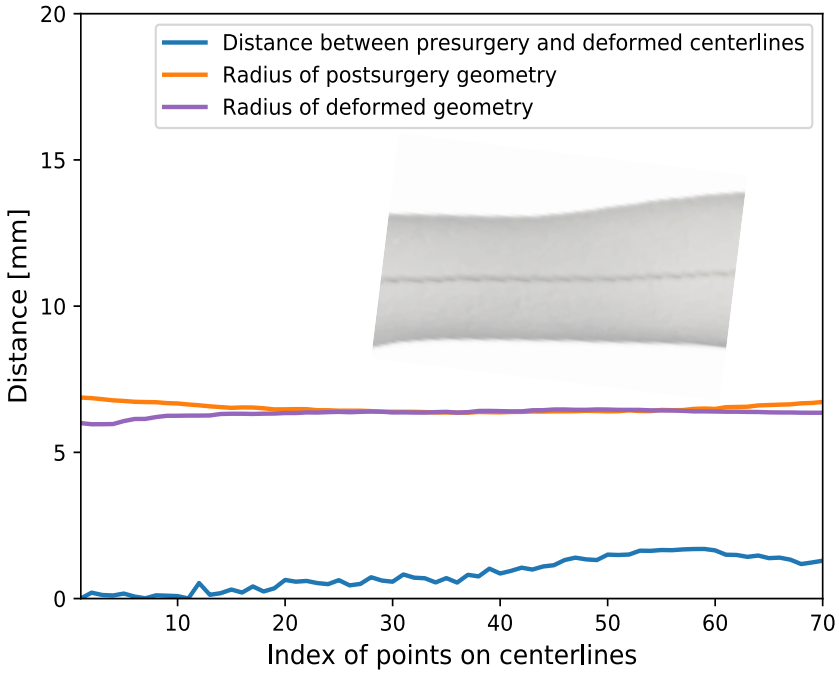

FIGURE 3.20: Validation of virtual stent implantation, with inset showing the realistic post-interventional geometry. An optimal stent with diameter 12 mm was chosen independently in both the in silico modeling and clinical intervention.

be segmented and reconstructed from high-quality image slices [41, 7, 53]. Furthermore, flow MRI is used for visualization and quantification of aortic flow. 2D flow MRI with through-plane velocity encoding is usually performed in clinical applications [119, 129, 138]. But the 2D flow measurement is affected by the selection of the cross-sectional plane. 4D flow MRI, alternatively, is able to obtain time-dependent 3D blood flow, which is resolved in all three dimensions of space and the dimension of time during the cardiac cycle. It can used for the estimation of the flow pathways and the WSS. But 4D flow imaging takes a significant amount of time, which prevents wide clinical application. Thus for patient-specific in silico stent implantation, MRI and LES need to work together and both are indispensable. Particularly, MRI provides data for geometry and boundary conditions, while LES predicts aortic flows for further evaluation.

3.1.6 Limitations and Future Works

In this work, we validated the LBM based LES with both phantom and in vivo experiments, and provided a realistic example of the in silico stent implantation. There are still some improvements possible which could be considered in the future. Firstly, the aortic flow is unsteady, but we didn't consider time dependent boundary condition in our simulations. We argue that current boundary conditions are enough for us to compare different methods and provide results for stent evaluation. By modeling the realistic cardiac cycle, one may get more instantaneous flow information at

the cost of longer computation time. Secondly, we assigned the flow rates to the vessel branches according to their cross areas. An alternative is the Windkessel model which considers resistance and capacitance of the vessel network. Thirdly, we used a fast geometric method to mimic the complex interaction between the aortic wall and the stent. Ideally, one would take into account the mechanical properties of the aortic wall and the stent, as well as the geometry of the stent, and model their interaction using finite element method. Unfortunately it is still a big challenge to get accurate orthotropic properties of the fiber reinforced aortic wall and to model the contact problem numerically. Thus a simplified geometric method is a reasonable start, and should be improved in the future for more realistic virtual stent implantation.

On the other hand, as an important part of the in silico modeling, MRI provides information such as geometry and boundary conditions. Thus the image quality directly affects the flow field obtained. Therefore, MRI acquisition techniques and image post-processing still need to be optimized. Furthermore, although the traditional CFD can resolve the hemodynamics accurately, it is still time consuming. For rapid surgical planning, other methods such as machine learning might be considered in the future.

3.1.7 Conclusion

As a congenital defect, CoA may cause many serious problems for patients if it is not treated in time and effectively. Stent intervention is a recommended therapy, but it remains challenging for physicians to find the optimal stent before treatment. In this study, we proposed a framework for personalized stent planning using in silico modeling, combining CFD and image-based virtual geometry deformation. We firstly compared the flow fields from LBM based LES and DNS, and MRI for 3D-printed phantoms and in vivo. The validated LES was then used to resolve the flows in virtually deformed aortic geometries. Stents with three different diameters were considered. Based on the obtained pressure drop and maximum WSS, we concluded that a stent with diameter 12 mm was the optimal one for the patient. This agrees with the physicians' independent choice. Our study shows that the proposed in silico stenting is a powerful tool, and can be used to help clinicians to evaluate the surgical plans based on predicted results and to be able to select an optimal stent before intervention. Such methodology could also be extended to other stenosis, such as cerebral artery stenosis.

Conflict of interest

The authors have no conflict to disclose.

Ethics Declarations

This article does not describe studies with human or animal subjects. The anonymous images used in this article were obtained from a clinical database. Informed

consent of the patients that permits research use of their data has been obtained beforehand.

3.2 Supplementary Material

Geometry Deformation

- **Transition zone deformation**

  In addition to the stent zone, we need to consider the transition zone, which is the junction between the stent zone and the normal vessel. Because the vessel is elastic, in order to ensure continuity and smooth transition between the stenotic zone and the original vessel at the junction, we assume that the diameter change of the transition zone is associated with the following logistic function. The schematic diagram of virtual surface deformation located at transition zone are shown in Figure 3.21. The diameter D_m can be calculated using

$$D_m = \frac{1}{1 + e^{-12(\frac{n}{m} - 0.5)}}, \tag{3.5}$$

  where $n \in [0, m]$, m is the length of the transition zone. If a large m is chosen, it is a wider and smoother transition zone. So m represents the stiffness of the vessel.

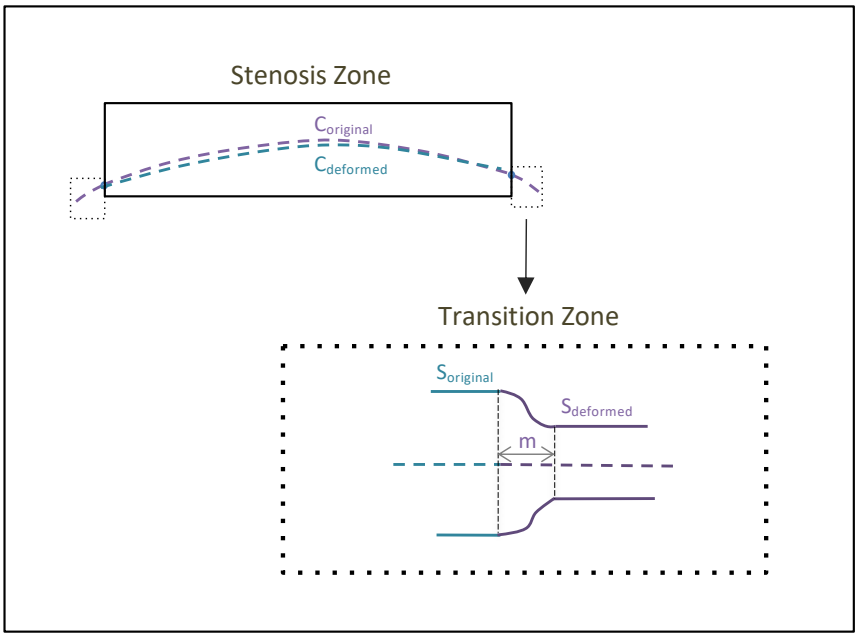

FIGURE 3.21: The schematic diagram of virtual surface deformation located at transition zone.

- **The procedure of Geometry deformation**

TABLE 3.5: The parameters used in the visual aortic deformation.

Parameters	Input
Narrowing region	No. 300-393
Centerline control (Distance)	0.4
Centerline control (i)	0.1
Transition Zone	2
Stent diameter	12

The process of virtual aortic deformation [85] is shown in Figure 3.22. First, we performed the calculation of the original aortic centerline. After image segmentation and reconstruction, we were able to obtain a stl file of the aortic geometry, whose centerline was then calculated using Vmtk. The basic principle is to find the centroid of the largest endotropic sphere at each vertex on the 3D Voronoi diagram of the surface grid, and connecting these centroids draws the centerline. At the same time, the aortic diameters along the aorta were also obatined. As shown in Figure 3.23, the relative stenosis from the ascending segment of the aorta through the aortic arch to the descending segment occurs at points 300-393 on the centerline, with a stenosis length of 33.36 mm and a minimum stenosis diameter of 6.03 mm. The input parameters for virtual deformation are given in Table 3.5, where the centerline control (Distance) represents the maximum distance between spline and straight line (the gray line in Figure 3.12). Finally we got the new aortic centerline and the surface geometry deformed according to the new aortic centerline, which can be seen in Figure 3.2. In addition, based on the mean diameter range and the length of the stenotic segment, an aortic stent (the diameter is 12 mm and the length is 34 mm) was recommended to treat this patient, and this result was proved to be in good agreement with the the one used by the physicians.

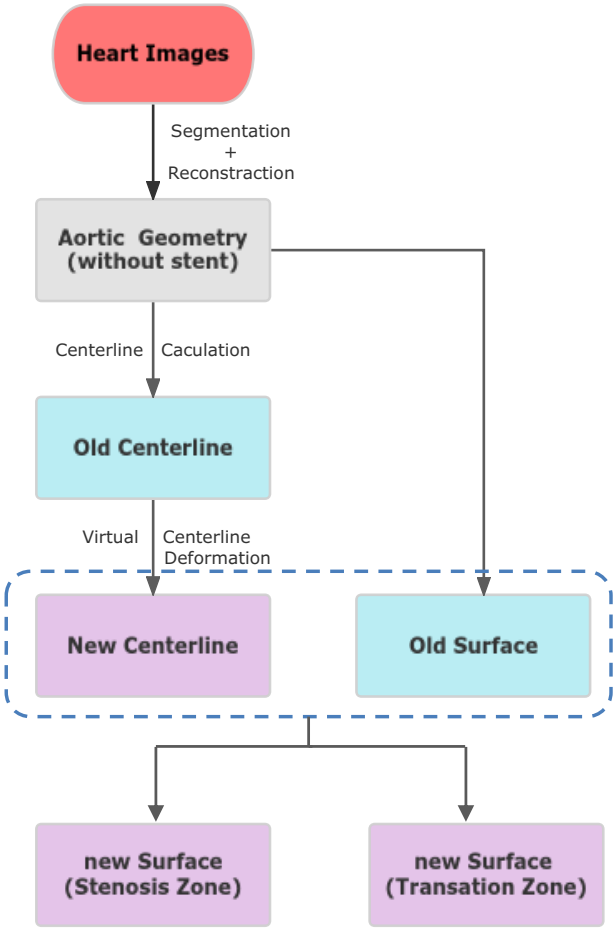

FIGURE 3.22: Flow chart of virtual aortic geometry deformation.

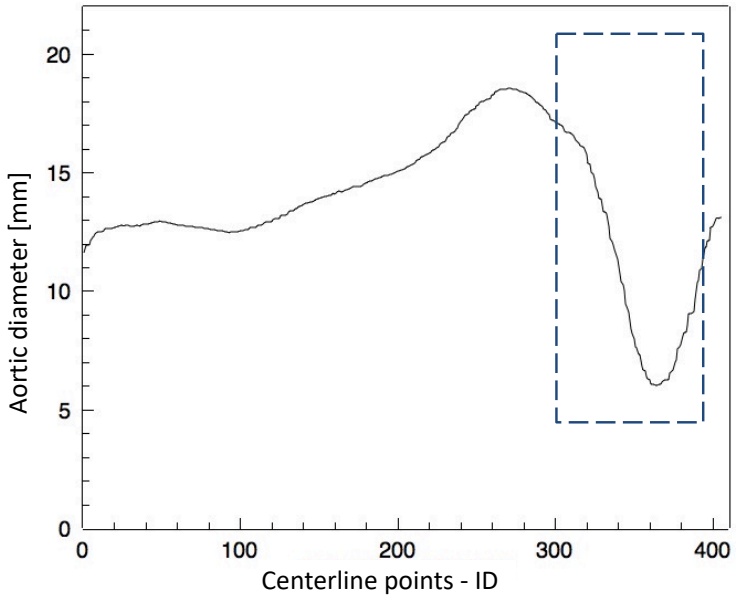

FIGURE 3.23: The distribution of diameter along the centerline in the pre-interventional aorta. The region of aortic stenosis is shown in the black box.

Chapter 4

Image-based hemodynamic prediction using PINN

MRI is indispensable in hemodynamic studies as a harmless and non-invasive experimental tool, but the flow information obtained from flow MRI still have some uncertainties. CFD resolves the flow field by numerically solving the physical equations, but its accuracy is determined by several factors such as the geometry of the computational region, boundary conditions and numerical models.

The emergence of PINN, which is based on the NN framework and physical equations, has attracted much interest. For several canonical laminar flows, PINN performed well based on CFD data or experimental data as training data [102, 27, 58, 83]. Further development of the PINN offers the possibility to predict more complex flow. For example, by involving an artificial viscosity, PINN was used for the recovery of scale-adaptive turbulent structures [142]. Although PINN has evolved considerably in the last few years and is being used in an increasing number of fields, very little research has been done in biophysics, especially in hemodynamics.

In this chapter, I propose an alternative strategy that combines PINN and MRI to quantitatively predict flow. This strategy overcomes the limitations of each method in hemodynamic studies to accomplish more accurate and effective predictions. First, I predict flow in idealized phantoms of normal and stenotic vessels and discuss the accuracy of PINN in terms of image noise reduction and data assimilation, as well as its ability to find vessel walls. Next, I use PINN to complete aortic flow prediction in a CoA patient and discuss its ability to predict complex flow field.

4.1 Methodology

This section provides more details of PINN. The training data preparation based on flow MRI is also introduced.

4.1.1 Physics Informed Neural Network

As mentioned in Chapter 1, blood in large vessels can be considered as a Newtonian fluid. The motion of blood flow is governed by three fundamental conservation

laws, as introduced in Chapter 2, namely, the laws of conservation of mass, conservation of momentum and conservation of energy. Since blood is incompressible and has a constant temperature in the body (without considering heat exchange), the governing equations for blood flow can be further simplified as follows:

$$\bigtriangledown \cdot \boldsymbol{u} = 0 \tag{4.1}$$

$$\rho \frac{D\boldsymbol{u}}{Dt} + \bigtriangledown p - \mu \bigtriangledown^2 \boldsymbol{u} = 0 \tag{4.2}$$

where ρ is the density, which is constant for incompressible blood flow; $\boldsymbol{u}$ is the flow velocity containing three components (u, v, w) corresponding to (x, y, z) in the three-dimensional Cartesian coordinate system; p is the pressure; and μ is the dynamic viscosity. Besides those governing equations, initial conditions and boundary conditions are also required to resolve a specific flow.

The schematic diagram of PC MRI based PINN is given in Figure 4.1. A fully connected NN is considered. The input variables of the NN are the positions in a given domain. The output is the flow velocities and other flow-related variables such as pressure and Re. The constraint part contains data constraint and physical equation constraint. The data constraint is to minimize the deviation of the predicted flow field from velocity information from PC MRI, while the equation constraint is to minimize the residuals of the physical equations calculated based on the automatic difference method in Tensorflow [1]. Under the combined effect of data constraint and physical equation constraint, the NN finally predicts the flow field with high accuracy by adjusting the parameters of the hidden layers. The absolute loss equations are given in Equations (4.3) and (4.4). The total loss based on mean square deviations of data and equations in training is given in Equation (4.5).

$$Loss_{equ1} = \frac{\partial u}{\partial x} + \frac{\partial v}{\partial y} + \frac{\partial w}{\partial z} \tag{4.3}$$

$$\begin{aligned}
Loss_{equ2} &= u\frac{\partial u}{\partial x} + v\frac{\partial u}{\partial y} + w\frac{\partial u}{\partial z} + \frac{\partial p}{\partial x} - (\frac{1}{Re} + \nu_\eta)(\frac{\partial^2 u}{\partial x^2} + \frac{\partial^2 u}{\partial y^2} + \frac{\partial^2 u}{\partial z^2}) \\
Loss_{equ3} &= v\frac{\partial v}{\partial x} + v\frac{\partial v}{\partial y} + w\frac{\partial v}{\partial z} + \frac{\partial p}{\partial y} - (\frac{1}{Re} + \nu_\eta)(\frac{\partial^2 v}{\partial x^2} + \frac{\partial^2 v}{\partial y^2} + \frac{\partial^2 v}{\partial z^2}) \\
Loss_{equ4} &= u\frac{\partial w}{\partial x} + v\frac{\partial w}{\partial y} + w\frac{\partial w}{\partial z} + \frac{\partial p}{\partial z} - (\frac{1}{Re} + \nu_\eta)(\frac{\partial^2 w}{\partial x^2} + \frac{\partial^2 w}{\partial y^2} + \frac{\partial^2 w}{\partial z^2})
\end{aligned} \tag{4.4}$$

$$
\begin{aligned}
Loss_{total} &= a * Loss_{data} + b * Loss_{equ} + c * Loss_{bc} \\
&= a * \frac{1}{N_d} \sum_{i=1}^{N_d} (|u_i^* - u_i|^2 + |v_i^* - v_i|^2 + (|w_i^* - w_i|^2) \\
&+ b * \frac{1}{N_e} \sum_{j=1}^{N_e} (\left|Loss_{equ1}\right|^2) + \left|Loss_{equ2}\right|^2) + \left|Loss_{equ3}\right|^2 + \left|Loss_{equ4}\right|^2) \\
&+ c * \frac{1}{N_{bc}} \sum_{k=1}^{N_{bc}} (|u_k^* - u_k|^2 + |v_k^* - v_k|^2 + (|w_k^* - w_k|^2)
\end{aligned}
\tag{4.5}
$$

.

where $Loss_{equ1} - Loss_{equ4}$ are the losses (or residuals) from the continuity equation and NSE, respectively; a, b, c represent the contributions of the data constraint, physical equation constraint and the boundary data constraint, respectively. $Loss_{data} = Loss_u + Loss_v + Loss_w$, in which $Loss_u$, $Loss_v$, $Loss_w$ are defined as the mean square deviations of the velocity components u, v and w. $Loss_{bc}$ can be seen as data constraint in boundary. $Re = \rho u L/\mu$ is the Reynolds number, with L the characteristic length such as vessel diameter. μ_η is an artificial viscosity introduced to model turbulence [142], and is set to zero for laminar flow. N_e, N_d, N_{bc} are the number of equation constraint, number of data constraint, number of data in boundary respectively; thus $N_d \leq N$ and $N_{bc} \leq N$, with N the total number of discrete points in the region of interest.

In this chapter, I used different NN and compared the computational results of them. The Adam method [60] was selected as the optimizer (details described in Chapter 2). *swish* [103] was selected as the activation function. The losses were used to monitor the convergence during the iteration so that solutions with acceptable accuracy were obtained.

4.1.2 Training Data Preparation

To provide training data for PINN, flows in several printed vessel phantoms, with physiologically reasonable Re, were considered. For simplicity, water was used instead of blood.

In a flow image/field, the flow information is contained at many voxels, each of which is considered as a discrete point in space. In this study, the flow fields were acquired using 4D PC MRI, containing three instantaneous velocity components at a specific time and a specific location. Most of the voxels from PC MRI provide realistic blood flow. Due to measurement limitations, some voxels may deviate from the constraints of the physical equations.

As shown in Figure 4.1, three vessel phantoms, including both idealized ones and realistic one, were considered in this study. All three phantoms were generated with Autodesk Meshmixer [113], then printed out. The idealized phantoms were printed using Ultimaker 2 Extended+, while the realistic aortic phantom was printed using

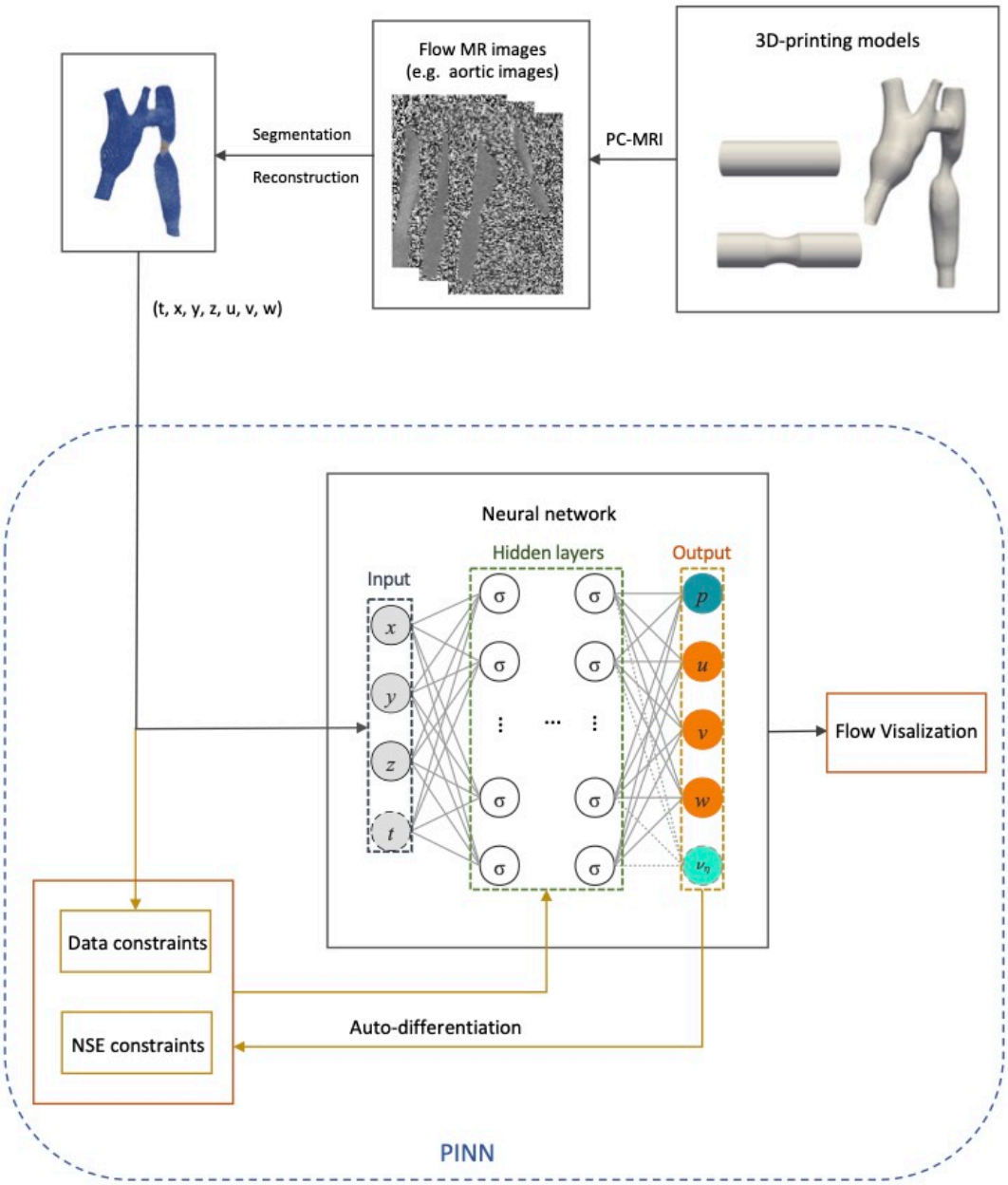

FIGURE 4.1: The schematic diagram of PC MRI based PINN. Top, the training data preparation from PC MRI; bottom, a schematic representation of PINN in blue box.

a high-end 3D laser printer from Stratasys due to more complex geometry, as shown in Section 2.1.3. More details are given below:

- A straight pipe, with inner diameter 30 mm, was used to mimic a normal vessel with laminar flow.
- A pipe with local narrowing was used to mimic a vessel with 50% stenosis. The inner diameters in the normal part and narrowest part are 12 mm and 8.5 mm respectively. Flow therein was laminar.
- An aortic phantom was created based on the three-dimensional anatomy of a patient specific aorta. The model was reconstructed from images obtained by Magnetom Skyra 3T (Siemens Healthineers, Erlangen, Germany). The geometry, including the ascending aorta, aortic arch and descending aorta, was segmented and exported as a STL file using ITK-SNAP [91]. The generated geometry was then smoothed using Autodesk Meshmixer. The flow was turbulent.

Water flows inside these phantoms were driven by a pump, and measured with 4D PC MRI [33, 97]. The parameters of the measurement sequences for the different phantoms will be provided below. Three measurements were performed for each phantom, and the averaged flow field of these three measurements was used as training data for PINN. In addition, LBM-based CFD, with boundary conditions obtained from PC MRI, was also performed for all phantoms and used as a reference for comparison.

4.2 Results and Discussion

In the following I will first present the prediction of laminar flow in the normal vessel. Such flow with analytical solutions is always considered as a benchmark for flow measurement or modeling. I progressively increase the complexity of the geometry, thus complexity of the flow. Secondly, the flow in a stenotic vessel is discussed. Finally, prediction of the flow in a realistic aortic geometry of a CoA patient is performed, and the same geometry was also considered in Chapter 3.

4.2.1 Laminar Flow in Normal Vessel

Flow in the normal vessel phantom was considered first. Such flow was laminar with $Re = 400$, calculated from the maximum velocity and the pipe inner diameter. Parameters used for the flow MRI are given in Table 4.1. In the flow data measured by MRI, some noise is usually present at the boundaries due to e.g. blood and vessel interactions, limitations of image segmentation, etc [69]. In order to select relatively accurate data as training data and check the sensitivity of PINN to the training data, several data sets away from the boundary were considered. The following cases

TABLE 4.1: Parameters used in MRI sequences for the phantom of normal vessel.

	Straight pipe
Sequence type	3D Cartesian FLASH
Matrix size	320 × 263
Number of slices	25
Slice thickness (mm)	2.20
Pixel size (mm^2)	2.10×2.40
Echo time (ms)	2.30
Repetition time (ms)	4.80
Flip angle (°)	10
Velocity encoding (cm/s)	5

were performed with either partial or full data constraint, while physical constraint was applied at all voxels:

- **PINN-50**%: data in the central region with area of 50% of the cross-sectional area of the pipe were selected for training;
- **PINN-70**%: data in the central region with area of 70% of the cross-sectional area of the pipe were selected for training;
- **PINN-100**%: data in the the whole vessel were selected for training;
- **PINNlessS**: 5 out of 30 MRI slices in the long axis of the vessel, thus 1/6 of the whole data, were selected as data constraint.

In the NN part, the inputs are x, y, and z; the outputs are u, v, w and p. Each hidden layer has 50 neurons for each output variable, with a total of 10 hidden layers. For simplicity, this network is named 10*(4*50). The learning rate is 10^{-3} for the first 10,000 iterations, after which it is 10^{-4}. The contribution parameters of losses are $a = 1$, $b = 1$, and $c = 0$. Therein, $c = 0$ means that no strict boundary condition is applied. The predicted flow fields and comparisons are shown in Figures 4.2 and 4.3.

For such pipe flow, if the flow is fully developed, the velocity component in the main flow direction (long axis) is parabolic and the other components are zero due to no-slip boundary condition. The velocity profiles along the y direction located at the center of the pipe, as well as the coordinate system, are shown in Figure 4.2. For such simple flow, CFD data agree with analytical solution very well, thus work as reference here. In general, the flow patterns from MRI, PINN and CFD are similar. For the velocities components u and v, which should be zero, acceptable deviations

are found in the profiles from MRI. Since PINN used the data from MRI as constraint partially, similar but reduced deviations can be found in the profiles of PINN, especially in the region near the wall. For the velocity component w and magnitude $\sqrt{u^2+v^2+w^2}$, MRI introduced some artifacts in the center resulting an asymmetric profile, while the profiles of PINN are closer to that of CFD.

The velocity contours in the $x-y$ and $y-z$ planes are shown in Figures 4.3 and 4.4. In the MRI-obtained flow, the maximum velocity region is off-center and there is some noise at the boundary. But from **PINN-50**% to **PINN-100**%, the velocity contours are getting closer and closer to those of CFD-obtained flow. **PINNlessS** and **PINN-100**% are in general agreement with the CFD-obtained flow. It should be mentioned that CFD used a higher spatial resolution compared with PC MRI and PINN, thus the contours of the CFD-obtained flow are smoother than others. The vessel boundary, i.e., the region with zero velocity, is successfully found in all cases except **PINN-50**%. In addition, PINN successfully predicts the pressure distribution in the main flow direction and the reference pressure at the outlet was defined as zero.

The deviations are shown in Figures 4.5 and 4.6, in which the CFD-obtained flow is used as a reference. It can be seen that the deviations are mainly distributed at the boundary and the off-center regions. As mentioned previously, this is due to the noise introduced by MRI in the area close to the vessel wall. Alternatively, PINN effectively eliminates noise introduced by MRI, especially in the cases of **PINN-70**%, **PINN-100**% and **PINNlessS**. These deviations are summarized in Table 4.2. It is found that for **PINN-50**% and **PINN-100**%, the losses of velocity components are close, while the loss of the equation in **PINN-50**% is the greatest. It should be mentioned that greater loss of data only means greater derivation between the predicted and training data, and does not mean that the prediction is less accurate. And for **PINNlessS**, the loss of data is slightly larger, while its loss of physical equations is minimal, which means that the flow is more consistent with physical laws and therefore more accurate.

The scatter plots of the velocity magnitude distribution are shown in Figure 4.7, using the CFD data as a reference. The blue line represents the state that MRI/PINN and CFD are in perfect agreement. The points with low CFD velocity in the figure represent points close to the no-slip boundary of the vessel. It can be seen that the **PINNlessS** reduced the noises in the region close to the vessel wall, showing a more converged distribution. The root mean square error (RMSE) is reduced from 0.0081288 for MRI to 0.0014937 for **PINNlessS**, while the coefficient of determination (R^2) increased from 0.70726 for MRI to 0.9943 for **PINNlessS**.

Based on the above discussion, we found that **PINNLessS** can achieve flow prediction using a small amount of data. Therefore, in the next study, the data constraints was selected in a similar way as **PINNlessS**.

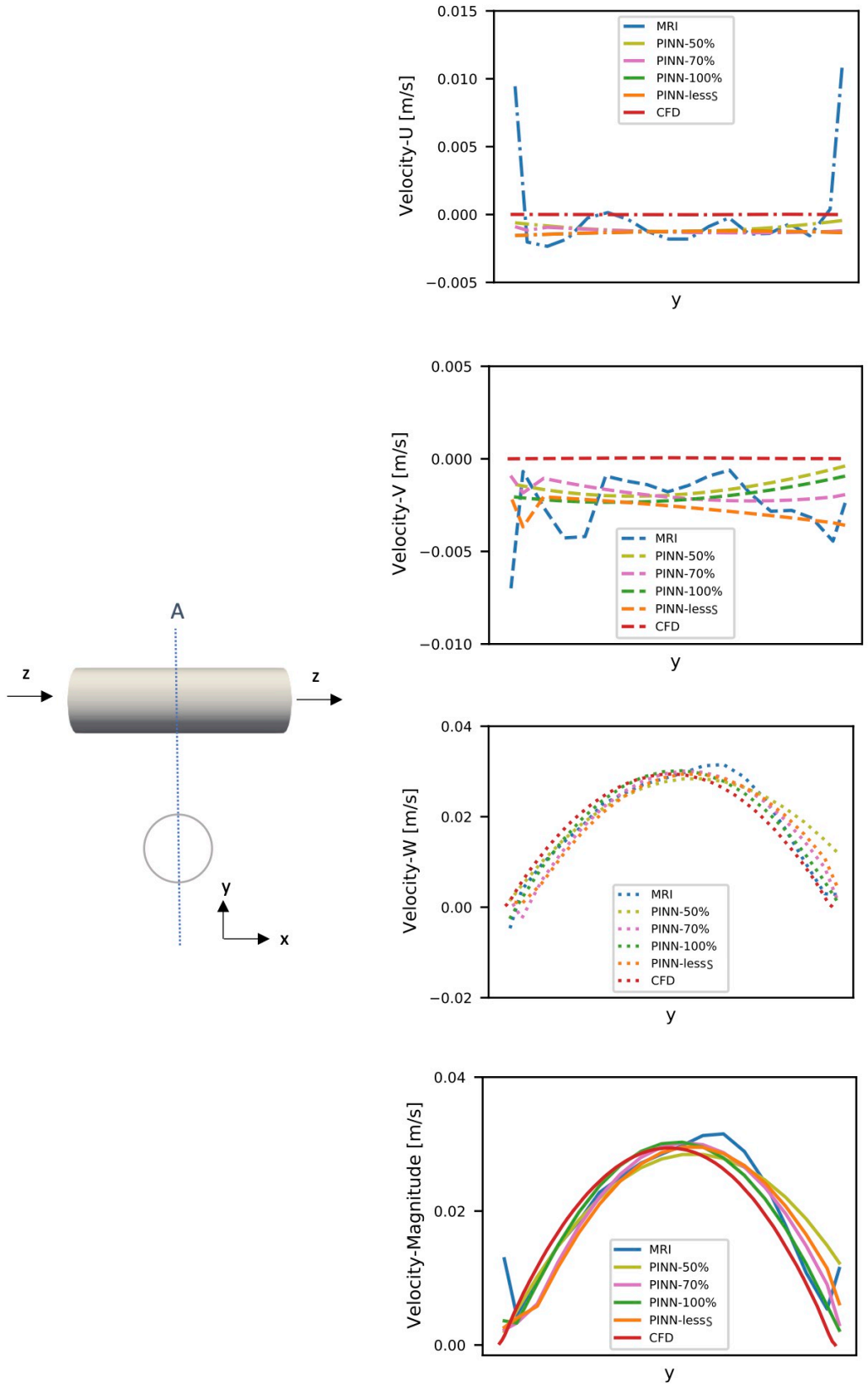

FIGURE 4.2: The velocity profiles in a selected line along y direction. Normal vessel phantom.

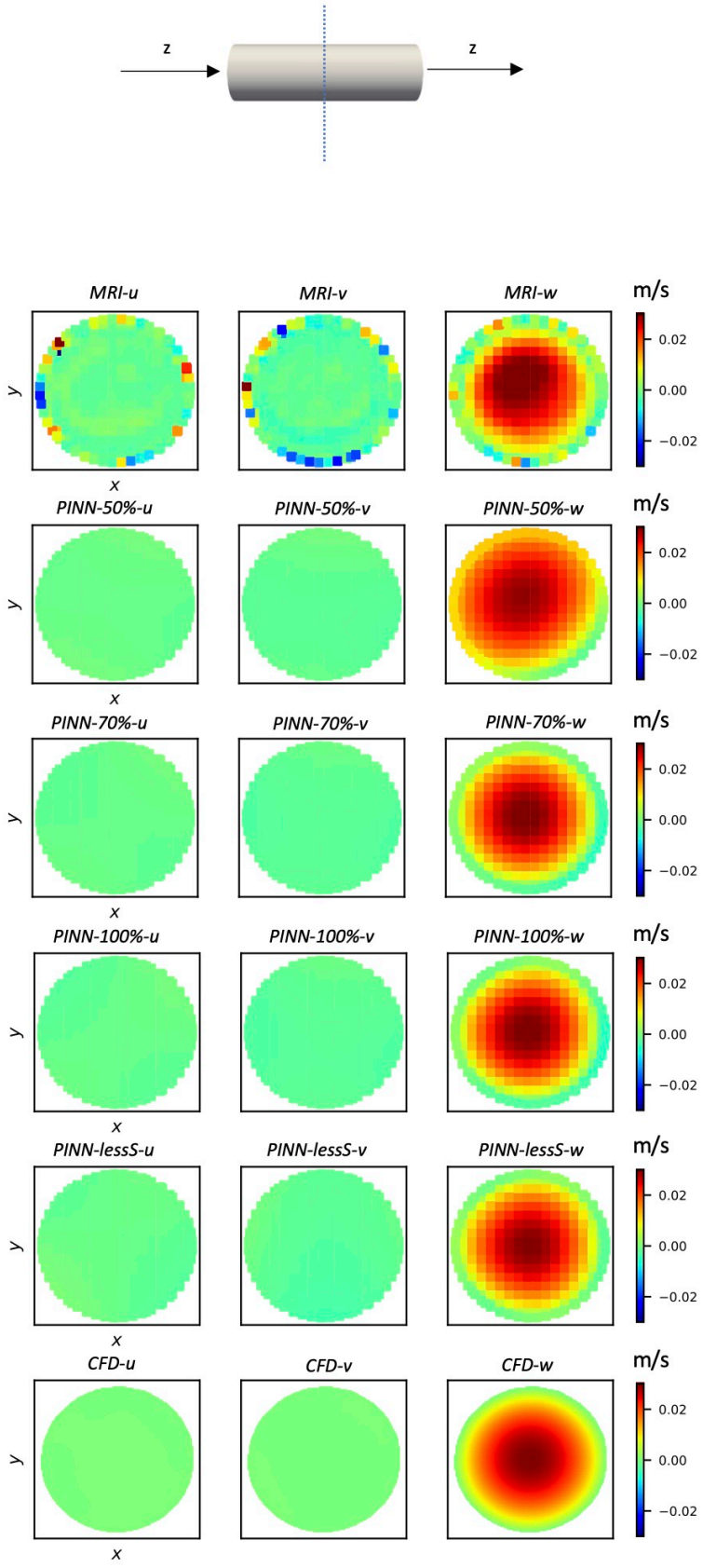

FIGURE 4.3: The velocity contours in the cross-section. From left to right, the three velocity components among the cases from MRI, PINN and CFD. Normal vessel phantom.

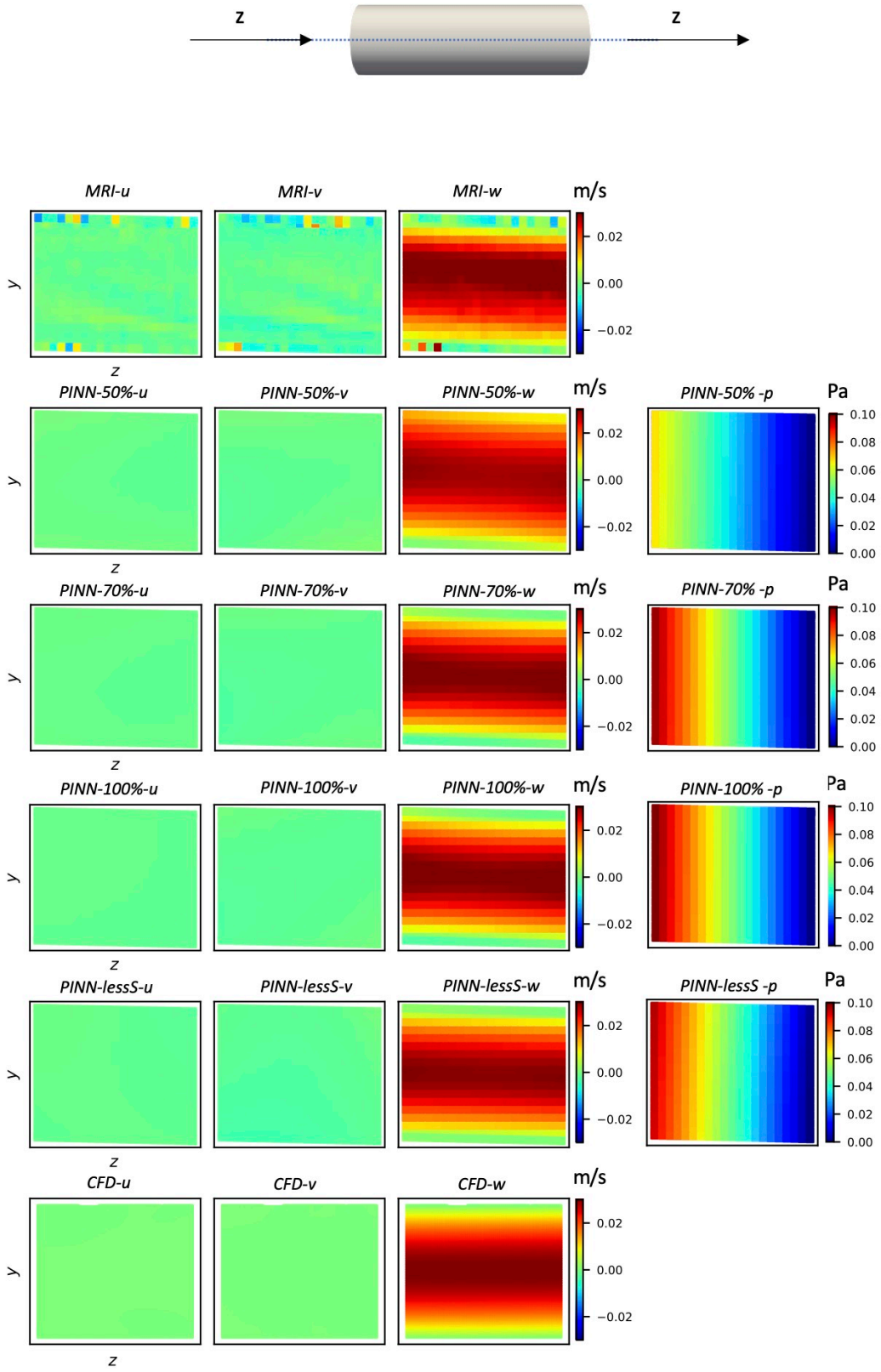

FIGURE 4.4: The velocity and pressure contours in the $y-z$ plane through the central line. From left to right, the three velocity components and the pressure. Normal vessel phantom.

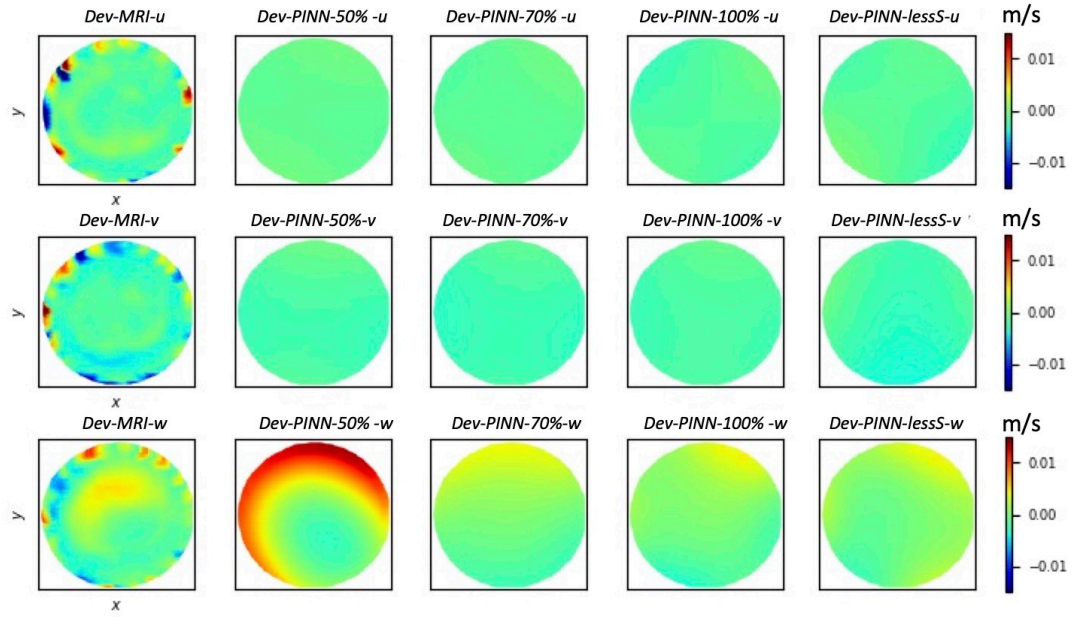

FIGURE 4.5: The deviations of velocity components in the cross-section, using CFD data as a reference. Normal vessel phantom.

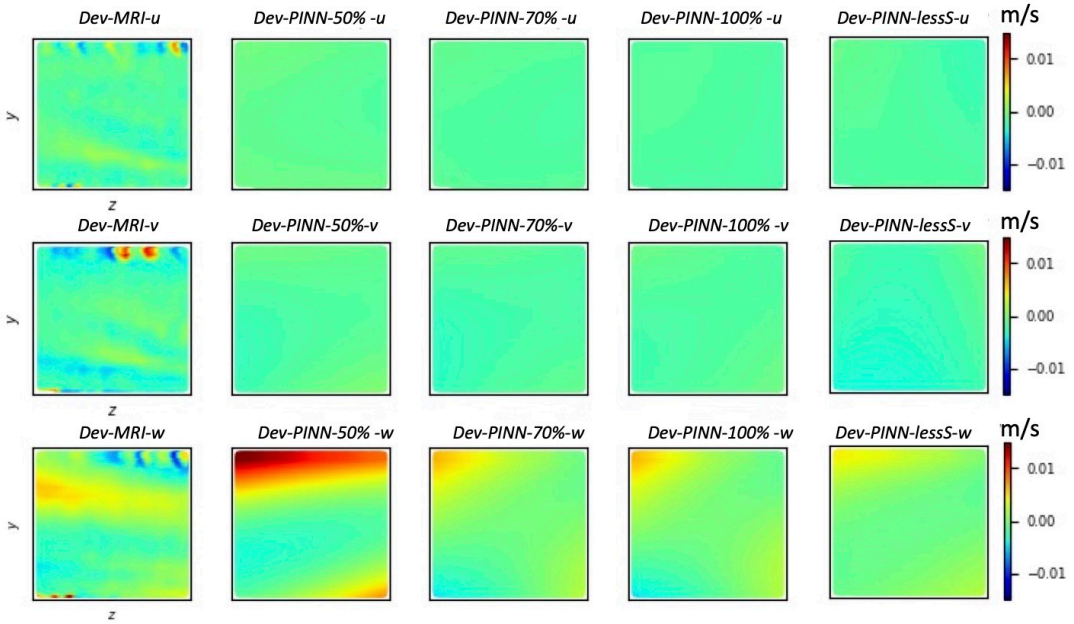

FIGURE 4.6: The deviations of velocity components in the $y - z$ plane through the central line, using CFD data as a reference. Normal vessel phantom.

TABLE 4.2: The comparison of the losses and relative L^2 errors obtained with different training data sets.

	PINN-50 %	**PINN-70 %**	**PINN-100 %**	**PINNlessS**
$Loss_{total}$	9.320×10^{-6}	6.586×10^{-6}	8.234×10^{-6}	7.284×10^{-5}
$Loss_u$	7.624×10^{-7}	8.696×10^{-7}	1.116×10^{-6}	2.004×10^{-5}
$Loss_v$	1.153×10^{-6}	1.432×10^{-6}	1.761×10^{-6}	3.057×10^{-5}
$Loss_w$	4.980×10^{-6}	3.785×10^{-6}	4.120×10^{-6}	2.174×10^{-5}
$Loss_{data}$	6.895×10^{-6}	6.087×10^{-6}	6.996×10^{-6}	7.235×10^{-5}
$Loss_{equ}$	2.424×10^{-6}	1.062×10^{-6}	1.238×10^{-6}	4.956×10^{-7}
Relative L^2 error of u	1.005	1.004	1.004	1.007
Relative L^2 error of v	1.011	1.007	1.007	9.955×10^{-1}
Relative L^2 error of w	6.884×10^{-1}	4.340×10^{-1}	4.296×10^{-1}	4.199×10^{-1}

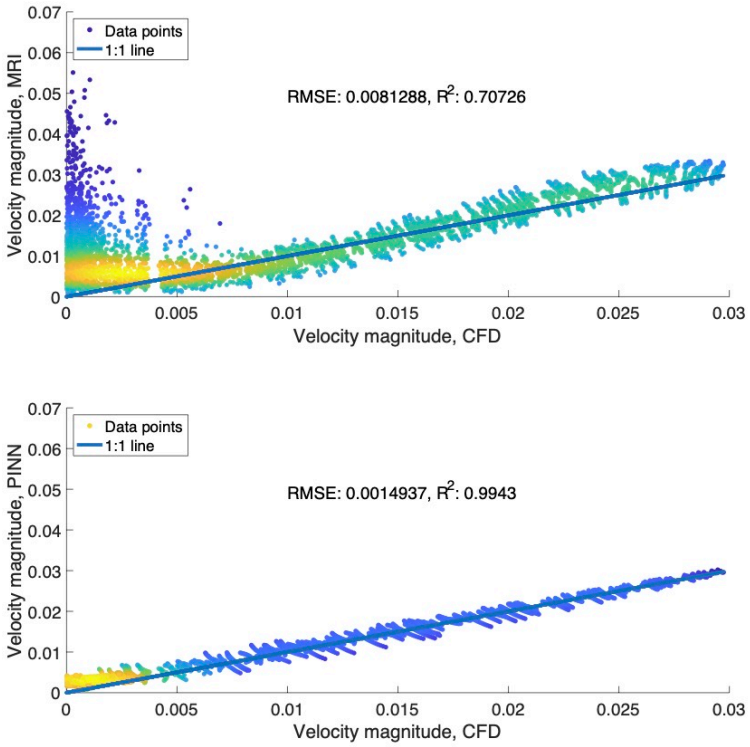

FIGURE 4.7: Scatter plot of the velocity magnitude distribution in the normal vessel phantom (Unit: m/s). Points on the blue line indicate a better fit for PINN/MRI and CFD. Top, comparison of MRI data and CFD data; bottom, comparison of **PINNlessS** data and CFD data. RMSE is the root mean square error and R^2 is the coefficient of determination.

TABLE 4.3: Parameters used in MRI sequences for the stenotic vessel phantom.

	Pipe with stenosis
Sequence type	3D Cartesian FLASH
Matrix size	384×312
Number of slices	78
Slice thickness (mm)	0.77
Pixel size (mm^2)	0.76×0.76
Echo time (ms)	4.6
Repetition time (ms)	36.40
Flip angle (°)	7
Velocity encoding (cm/s)	40

4.2.2 Laminar Flow in Stenotic Vessel

The flow in a vessel with 50% stenosis was considered secondly. This flow was laminar with $Re = 686$, based on the maximum velocity and diameter at the stenosis. Parameters used for flow MRI are shown in Table 4.3. The CFD-obtained flow showed that such flow was steady in the left part and unsteady in the right part after the flow passed the stenosis. Thus only the domain from the normal vessel to the narrowest part was considered for training and comparison. In the long axis of the stenotic vessel, 6 out of 18 MRI slices (approximate 1/3 of the whole data) were selected as data constraint. Two predictions of flow by PINN were performed: one was preformed with the contribution parameters $a = 50$, $b = 1$, and $c = 0.$; the other with an additional no-slip boundary condition, i.e. velocity components at the voxels at the wall were manually set to be zero, with $a = 50$, $b = 1$, and $c = 50$. All the voxels were constrained by the physical equations. Four different network structures were considered firstly, and compared in Table 4.4. It can be found that the network 10*(4*50) has relatively smaller losses and relative L^2 errors, and was used for the following training.

The time histories of the losses can be found in Figures 4.8 and 4.9, where the velocity components converge smoothly, while the error (residual) of equation changes from large oscillations (with learning rate 10^{-3}) to small fluctuations (with learning rate 10^{-4}) during the training of the PINN. It should be noted that a was set to 50 in order to emphasize the data constraint, thus the total loss was scaled up accordingly.

The distributions of velocity located in the plane "A" with normal diameter and the plane "B" with the smallest diameter are shown in Figures 4.10 and 4.11, respectively. It can be found that the velocity profiles of MRI, PINN and CFD are similar. Specifically, in plane "A", the velocity components and amplitudes are very consistent, although there is some noise in the MRI data. In plane "B", the boundary and

TABLE 4.4: The comparison of the losses and relative L^2 errors obtained by different PINN.

	10*(4*30)	10*(4*50)	15*(4*50)	20*(4*50)
$Loss_{total}$	1.387×10^{-2}	1.241×10^{-2}	1.387×10^{-2}	1.328×10^{-2}
$Loss_u$	1.161×10^{-4}	9.842×10^{-5}	1.077×10^{-4}	1.098×10^{-4}
$Loss_v$	7.720×10^{-5}	8.176×10^{-5}	8.795×10^{-5}	8.623×10^{-5}
$Loss_w$	8.231×10^{-5}	6.693×10^{-5}	8.045×10^{-5}	6.768×10^{-5}
$Loss_{equ}$	8.573×10^{-5}	5.226×10^{-5}	6.596×10^{-5}	1.011×10^{-4}
Relative L^2 error of u	4.092×10^{-1}	4.051×10^{-1}	4.070×10^{-1}	4.143×10^{-1}
Relative L^2 error of v	9.591×10^{-1}	9.611×10^{-1}	9.604×10^{-1}	1.002
Relative L^2 error of w	9.988×10^{-1}	0.995×10^{-1}	9.933×10^{-1}	9.887×10^{-1}

maximum velocity values have some slightly larger deviations. In the main flow direction (long axis), it can be seen from Figure 4.12 that u increases significantly from the normal region of the vessel towards the stenosis region. Compared with the MRI-obtained flow, the PINN-obtained flow is more continuous and smoother, close to the CFD-obtained one. In particular, the flow obtained by PINN with boundary conditions is closer to the CFD-obtained flow due to the inclusion of boundary condition. The velocity contours in two cross sections are shown in Figures 4.13 and 4.14. In the normal region, the vessel wall with zero velocity was found in both PINN with and without boundary condition. However, in the narrow region, the variation of velocity in the radius direction is more significant and no boundary was found in the PINN without boundary condition.

The scatter plots of the velocity magnitude distribution are shown in Figure 4.15, using the CFD data as a reference. In the region with low CFD velocity, the PINN data show a more consistent distribution compared to the MRI data. This represents an effective improvement of the flow near the vessel wall by PINN, especially in the case of PINN with boundary conditions. In the region with high CFD velocity, the points from MRI are distributed on both sides of the blue line with bias, while some points from PINN are distributed on the right side of the blue line, i.e., slightly lower than the CFD data. From MRI to PINN, the RMSE decreases and R^2 increases.

4.2.3 Transitional Flow in Aorta with CoA

The combination of PINN and MRI effectively accomplishes the flow prediction of the simplified phantoms described above. Here, I will discuss the ability of PINN to predict more complex flow in realistic aorta. The third phantom is the geometry of a three-dimensional aorta from a patient with CoA. As presented in Chapter 3, the bifurcation vessels were blocked in order to simplify the experimental setup. In this

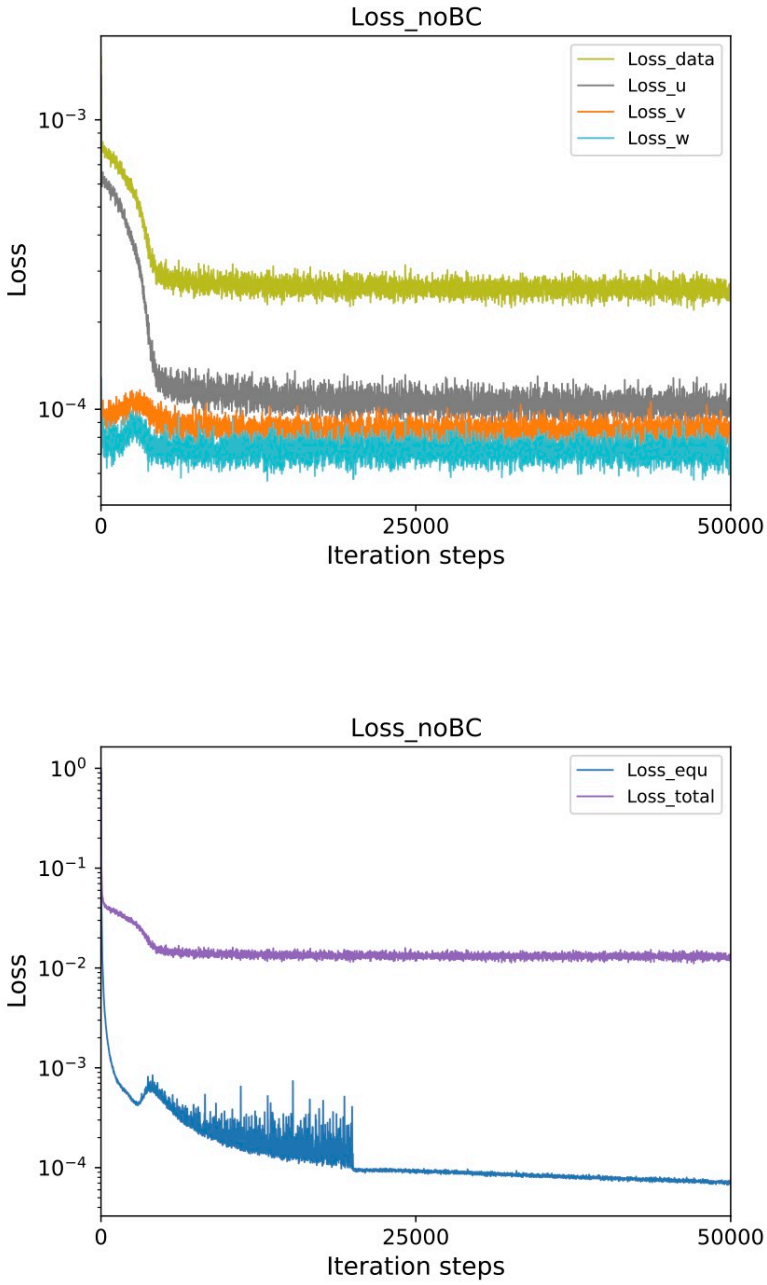

FIGURE 4.8: The losses monitored during the training process in the case of stenotic vessel without boundary conditions. The learning rate is 10^{-3} until 20,000 iterations, after which it becomes 10^{-4}. Top, $Loss_u$, $Loss_v$, $Loss_w$ and $Loss_{data}$; bottom, $Loss_{equ}$ and $Loss_{total}$. Contribution parameters $a = 50$, $b = 1$, and $c = 0$.

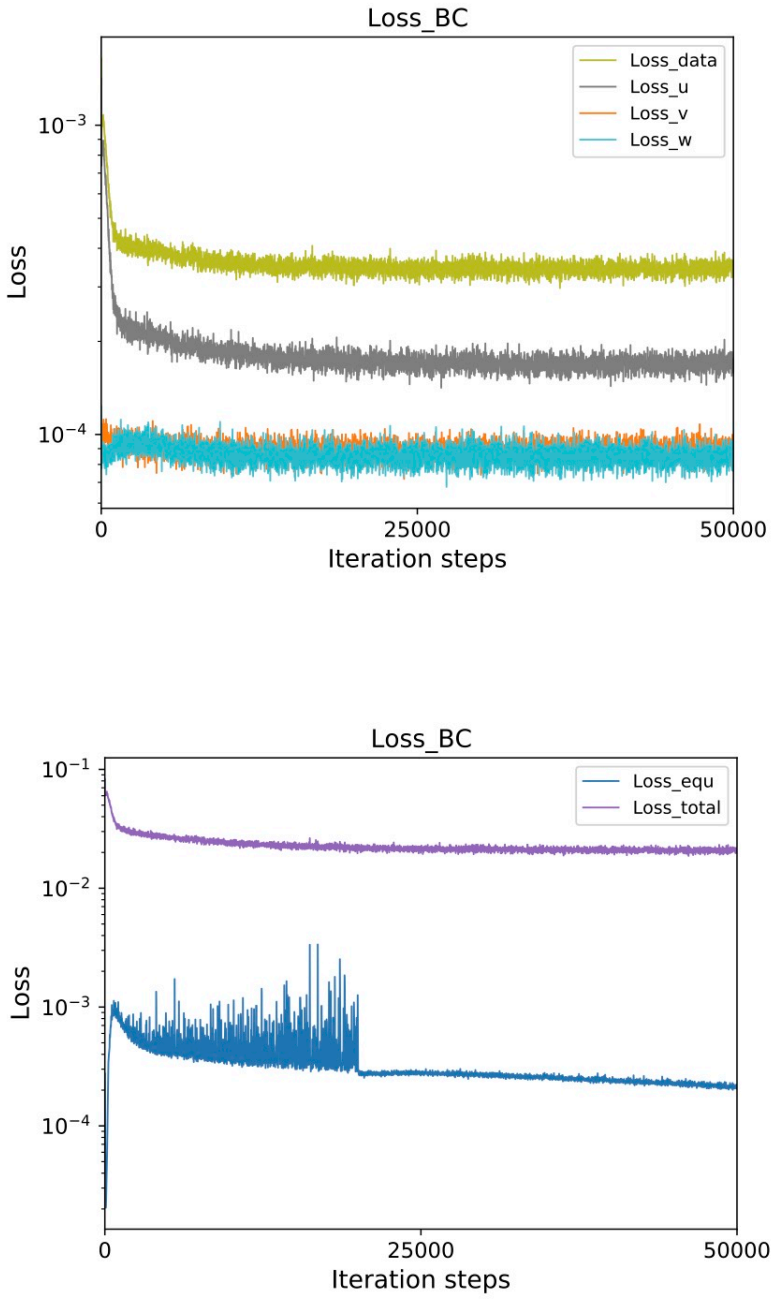

FIGURE 4.9: The losses monitored during the training process in the case of stenotic vessel with boundary conditions. The learning rate is 10^{-3} until 20,000 iterations, after which it becomes 10^{-4}. Top, $Loss_u$, $Loss_v$, $Loss_w$ and $Loss_{data}$; bottom, $Loss_{equ}$ and $Loss_{total}$. Contribution parameters $a = 50$, $b = 1$, and $c = 50$.

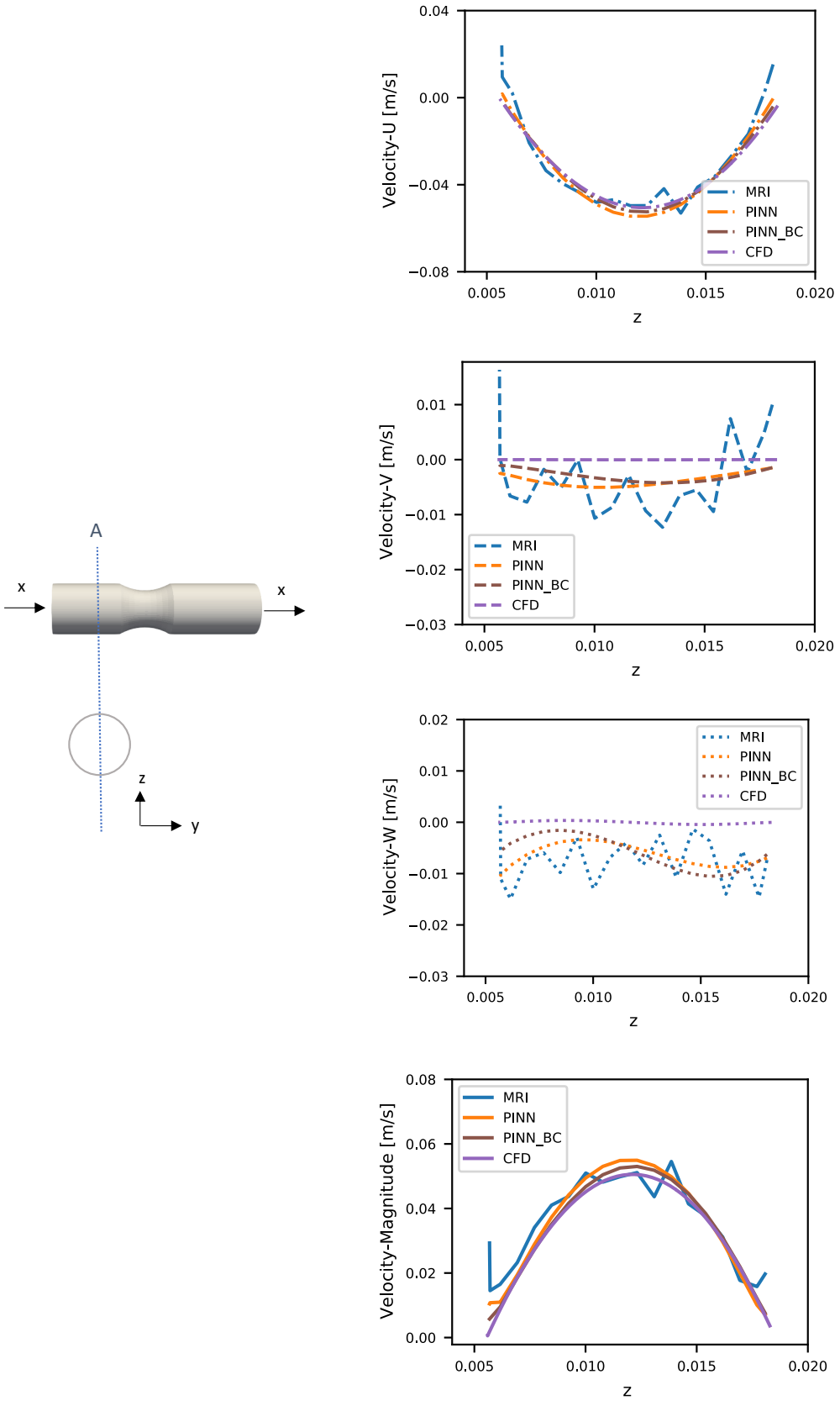

FIGURE 4.10: The comparison of velocity profiles in the normal region of the stenotic vessel. Left: location of plane "A"; right: velocity components along the symmetric axis of plane "A".

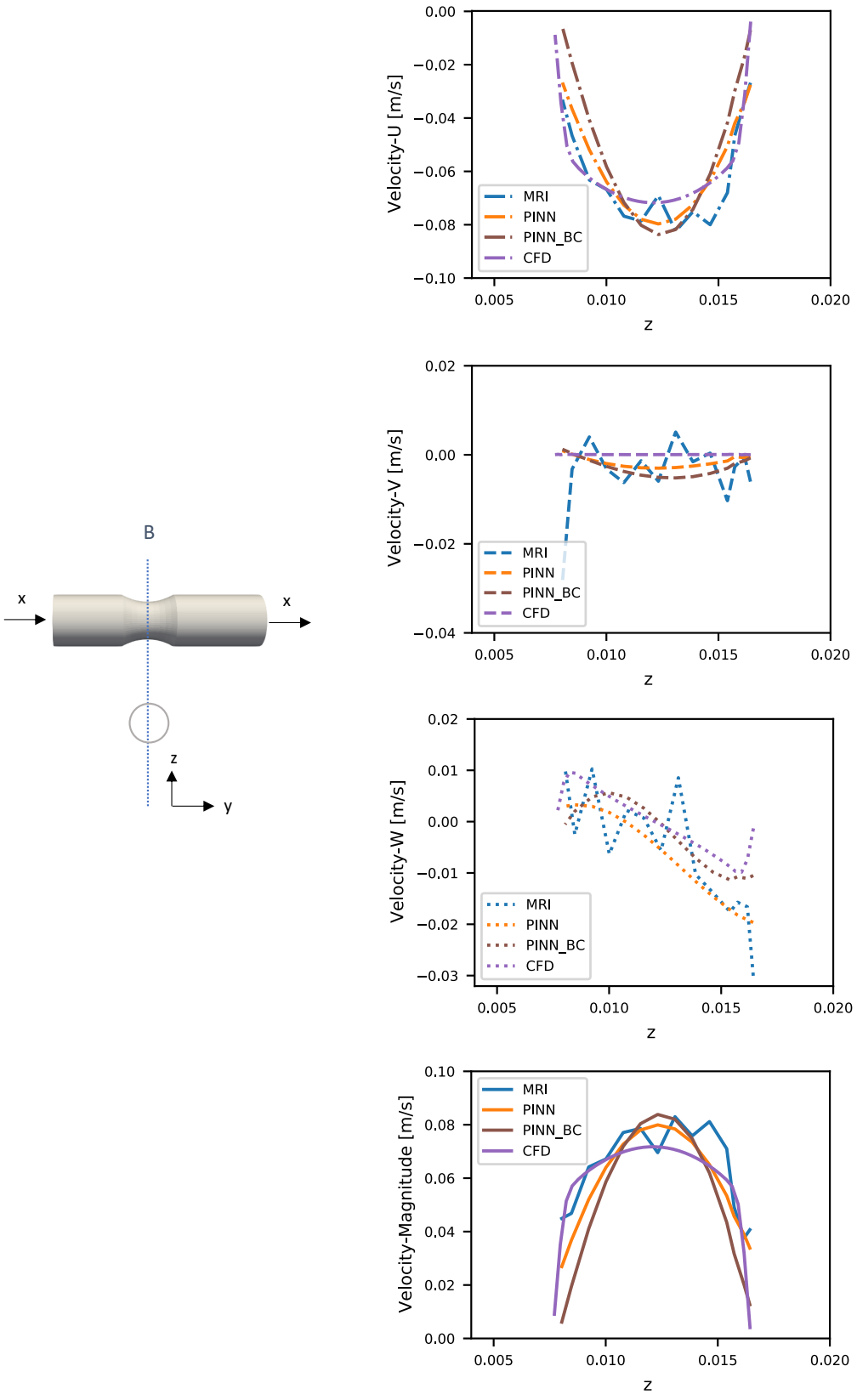

FIGURE 4.11: The comparison of velocity profiles in the narrowest region of the stenotic vessel. Left: location of plane "B"; right: velocity components along the symmetric axis of plane “B”.

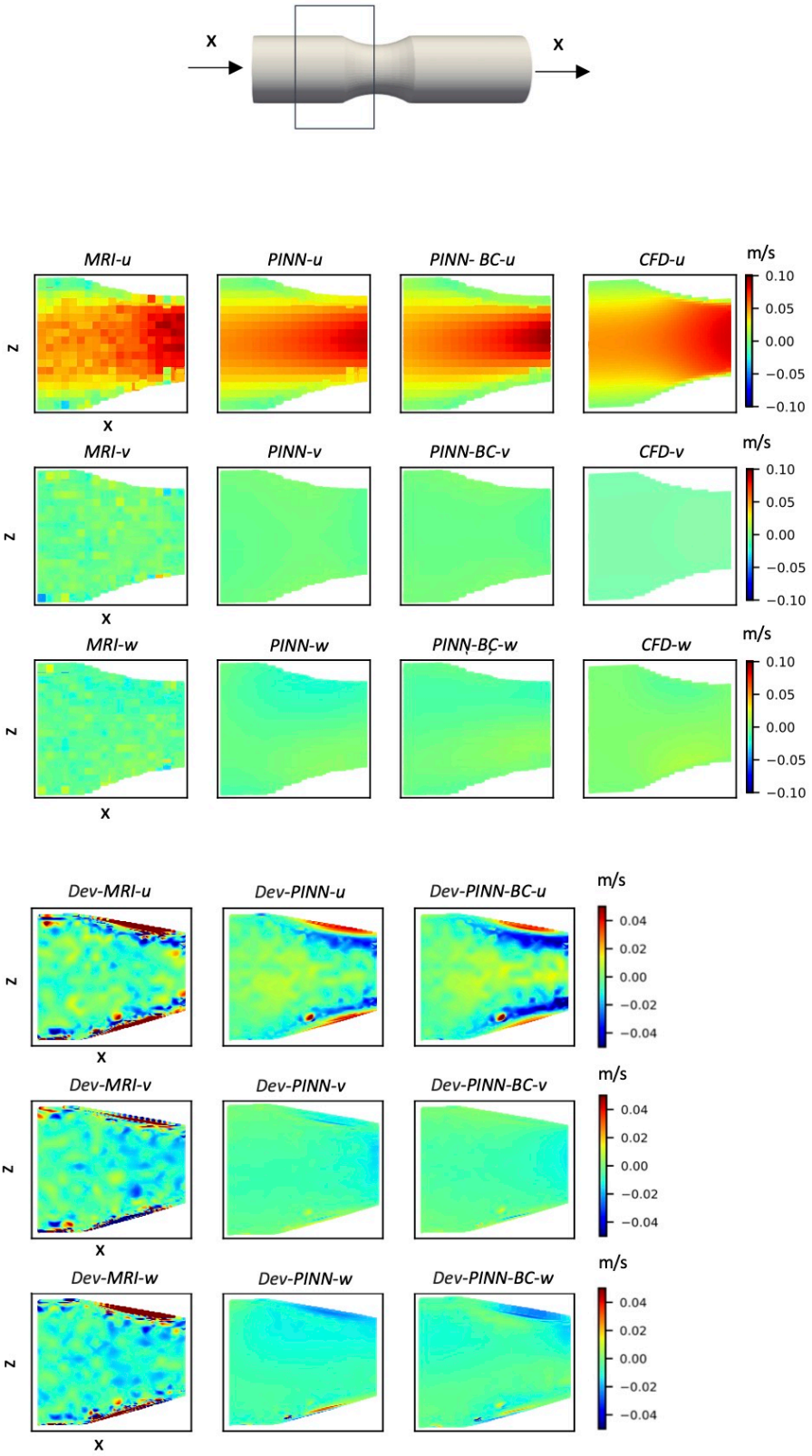

FIGURE 4.12: Velocity contours in the central $x-z$ plane of the stenotic vessel. Top, location of the central $x-z$ plane; middle, distributions of the velocity components; bottom, distributions of the differences between the MRI/PINN data and the CFD data. All images were interpolated to a resolution of 0.01 mm to calculate the differences.

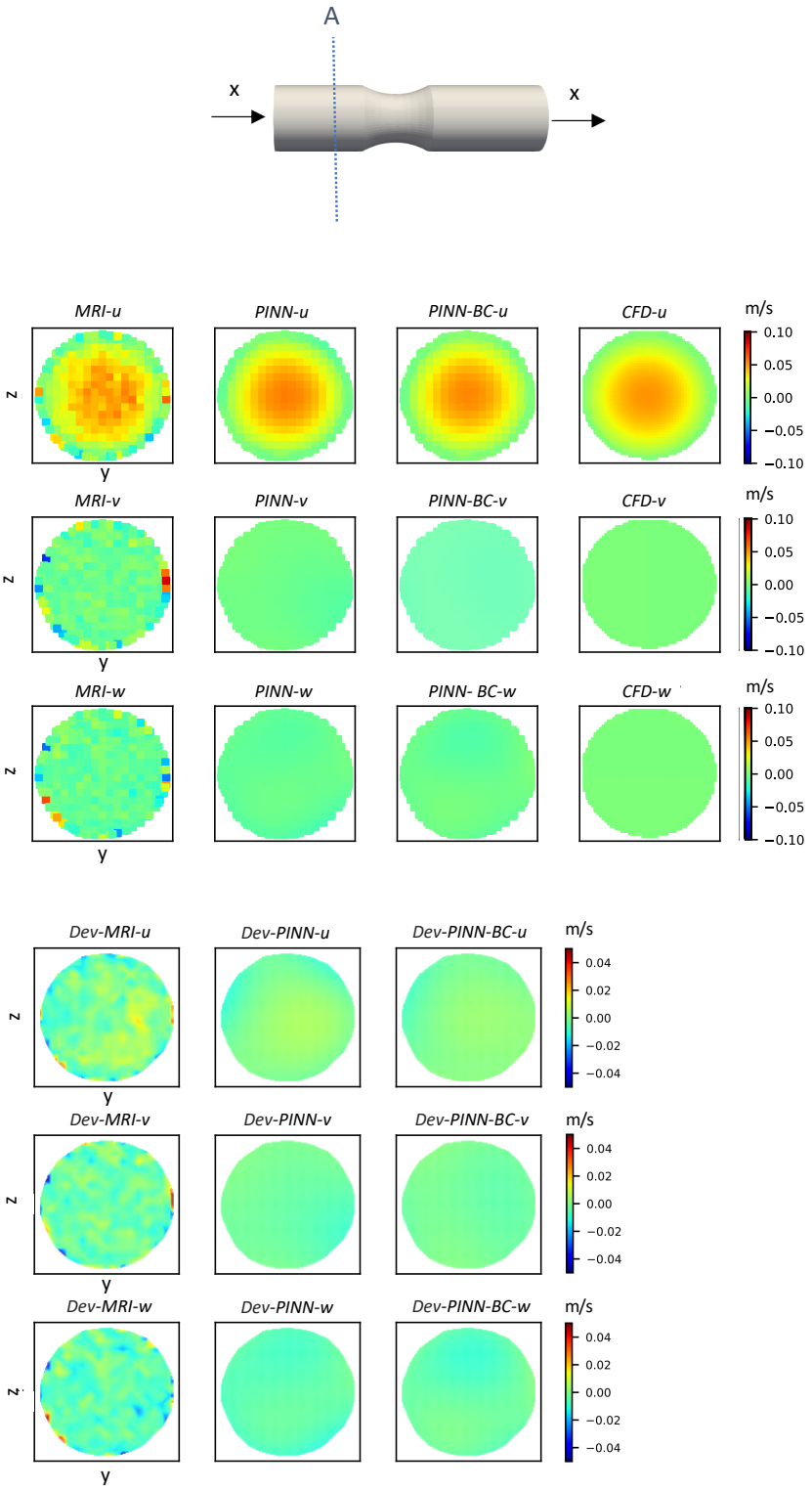

FIGURE 4.13: Velocity contours in a cross section of the normal region of the stenotic vessel. Top, location of the cross plane "A"; middle, distributions of the velocity components; bottom, distributions of the differences between the MRI/PINN data and the CFD data. All images were interpolated to a resolution of 0.01 mm to calculate the differences.

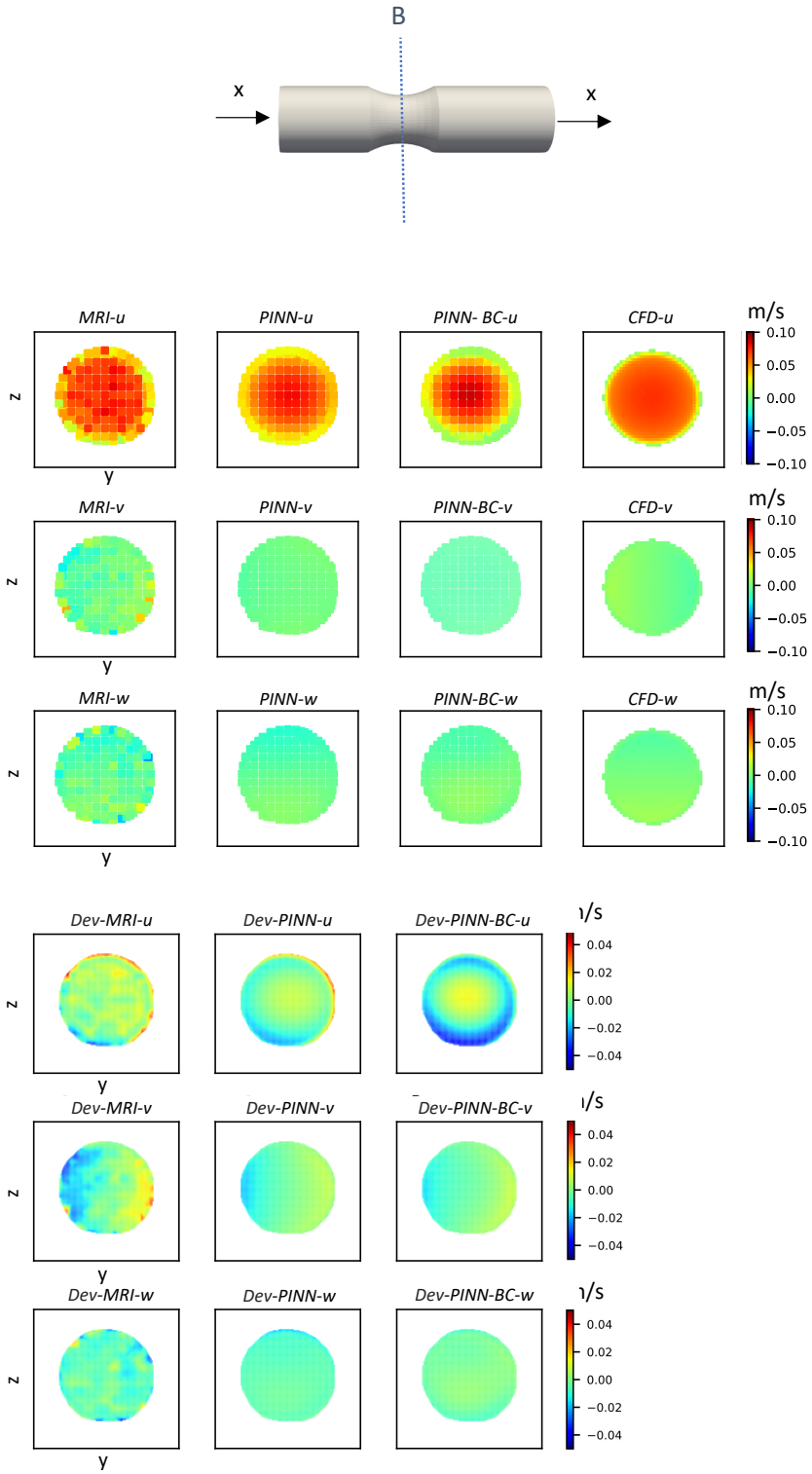

FIGURE 4.14: Velocity contours in the cross section of the narrowest region of the stenotic vessel. Top, location of the cross plane "B"; middle, distributions of the velocity components; bottom, distributions of the differences between the MRI/PINN data and the CFD data. All images were interpolated to a resolution of 0.01 mm to calculate the differences.

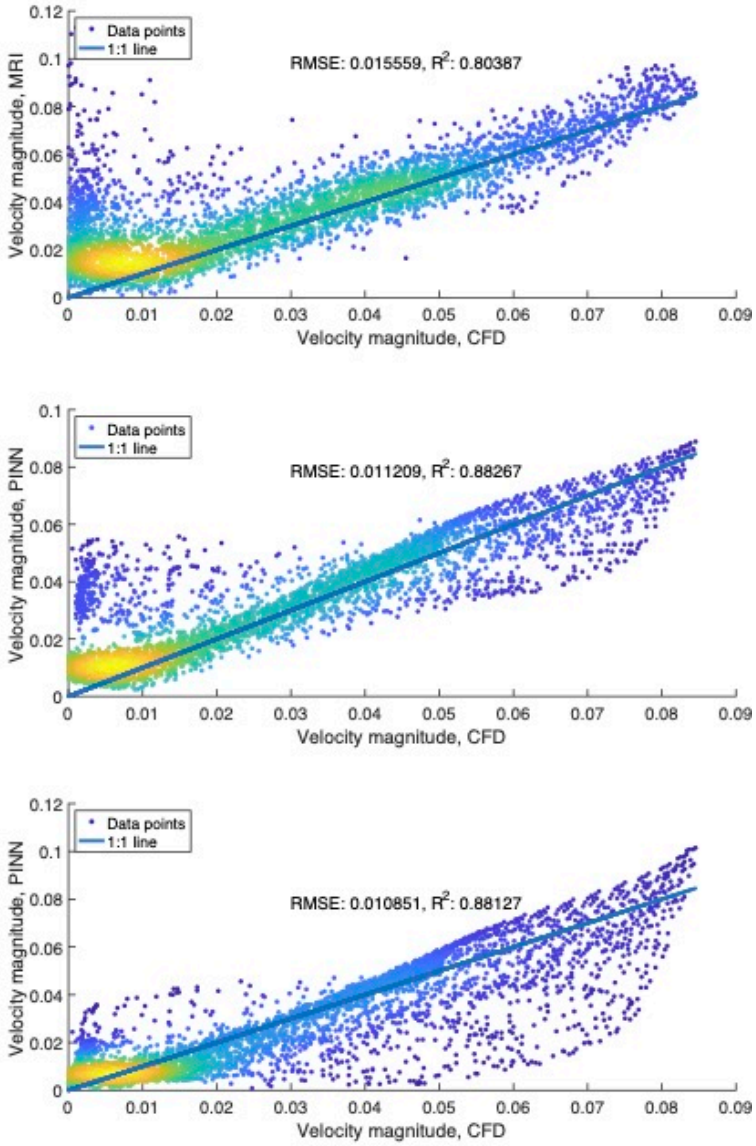

FIGURE 4.15: Scatter plot of the velocity magnitude distribution in the stenotic vessel phantom (Unit: m/s). Points on the blue line indicate a better fit for PINN/MRI and CFD. Top, comparison of MRI data and CFD data; middle and bottom, comparison of PINN data (without/with boundary conditions) and CFD data. RMSE is the root mean square error and R^2 is the coefficient of determination.

TABLE 4.5: Parameters used in the MRI sequences for aortic phantom measurements.

	aortic phantom
Sequence type	3D Cartesian FLASH
Matrix size	384 ×504
Number of slices	144
Slice thickness (mm)	0.77
Pixel size (mm^2)	0.77×0.77
Echo time (ms)	4.61
Repetition time (ms)	36.40
Flip angle (°)	7
Velocity encoding (cm/s)	50

phantom, when the water flows through the bifurcation and stenosis of the aorta, it causes a complex flow due to the complex geometry.

First, I selected 6 slices of PC MRI data along the main stream of the aorta as data constraint to predict the flow through the whole stenotic region. The thickness between the selected slices is 5.39 mm, which is 7 times the thickness of the original MRI slices. The Re is about 5000, based on the maximum velocity and equivalent diameter of the narrowest part of the aorta. Since some region of the flow was turbulent, an additional output value ν_η was considered in the PINN. Such artificial viscosity term was used to regress the Reynolds stress in the RANS model. $a = 50$, $b = 1$ and $c = 0$ were used for the loss contributions in the training. This case is named **CoA-1**. The network was 10*(5*80) and the convergence of the losses can be found in Figure 4.16. The velocity component converges smoothly. $Loss_{equ}$ and $Loss_{data}$ change from large oscillations (learning rate of 10^{-3}) to small fluctuations (learning rate of 10^{-4}).

Since the flow in the aortic stenotic segment was turbulent, the temporally averaged flow field was used for training. Specifically, the MRI-obtained flow and the CFD-obtained flow were averaged over multiple time instants, while the equation constraints for PINN were parameterized equations with the artificial viscosity. The velocity contours in a $y - z$ plane (Figure 4.17) and a $x - z$ plane (Figure 4.18) show a sharp increase in velocity as the blood flow passes through the stenosis, producing a jet after the stenosis that leads to an abrupt change in pressure. The MRI-obtained and PINN-obtained flows clearly show the complex profile. In the PINN-obtained flow, the noise is reduced and the flow is smoother. Comparing the velocity magnitude, it can be seen that both PINN and MRI are generally close to the CFD-obtained flow. In addition, in the pressure distribution of PINN, a sharp drop in pressure can be clearly observed as the blood flow passes through the stenotic segment. This shows that PINN has the ability to accomplish flow prediction even in realistic stenotic aortas using a small number of data constraint.

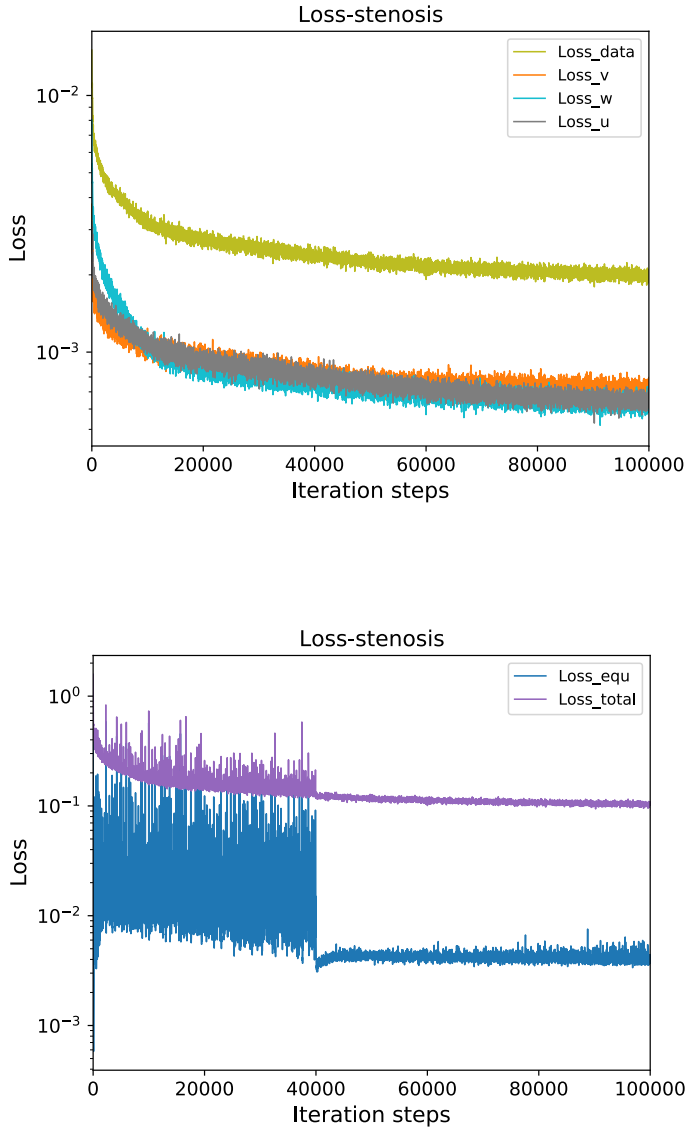

FIGURE 4.16: The losses monitored during the training process in **CoA-1**. The learning rate is 10^{-3} until 40,000 iterations, after which it becomes 10^{-4}. Top, $Loss_u$, $Loss_v$, $Loss_w$ and $Loss_{data}$ are shown; bottom, $Loss_{equ}$ and $Loss_{total}$ are shown. Contribution parameters $a = 50$, $b = 1$, and $c = 0$.

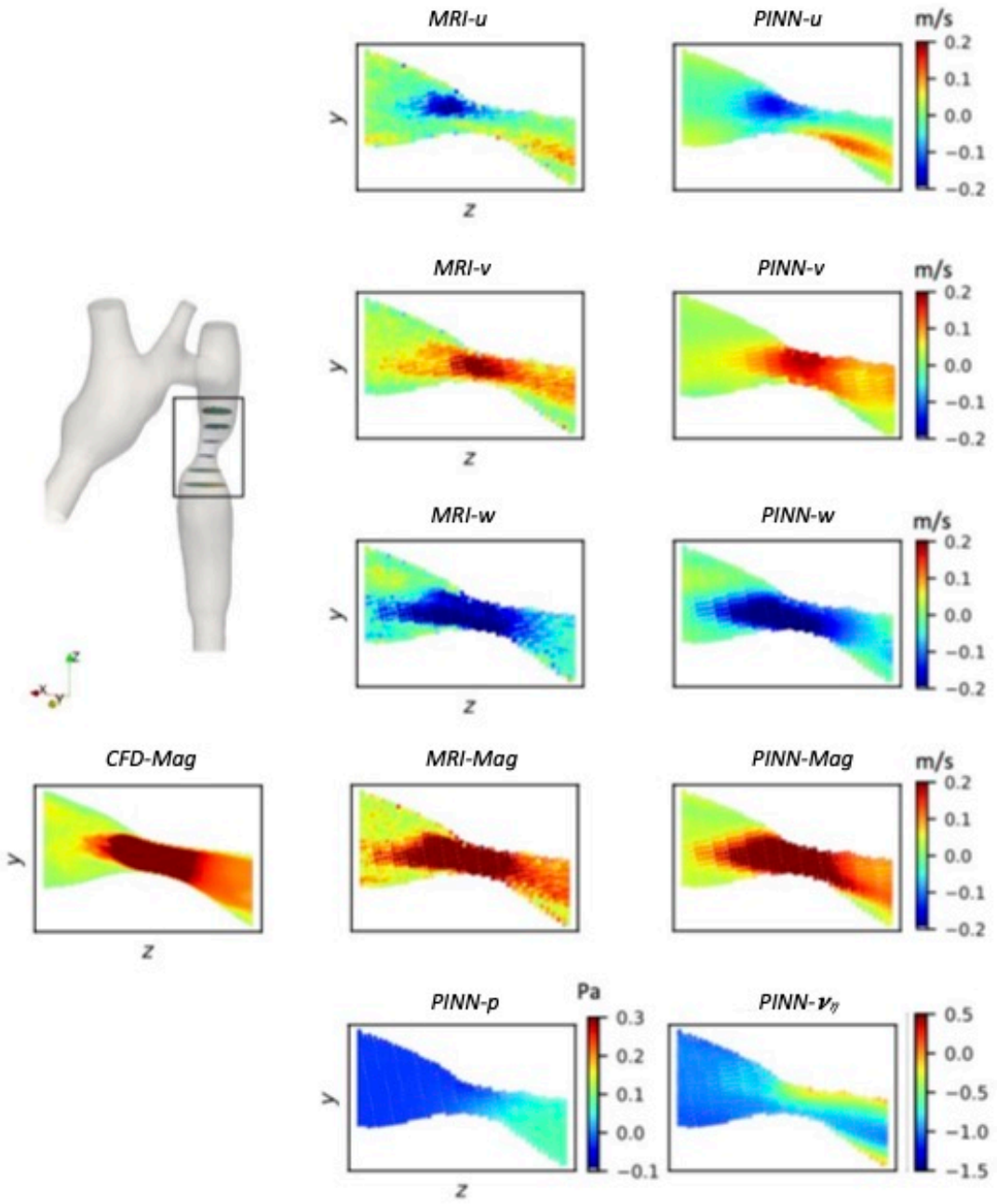

FIGURE 4.17: The velocity and pressure contours of **CoA-1** in a $y-z$ plane. Left, the training data (6 slices) and the velocity magnitude from CFD; middle, the velocity components, magnitude from MRI and the pressure from PINN; right, the velocity components, magnitude and artificial viscosity from PINN.

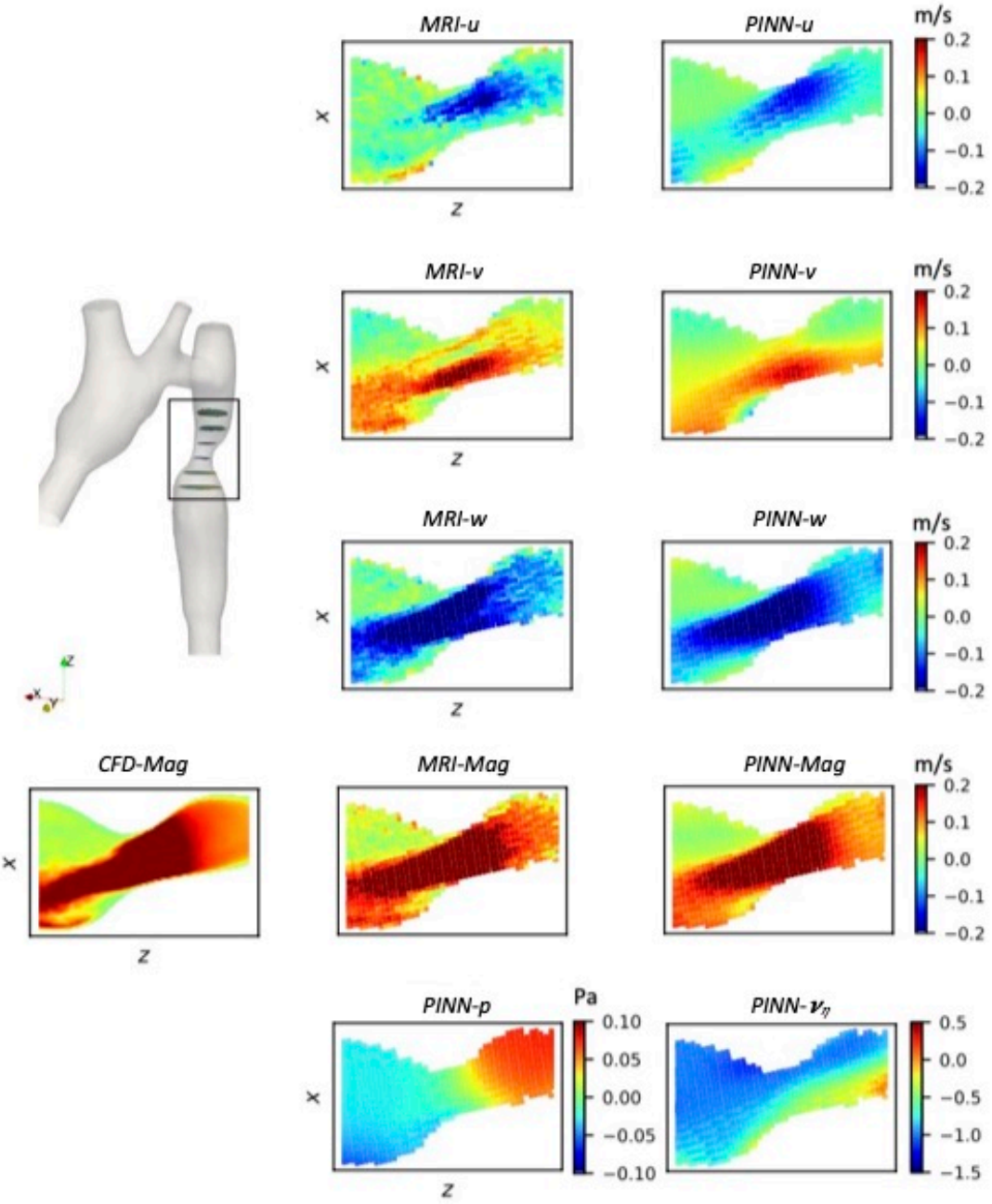

FIGURE 4.18: The velocity and pressure contours of **CoA-1** in a $x-z$ plane. Left, the training data (6 slices) and the velocity magnitude from CFD; middle, the velocity components, magnitude from MRI and the pressure from PINN; right, the velocity components, magnitude and artificial viscosity from PINN.

TABLE 4.6: Comparison of the losses and relative L^2 errors obtained for aortic stenosis flow.

	CoA-1	**CoA-2**
$Loss_{total}$	1.042×10^{-1}	4.47×10^{-2}
$Loss_u$	6.731×10^{-4}	-
$Loss_v$	6.992×10^{-4}	-
$Loss_w$	6.327×10^{-4}	2.822×10^{-4}
$Loss_{equ}$	3.975×10^{-3}	2.405×10^{-3}
Relative L^2 error of u	6.453×10^{-1}	8.576×10^{-1}
Relative L^2 error of v	5.325×10^{-1}	1.056
Relative L^2 error of w	4.563×10^{-1}	3.223×10^{-1}

For MRI, obtaining all three high-precision velocity components in a volume with 4D PC MRI sometimes is time-consuming and difficult, whereas it is relatively easier to obtain the velocity component perpendicular to the scanning plane using 2D PC MRI. Thus, another case, **CoA-2**, was conducted as an attempt to test the ability of PINN for flow prediction using one velocity component from MRI. In this case, the input variables were the spatial location of the pixels (6 slices only) and the velocity component in the main flow direction, i.e., x, y, z, and w. The contribution parameters were $a = 150$, $b = 1$, and $c = 0$. The network was 10*(5*100) and the convergence of the losses can be found in Figure 4.16. It can be seen that the velocity component w converges smoothly. $Loss_{equ}$ and $Loss_{data}$ change from large oscillations (learning rate of $1e-3$) to small fluctuations (learning rate of $1e-4$), same as the case with all three velocity components. The PINN-obtained flow is given in Figure 4.20. Using CFD as a standard, PINN-obtained flow is similar to MRI-obtained flow, but again more continuous and smoother. There are small deviations in some places, such as the recirculation area after the stenosis. The losses and relative L^2-errors are summarized in Table 4.6, where the data constraint for **CoA-1** is (x, y, z, u, v, w) and the data constraint for **CoA-2** is (x, y, z, w). It is found that the losses and errors of **CoA-2** are close to those of **CoA-1**.

The scatter plots of the velocity magnitude distribution are shown in Figure 4.21. The velocity distribution of PINN is similar to that of MRI, but the number of points with larger deviations is reduced. In the region with high CFD velocity, PINN has some points distributed below the blue line, meaning that they are slightly smaller than the CFD data. Moreover, from **CoA-1** to **CoA-2**, even only one velocity component was used for training, RMSE and R^2 don't change too much. This implies that PINN can accomplish the prediction of the volumetric flow and all velocity components using only a single velocity component on finite slices.

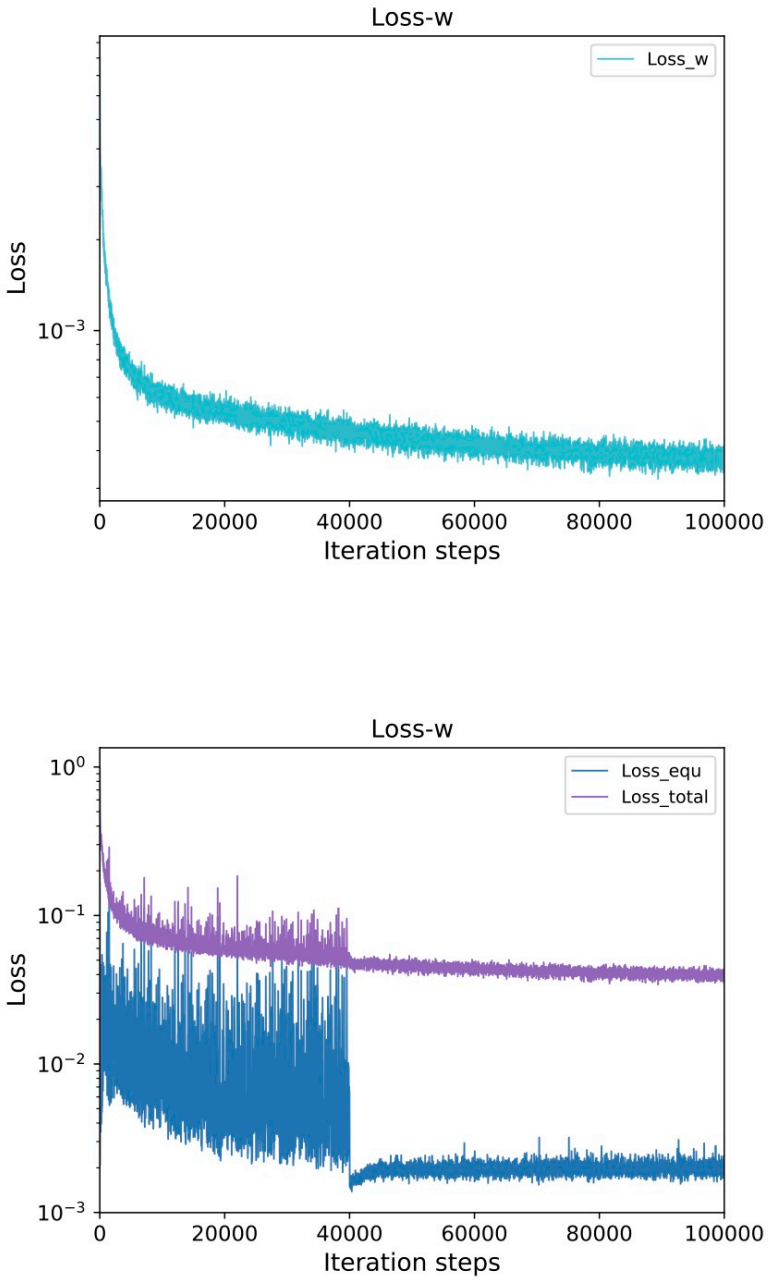

FIGURE 4.19: The losses monitored during the training process in **CoA-2**. The learning rate is 10^{-3} until 40,000 iterations, after which it becomes 10^{-4}. Contribution parameters $a = 150$, $b = 1$, and $c = 0$.

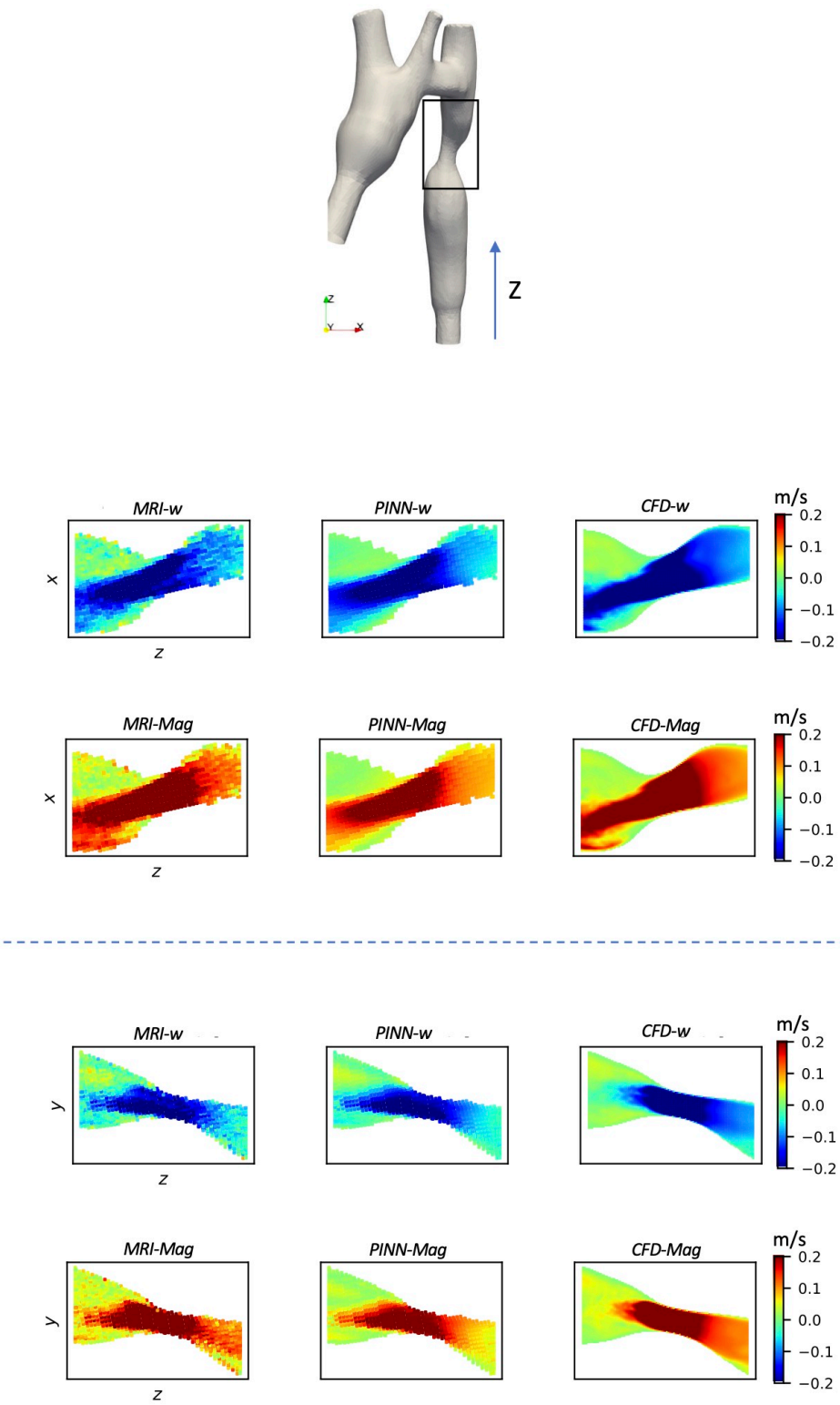

FIGURE 4.20: The velocity contours of **CoA-2** in a $x-z$ plane and a $y-z$ plane. Top, the location of stenosis; middle, the velocity contours from MRI/PINN/CFD in a $x-z$ plane; bottom, the velocity contours from MRI/PINN/CFD in a $y-z$ plane.

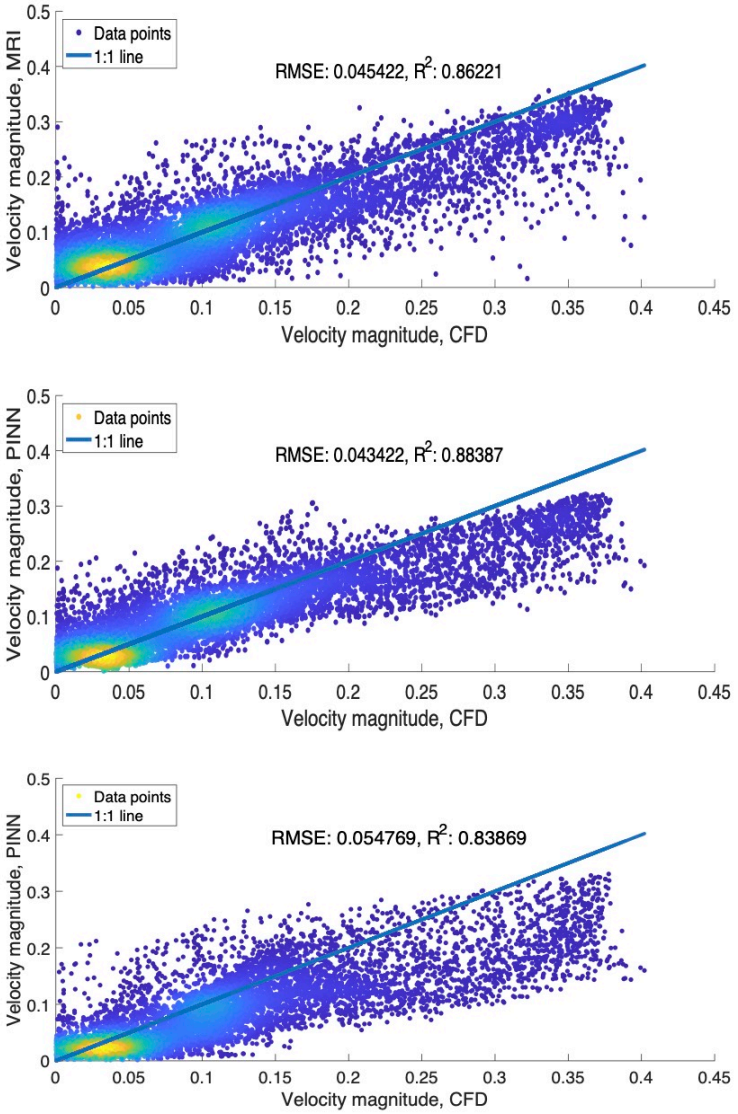

FIGURE 4.21: Scatter plot of the velocity magnitude distribution in **CoA-1** and **CoA-2** (Unit: m/s). Points on the blue line indicate a better fit for PINN/MRI data and CFD data. Top, comparison of MRI data and CFD data; middle and bottom, comparison of **CoA-1**/**CoA-2** data and CFD data. RMSE is the root mean square error and R^2 is the coefficient of determination.

4.3 Discussion and Conclusion

Blood flow in our body is laminar in general, but in some cases it may become transitional or turbulent, such as with stenosis cased by congenital or under pathological conditions. However, it is often difficult to obtain an accurate flow field using a single method of hemodynamic study. Therefore, it is necessary to combine multiple techniques to accomplish accurate blood flow visualization and investigation.

PC MRI plays a very important role in the visualization of human blood flow. As we observed in the above cases, the flows measured by PC MRI clearly show reasonable pattern. Although the images from PC MRI contain some deviations in the flow field, compared with the CFD data. These deviations arise from the noise, dead pixels and experimental errors that are inevitable during the data acquisition and image reconstruction. In in vitro measurements of simplified phantoms of normal and stenotic vessels, as shown in Section 4.2.1 and Section 4.2.2, MRI accurately captured the main features for both flows, and more noise were found in the stenotic vessel due to more complex flow therein. The noise was distributed globally, but most pronounced in the region close to the vessel boundaries. The ability of PC MRI to measure complex flow, such as those in complex geometries and even turbulent flows, was further proved in Section 4.2.3, where a realistic aortic phantom with stenosis was considered.

On the other hand, CFD, by discretizing time and space and solving the physical equations numerically, can resolve blood flow accurately with a higher temporal and spatial resolution than quite a few experimental measurements, such as MRI. Thus CFD has found synergistic use in hemodynamic studies [122, 131]. However, taking aortic flow as an example, in addition to the precise vascular structure geometry, the boundary conditions of the inlet and outlet are crucial for CFD and have a very strong influence on the obtained flow pattern and hemodynamic parameters [36, 95, 82, 81]. Moreover, laminar and turbulent flows as well as transitional flows may occur simultaneously in the aorta due to complex personalized geometries [68, 121]. This in turn poses a new challenge for CFD. In order to resolve such complex flow, one needs to choose a turbulence model and balance accuracy and computational requirement, as discussed in Chapter 3.

PINN is a scientific machine learning technique to solve complex problems containing PDE by training NN to minimize a loss function [27]. The training process is under the unsupervised learning without the labeled data. Unlike data-driven approaches, it does not require a large number of samples, which is particularly suitable for applications in personalized medicine. Numerous studies have shown that PINN can predict the flow even white noise was artificially added.

For hemodynamic applications, prediction with medical image-based PINN can exclude the effect of noisy MRI data so that the flow field of interest satisfies the laws of physics. Accurate flow fields can also be predicted with a small amount of data. For example, in the test case of realistic aortic geometry, the amount of constrained

data is about 14% of the total predicted data. Moreover, the selection of sparse data as training data also solves the limitation of acquisition resolution of PC MRI. In addition, as shown in Figure 4.20, it was found that the three-dimensional velocity field can be predicted using only the velocity component in one direction. Considering the advantages and disadvantages of 2D PC MRI and 4D PC MRI in clinical applications, as discussed in Chapter 2, this feature would provide the possibility to predict the 4D flow field using 2D PC MRI data. In addition to the choice of training data, the structure of the fully connected NN also has an impact on the prediction data, as verified in Table 4.4. With PINN, other hemodynamic parameters, such as pressure distribution, pressure drop and Reynolds number, can also be predicted in addition to the velocity field. Finally, compared to CFD, image-based PINN does not require precise boundary conditions or turbulence models, thus greatly increasing its versatility.

4.4 Summary

MRI is one of the most important experimental methods for hemodynamics, and the blood flow obtained by it inevitably suffers from some noise and errors. In this chapter I proposed a new strategy to accomplish blood flow prediction by combining MRI and PINN. Specifically, using the spatial position of voxels obtained by MRI as input, accompanied by a small amount of velocity information from MRI, and then using the flow governing equations as physical constraint, PINN succeeded in obtaining volumetric hemodynamics. Laminar and turbulent flows in three-dimensional printed phantoms, representing idealized and realistic vessel geometries, were successfully predicted by PINN. This study shows that image-based PINN can avoid the shortcomings of MRI and CFD, which are currently widely used for hemodynamic studies, and use spare and noisy data to quantitatively predict blood flow. Therefore, it promises to be a new avenue for hemodynamic studies and clinical applications.

Chapter 5

Summary and Outlook

5.1 Summary

Cardiovascular diseases are circulatory diseases that affect the heart and blood vessels, and are characterized by high morbidity, disability, mortality, recurrence and complications. The circulatory system is thought of as a system that involves complex blood flows. Hemodynamics is often used to study blood flow in such systems under normal and pathological conditions to understand the mechanisms of various diseases and to treat them accordingly. Different methods, such as experimental measurement, numerical modeling and machine learning, have been adopted for hemodynamic studies. However, each method has its own pros and cons. MRI can provide flow fields and geometric information, but it cannot be used for prediction of surgery and the acquired data are noisy. Numerical modeling, specifically CFD, can provide accurate and high-resolution flow fields, but the accuracy of the results is strongly influenced by the boundary conditions and numerical methods selected. PINN, a new method that combines data and physical laws, is still under development, and further development and validation is needed for clinical applications.

The combination of MRI, CFD, and PINN takes full advantage of each method, allowing better quantification of hemodynamics and better prediction of the outcome of surgical protocols.

The first strategy proposed is for personalized CoA stenting, using an in silico model that combines prediction of aortic geometry after stenting based on MRI with hemodynamic prediction using CFD. First, numerical simulations of flow in the aorta were performed using LBM, with boundary conditions extracted from PC MRI. LBM based LES was shown to resolve accurate aortic flow at an acceptable computational cost, compared to MRI-obtained flow in a three-dimensional printed phantom and in a volunteer. Subsequently, in silico stenting was performed in a CoA patient by predicting the deformed aortic geometries and blood flows therein after stent implantation. An optimal stent was selected by evaluating hemodynamic parameters, such as pressure drop and maximum wall shear stress from in silico modelings. Although only aorta was considered, such strategy can be extended to other stenosis, and can be used to help clinicians to evaluate surgical plans before intervention.

The second strategy is to perform the flow prediction using PINN based on MRI-obtained flow. Specifically, within the ML framework, the spatial location of voxels obtained from MRI was used as input, flow information (such as velocity components, pressure, etc.) was output, accompanied by a small amount of velocity information from MRI as data constraint, and flow governing equations (continuity equation and NSE) were used as physical constraint. First, PINN successfully predicted the flows within three-dimensional printed phantoms of normal and stenotic vessels respectively. PINN successfully located the wall in the normal vessel model and to some extent in the stenotic vessel model. Secondly, the prediction of turbulent flow in a realistic aortic geometry by PINN was achieved. It is shown that three-dimensional turbulent flow can be predicted based on a small amount of 4D PC MRI data, even using only one velocity component as data constraint. These studies show that image-based PINN can overcome the drawbacks of MRI and CFD, which are currently widely used for hemodynamic studies, and predict flow quantitatively using small amounts of noisy data. It thus promises to be a new avenue for hemodynamic studies and clinical applications.

In conclusion, in this dissertation I have developed two new strategies by combining different methods based on physical information and applied them for quantitative study of hemodynamics. Bringing together physics, medicine and computer science, these strategies may shed light on precision medicine and personalized medical therapy.

5.2 Future Work

There are also some possible improvements that might be considered in the future. For the in silico modeling for personalized stenting, (1) firstly, while the boundary conditions using temporal velocities are sufficient to complete the current CFD evaluation, modeling of the whole cardiac cycle could be considered to obtain more information on the instantaneous flow field. One option is to involve the Windkessel model, which takes into account the resistance of the vascular network and the capacitance of the vascular network, in the boundary conditions. Corresponding model parameters can be obtained from MRI data. (2) Secondly, the effect of vessel deformation as well as the geometry of the stent on the flow can be considered. Of course, this requires accurate mechanical properties of the aortic wall as theoretical support. (3) Finally, although CFD can accurately solve hemodynamic problems, it is still time consuming. The use of ML for preprocessing work could be considered in the future.

For the image-based flow prediction, (1) firstly the ability of PINN to predict the location of the vessel wall needs to be further improved. Finding the vessel wall, in the current blood flow prediction, is mainly based on the phase images of PC MRI. The combination of magnitude and phase images of PC MRI for vessel wall prediction could provide a better way. (2) Secondly, in addition to the prediction

of velocity field and pressure field, other hemodynamic parameters such as WSS should be considered. (3) Thirdly, to obtain more accurate flow field, in addition to fully connected feedforward NN used in this study, other structural NN such as convolutional NN or recursive NN might be helpful and need to be tested. (4) Finally, the flow predictions in this dissertation are based on in vitro experiments, while prediction based on in vivo time-dependent flow is the ultimate target and needs to be done in the future.

Bibliography

[1] M. Abadi et al. *TensorFlow: Large-Scale Machine Learning on Heterogeneous Systems*. Software available from tensorflow.org. 2015. URL: https://www.tensorflow.org/.

[2] A. Adler et al. "Simulation of Flowing Spins in MRI using the Lattice Boltzmann Method". In: *ISMRM 2021. Proc. Intl. Soc. Mag. Reson. Med.* (2021).

[3] M. Alishiri et al. "Drug delivery and adhesion of magnetic nanoparticles coated nanoliposomes and microbubbles to atherosclerotic plaques under magnetic and ultrasound fields". In: *Engineering Applications of Computational Fluid Mechanics* 15.1 (2021), pp. 1703–1725. DOI: 10.1080/19942060.2021.1989042.

[4] W. Alkashkari, S. Albugami, and Z. M. Hijazi. "Management of coarctation of the aorta in adult patients: State of the art". In: *Korean Circulation Journal* 49.4 (2019), pp. 298–313. ISSN: 17385555. DOI: 10.4070/kcj.2018.0433.

[5] J. Aoki et al. "Coronary Artery Aneurysms After Drug-Eluting Stent Implantation". In: *JACC: Cardiovascular Interventions* 1 (1 2007), pp. 14–21. DOI: 10.1016/j.jcin.2007.10.004.

[6] A. Arzani, J. X. Wang, and R. M. D'Souza. "Uncovering near-wall blood flow from sparse data with physics-informed neural networks". In: *Physics of Fluids* 33 (7 July 2021). ISSN: 10897666. DOI: 10.1063/5.0055600.

[7] M. R. Avendi, A. Kheradvar, and H. Jafarkhani. "Fully automatic segmentation of heart chambers in cardiac MRI using deep learning". In: *Journal of Cardiovascular Magnetic Resonance* 18.S1 (2016), pp. 2–4. ISSN: 1532-429X. DOI: 10.1186/1532-429x-18-s1-p351.

[8] P. Aymeric et al. "Evaluation and Verification of Fast Computational Simulations of Stent-Graft Deployment in Endovascular Aneurysmal Repair". In: *Frontiers in Medical Technology* 3 (2021), p. 704806. ISSN: 2673-3129. DOI: 10.3389/fmedt.2021.704806.

[9] M. Barakat, D. Dvir, and A. N. Azadani. "Fluid Dynamic Characterization of Transcatheter Aortic Valves Using Particle Image Velocimetry". In: *Artif Organs* 42.11 (2018), E357–E368. DOI: doi:10.1111/aor.13290.

[10] F. Basombrío et al. "Numerical Experiments in Complex Hæmodynamic Flows. Non-Newtonian Effects". In: *International Journal of Computational Fluid Dynamics* 16 (Nov. 2002), pp. 231–246. DOI: doi.org/10.1080/1061856021000025111.

[11] G. K. Batchelor. *"An Introduction to Fluid Dynamics"*. Cambridge University Press, 2012.

[12] R. Benzi, S. Succi, and M. Vergassola. "The lattice Boltzmann equation: theory and application". In: *Physics Reports* 222.3 (1992), pp. 145–197.

[13] P. Berg et al. "Virtual stenting of intracranial aneurysms: A pilot study for the prediction of treatment success based on hemodynamic simulations". In: *International Journal of Artificial Organs* 41.11 (2018), pp. 698–705. ISSN: 03913988. DOI: 10.1177/0391398818775521.

[14] M. Bouzidi, M. Firdauss, and P. J. Lallemand. "Momentum transfer of a Boltzmann-lattice fluid with boundaries". In: *Physics of Fluids* 13 (2001), pp. 3452–3459. DOI: doi.org/10.1063/1.1399290.

[15] M. C. Brindise et al. "Hemodynamics of Stent Implantation Procedures in Coronary Bifurcations: An In Vitro Study". In: *Annals of Biomedical Engineering* 45 (3 Mar. 2017), pp. 542–553. ISSN: 15739686. DOI: 10.1007/s10439-016-1699-y.

[16] A. D. Caballero and S. Laín. "A Review on Computational Fluid Dynamics Modelling in Human Thoracic Aorta". In: *Cardiovascular Engineering and Technology* 4.2 (2013), pp. 103–130. ISSN: 18694098. DOI: 10.1007/s13239-013-0146-6.

[17] J. V. Callaham et al. "Learning dominant physical processes with data-driven balance models". In: *Nature Communications* 12 (1 Dec. 2021). ISSN: 20411723. DOI: 10.1038/s41467-021-21331-z.

[18] J. R. Cebral et al. "Efficient pipeline for image-based patient-specific analysis of cerebral aneurysm hemodynamics: technique and sensitivity." In: *IEEE Trans Med Imaging* 24 (Apr. 2005), pp. 457–467. DOI: 10.1109/tmi.2005.844159.

[19] A. U. Chatzizisis et al. "Role of Endothelial Shear Stress in the Natural History of Coronary Atherosclerosis and Vascular Remodeling: Molecular, Cellular, and Vascular Behavior". In: *Journal of the American College of Cardiology* 49 (25 2007), pp. 78–85. ISSN: 0735-1097. DOI: 10.1016/j.jacc.2007.02.059.

[20] Y. S. Chatzizisis et al. "Role of Endothelial Shear Stress in the Natural History of Coronary Atherosclerosis and Vascular Remodeling. Molecular, Cellular, and Vascular Behavior". In: *Journal of the American College of Cardiology* 49 (25 June 2007), pp. 2379–2393. DOI: 10.1016/j.jacc.2007.02.059.

[21] D. Chen et al. "Virtual stenting with simplex mesh and mechanical contact analysis for real-time planning of thoracic endovascular aortic repair". In: *Theranostics* 8.20 (2018), pp. 5758–5771. DOI: 10.7150/thno.28944.

[22] H. Chen et al. "Extended Boltzmann kinetic equation for turbulent flows". In: *Science* 301.5633 (2003), pp. 633–636. ISSN: 00368075. DOI: 10.1126/science.1085048.

[23] S. Chen and G. D. Doolen. "Lattice Boltzmann method for fluid flows". In: *Annual review of fluid mechanics* 30.1 (1998), pp. 329–364.

[24] Z. Cheng et al. "Geometric and Flow Features of Type B Aortic Dissection: Initial Findings and Comparison of Medically Treated and Stented Cases". In: *Annals of Biomedical Engineering* 43.1 (2015), pp. 177–189. ISSN: 15739686. DOI: 10.1007/s10439-014-1075-8.

[25] Z. Cheng et al. "Initial findings and potential applicability of computational simulation of the aorta in acute type B dissection". In: *Journal of Vascular Surgery* 57.2 SUPPL. (2013), 35S–43S. ISSN: 10976809. DOI: 10.1016/j.jvs.2012.07.061.

[26] M. Cibis et al. "The effect of resolution viscous dissipation measured with 4D flow MRI in patients with fontan circulation: Evaluation using computational fluid dynamics". In: *Journal of Biomechanics* 48.12 (2015), pp. 2984–2989. DOI: 10.1016/j.jbiomech.2015.07.039.

[27] S. Cuomo et al. "Scientific Machine Learning Through Physics–Informed Neural Networks: Where we are and What's Next". In: *Journal of Scientific Computing* 92 (3 2022). DOI: 10.1007/s10915-022-01939-z.

[28] M. Czerny, M. Cejna, and D. et al. Hutschala. "Stent-Graft Placement in Atherosclerotic Descending Thoracic Aortic Aneurysms: Midterm Results". In: *Journal of Endovascular Therapy* 11 (1 2004), pp. 26–32. DOI: 10.1177/152660280401100103.

[29] L. Dempere-Marco et al. *Lecture Notes in Computer Science*. Springer Verlag, 2006.

[30] D. D'Humières et al. "Multiple-relaxation-time lattice Boltzmann models in three dimensions". In: *Philosophical Transactions of the Royal Society A: Mathematical, Physical and Engineering Sciences* 360.1792 (2002), pp. 437–451. ISSN: 1364503X. DOI: 10.1098/rsta.2001.0955.

[31] H. N. Dixit and V. Babu. "Simulation of high Rayleigh number natural convection in a square cavity using the Lattice Boltzmann method". In: *International Journal of Heat and Mass Transfer* 49 (2006), pp. 727–739. DOI: 10.1016/j.ijheatmasstransfer.2005.07.046.

[32] M. M. Dua and R. L. Dalman. "Hemodynamic influences on abdominal aortic aneurysm disease: Application of biomechanics to aneurysm pathophysiology". In: *The Permanente Journal* 53.2 (1-2 2010), pp. 11–21. DOI: 10.1016/j.vph.2010.03.004.

[33] P. Dyverfeldt et al. "4D flow cardiovascular magnetic resonance consensus statement". In: *Journal of Cardiovascular Magnetic Resonance* 17.1 (2015), pp. 1–19. ISSN: 1532429X. DOI: 10.1186/s12968-015-0174-5.

[34] O. Filippova and D. Hänel. "Grid Refinement for Lattice-BGK Models". In: *Journal of Computational Physics* 147 (1998), pp. 219–228. DOI: 10.1006/jcph.1998.6089.

[35] T. Frauenfelder et al. "Computational fluid dynamics: Hemodynamic changes in abdominal aortic aneurysm after stent-graft implantation". In: *CardioVascular and Interventional Radiology* 29 (4 Aug. 2006), pp. 613–623. ISSN: 01741551. DOI: 10.1007/s00270-005-0227-5.

[36] D. Gallo et al. "On the use of in vivo measured flow rates as boundary conditions for image-based hemodynamic models of the human aorta: implications for indicators of abnormal flow". In: *Annals of Biomedical Engineering* 40 (2012), 729–741. DOI: 10.1007/s10439-011-0431-1.

[37] H. Gao, L. Sun, and J. X. Wang. "Super-resolution and denoising of fluid flow using physics-informed convolutional neural networks without high-resolution labels". In: *Physics of Fluids* 33 (7 2021). DOI: 10.1063/5.0054312.

[38] D. N. Ghista and F. Kabinejadian. "Coronary artery bypass grafting hemodynamics and anastomosis design: a biomedical engineering review". In: (2013). URL: http://www.biomedical-engineering-online.com/content/12/1/129.

[39] J. Golledge and P. E. Norman. "Atherosclerosis and abdominal aortic aneurysm: cause, response, or common risk factors?" In: *Arterioscler Thromb Vasc Biol* 30 (6 2016). DOI: 10.1161/ATVBAHA.110.206573.

[40] Z. L. Guo, C. G. Zheng, and B. C. Shi. "An extrapolation method for boundary conditions in lattice Boltzmann method". In: *Physics of Fluids* 14 (2002), pp. 2007–2010. DOI: doi.org/10.1063/1.1471914.

[41] M. M. A. Hadhoud et al. "Left Ventricle Segmentation in Cardiac MRI Images". In: *American Journal of Biomedical Engineering* 2.3 (2012), pp. 131–135. ISSN: 2163-1050. DOI: 10.5923/j.ajbe.20120203.07.

[42] X. He and L. S. Luo. "A priori derivation of the lattic Boltzmann equation". In: *Physical Review E* 55 (1996), R6333–R6336.

[43] X. He and L. S. Luo. "Theory of the lattice Boltzmann method: From the Boltzmann equation to the lattice Boltzmann equation". In: *Physical Review E* 55.6 (1997), pp. 6811–6820. ISSN: 1063651X. DOI: 10.1103/PhysRevE.56.6811.

[44] Y. He, Y. Wang, and Q. Li. *Lattice Boltzmann method: Theory and applications*. 2009.

[45] T. Henn et al. "Aortic coarctation simulation based on the lattice Boltzmann method: Benchmark results". In: *Lecture Notes in Computer Science (including subseries Lecture Notes in Artificial Intelligence and Lecture Notes in Bioinformatics)*. Vol. 7746 LNCS. 2013, pp. 34–43. ISBN: 9783642369605. DOI: 10.1007/978-3-642-36961-2_5.

[46] J. Hoffman and S. Kaplan. "The incidence of congenital heart disease". In: *Journal of the American College of Cardiology* 39.12 (2002), pp. 1890–1900. ISSN: 07351097. DOI: 10.1016/S0735-1097(02)01886-7.

[47] K. Hoshina et al. "Wall shear stress and strain modulate experimental aneurysm cellularity". In: *Journal of Vascular Surgery* 37 (5 2003), p. 1067. DOI: 10.1016/S0741-5214(03)70052-4.

[48] K. Huang et al. "Machine Learning-Based Optimal Mesh Generation in Computational Fluid Dynamics". In: *arXiv:2102.12923* (2021).

[49] J. D. Humphrey and M. A. Schwartz. "Vascular Mechanobiology: Homeostasis, Adaptation, and Disease". In: *Annual Review of Biomedical Engineering* 23 (2021), pp. 1–27. ISSN: 15454274. DOI: 10.1146/annurev-bioeng-092419-060810.

[50] D. Kontaxakis A. Parmigiani D. Lagrava F. Brogi M. B. Belgacem Y. Thorimbert S. Leclaire S. Li F. Marson J. Lemus C. Kotsalos R. Conradin C. Coreixas R. Petkantchin F. Raynaud J. Beny B. Chopard J. Latt O. Malaspinas. "Palabos: Parallel Lattice Boltzmann Solver". In: *Computers & Mathematics with Applications* 81 (2021), pp. 334–350. ISSN: 0898-1221. DOI: https://doi.org/10.1016/j.camwa.2020.03.022.

[51] D. J. JDUCHI and Y. Singer. "Adaptive Subgradient Methods for Online Learning and Stochastic Optimization". In: *Journal of Machine Learning Research* 12 (2011), pp. 2121–2159. URL: http://jmlr.org/papers/v12/duchi11a.html.

[52] M. Kaminogo, M. Yonekura, and S. Shibata. "Incidence and outcome of multiple intracranial aneurysms in a defined population". In: *Stroke* 34.1 (2003), pp. 16–21. DOI: 10.1161/01.str.0000046763.48330.ad.

[53] X. Kan et al. "Patient-Specific Virtual Stent-Graft Deployment for Type B Aortic Dissection: A Pilot Study of the Impact of Stent-Graft Length". In: *Frontiers in Physiology* 12.July (2021). ISSN: 1664042X. DOI: 10.3389/fphys.2021.718140.

[54] J. Kang and H. Ha. "Particle Image Velocimetry Investigation of Hemodynamics via Aortic Phantom". In: *J Vis Exp* 180 (2022). DOI: doi:10.3791/63492.

[55] M. Kang and N. J. Jameson. "Physics-informed neural networks: A deep learning framework for solving forward and inverse problems involving nonlinear partial differential equations". In: *Prognostics and Health Management of Electronics: Fundamentals,Machine Learning, and the Internet of Things* (2018). DOI: doi.org/10.1002/9781119515326.

[56] T. Kang, D. Mukherjee, and J. Ryu. "Numerical investigation of carotid stenosis in three-dimensional aortic-cerebral vasculature: pulsatility index, resistive index, time to peak velocity, and flow characteristics". In: *Engineering Applications of Computational Fluid Mechanics* 15.1 (2021), pp. 1645–1665. ISSN: 1997003X. DOI: 10.1080/19942060.2021.1984993.

[57] T. Kang et al. "Effects of progressive carotid stenosis on cerebral haemodynamics: aortic-cerebral 3D patient-specific simulation". In: *Engineering Applications of Computational Fluid Mechanics* 15.1 (2021), pp. 830–847. ISSN: 1997003X. DOI: 10.1080/19942060.2021.1916601.

[58] G. E. Karniadakis et al. "Physics-informed machine learning". In: *Nature Reviews Physics* 3 (6 2021), pp. 422–440. DOI: 10.1038/s42254-021-00314-5.

[59] D. P. Kingma and J. Ba. "Adam: A Method for Stochastic Optimization". In: (Dec. 2014). URL: http://arxiv.org/abs/1412.6980.

[60] D. P. Kingma and J. Ba. "Proceedings of the 3rd International Conference on Learning Representations". In: *ICLR* (2015).

[61] G. Kissas et al. "Machine learning in cardiovascular flows modeling: Predicting arterial blood pressure from non-invasive 4D flow MRI data using physics-informed neural networks". In: *Computer Methods in Applied Mechanics and Engineering* 358 (2020), p. 112623. ISSN: 00457825. DOI: 10.1016/j.cma.2019.112623. URL: https://doi.org/10.1016/j.cma.2019.112623.

[62] C. A. Kousera et al. "A Numerical Study of Aortic Flow Stability and Comparison With In Vivo Flow Measurements". In: *Journal of Biomechanical Engineering* 135.1 (Dec. 2012). 011003. ISSN: 0148-0731. DOI: 10.1115/1.4023132.

[63] T. Krüger et al. *The lattice Boltzmann method: Principles and Practice*. Switzerland : Springer-Verlag, 2017.

[64] D. N. Ku. "Blood flow in arteries". In: *Annual Review of Fluid Mechanics* 29 (1997), pp. 399–434. ISSN: 00664189. DOI: 10.1146/annurev.fluid.29.1.399.

[65] K. Landheer et al. "Theoretical description of modern 1H in Vivo magnetic resonance spectroscopic pulse sequences". In: *Journal of Magnetic Resonance Imaging* 51.4 (2020), pp. 1008–1029. DOI: doi.org/10.1002/jmri.26846.

[66] L. Liang, W. Mao, and W. Sun. "A feasibility study of deep learning for predicting hemodynamics of human thoracic aorta". In: *J Biomech* 23;99:109544 (2020). DOI: 10.1016/j.jbiomech.2019.109544.

[67] G. Litjens et al. "A survey on deep learning in medical image analysis". In: *Med Image Anal* 42 (1 2017), pp. 60–88. DOI: 10.1016/j.media.2017.07.005.

[68] E. L. Manchester et al. "Analysis of Turbulence Effects in a Patient-Specific Aorta with Aortic Valve Stenosis". In: *Cardiovascular Engineering and Technology* 12.4 (2021), pp. 438–453. ISSN: 18694098. DOI: 10.1007/s13239-021-00536-9.

[69] M. Markl, S. Schnell, and A. J. Barker. "4D flow imaging: Current status to future clinical applications". In: *Current Cardiology Reports* 16.5 (2014). ISSN: 15343170. DOI: 10.1007/s11886-014-0481-8.

[70] M. Markl et al. "4D flow MRI". In: *Journal of Magnetic Resonance Imaging* 36.5 (2012), pp. 1015–1036. ISSN: 10531807. DOI: 10.1002/jmri.23632.

[71] M. Markl et al. "4D flow MRI". In: *Journal of Magnetic Resonance Imaging* 36.5 (2012), pp. 1015–1036. DOI: 10.1002/jmri.23632.

[72] R. McCloy and R. Stone. "Science, medicine, and the future: Virtual reality in surgery". In: *BMJ* 323.7318 (2001), pp. 912–915. ISSN: 0959-8138. DOI: 10.1136/bmj.323.7318.912.

[73] D. W. McRobbie. *MRI from Picture to Proton*. Cambridge University Press, 2007.

[74] Z. Meng H.and Wang et al. "Complex hemodynamics at the apex of an arterial bifurcation induces vascular remodeling resembling cerebral aneurysm initiation". In: *Stroke* 38 (6 June 2007), pp. 1924–1931. ISSN: 00392499. DOI: 10.1161/STROKEAHA.106.481234.

[75] H. Mirzaee et al. "MRI-based computational hemodynamics in patients with aortic coarctation using the lattice Boltzmann methods: Clinical validation study". In: *Journal of Magnetic Resonance Imaging* 45 (2017), pp. 139–146. ISSN: 15222586. DOI: 10.1002/jmri.25366.

[76] S. Miyazaki et al. "Validation of numerical simulation methods in aortic arch using 4D Flow MRI". In: *Heart and Vessels* 32.8 (2017), pp. 1032–1044. ISSN: 16152573. DOI: 10.1007/s00380-017-0979-2.

[77] A. M.Nixon, A. Gunel, and B. E. Sumpio. "The critical role of hemodynamics in the development of cerebral vascular disease". In: *J Neurosurg* 112 (6 2010), pp. 1240–1253. ISSN: 2234-8565. DOI: 10.7461/jcen.2014.16.4.335.

[78] A.A. Mohamad. *Lattice Boltzmann Method Fundamentals and Engineering Applications with Computer Codes, Second Edition*. London: Springer-Verlag, 2012.

[79] P. Moin and K. Mahesh. "DIRECT NUMERICAL SIMULATION: A Tool in Turbulence Research". In: *Annual Review of Fluid Mechanics* 30.1 (1998), pp. 539–578. DOI: 10.1146/annurev.fluid.30.1.539.

[80] P. R. Moran. "A flow velocity zeugmatographic interlace for NMR imaging in humans". In: *Magnetic Resonance Imaging* 1.197–203 (1982).

[81] U. Morbiducci et al. "Inflow boundary conditions for image-based computational hemodynamics: impact of idealized versus measured velocity profiles in the human aorta". In: *J Biomech* 46 (1 2012), 102–9. DOI: 10.1016/j.jbiomech.2012.10.012.

[82] U. Morbiducci et al. "Outflow conditions for image-basedhemodynamic models of the carotid bifurcation: implications for indicators ofabnormal flow". In: *J. Biomech. Eng.* 132 (2010), p. 091005. DOI: 10.1115/1.4001886.

[83] P. Moser et al. "Modeling of 3D Blood Flows with Physics-Informed Neural Networks: Comparison of Network Architectures". In: *Fluids* 8 (2 Jan. 2023), p. 46. ISSN: 2311-5521. DOI: 10.3390/fluids8020046. URL: https://www.mdpi.com/2311-5521/8/2/46.

[84] D. Mozaffarian, E. Benjamin, and A. Go. "Heart disease and stroke statistics-2016 update. A report from the American Heart Association". In: *Circulation* 133 (2016). DOI: 10.1161/CIR.0000000000000350.

[85] M. Neugebauer et al. "Interactive virtual stent planning for the treatment of coarctation of the aorta". In: *International Journal of Computer Assisted Radiology and Surgery* 11.1 (2016), pp. 133–144. ISSN: 18616429. DOI: 10.1007/s11548-015-1220-3.

[86] C. W. Ong et al. "Computational Fluid Dynamics Modeling of Hemodynamic Parameters in the Human Diseased Aorta: A Systematic Review". In: *Ann Vasc Surg*. 63 (2020). DOI: 10.1016/j.avsg.2019.04.032.

[87] World Health Organization. "Cardiovascular diseases (cvds)". In: *https://www.who.int/news-room/fact-sheets/detail/cardiovascular-diseases(cvds)* (1 2020).

[88] S. Orszag. "Analytical Theories of Turbulence". In: *Journal of Fluid Mechanics* 41 (2 1970), pp. 363–386. DOI: 10.1017/S0022112070000642.

[89] E. Oubel et al. *Analysis of intracranial aneurysm wall motion and its effects on hemodynamic patterns*. Vol. 6511. SPIE, 2007, pp. 706–713.

[90] M. O'Donnell. "NMR blood flow imaging using multiecho, phase contrast sequences". In: *Medical Physics* 12.59–64 (1982). DOI: 10.1118/1.595736.

[91] H. C. Hazlett R. G. Smith P. A. Yushkevich J. Piven and G. Gerig S. Ho J. C. Gee. "User-guided 3D active contour segmentation of anatomical structures: Significantly improved efficiency and reliability". In: *NeuroImage* 31.3 (2006), pp. 1116–1128. ISSN: 1053-8119. DOI: https://doi.org/10.1016/j.neuroimage.2006.01.015.

[92] A. S. Patel and K. G. Burnand. "Cardiovascular haemodynamics and shock". In: *Surgery (Oxford)* 27 (Nov. 2009), pp. 459–464. DOI: 10.1016/J.MPSUR.2009.09.009.

[93] T. J. Pedley. *The Fluid Mechanics of Large Blood Vessels*. Cambridge Monographs on Mechanics. Cambridge University Press, 1980. DOI: 10.1017/CBO9780511896996.

[94] C. Pinter, A. Lasso, and G. Fichtinger. "Polymorph segmentation representation for medical image computing". In: *Computer Methods and Programs in Biomedicine* 171 (2019), pp. 19–26. ISSN: 0169-2607. DOI: https://doi.org/10.1016/j.cmpb.2019.02.011.

[95] S. Pirola et al. "On the choice of outlet boundary conditions for patient-specific analysis of aortic flow using computational fluid dynamics". In: *Journal of Biomechanics* 60 (2017), pp. 15–21. ISSN: 18732380. DOI: 10.1016/j.jbiomech.2017.06.005.

[96] S. B. Pope. "Turbulent Flows". In: *Cambridge University Press* (2000). DOI: 10.1017/CBO9780511840531.011.

[97] W. V. Potters et al. "4D MRI-based wall shear stress quantification in the carotid bifurcation: a validation study in volunteers using computational fluid dynamics". In: *Journal of Cardiovascular Magnetic Resonance* (2014). DOI: 10.1186/1532-429x-16-s1-p162.

[98] Y. H. Qian, D. D'Humières, and P. Lallemand. "Lattice BGK models for Navier-Stokes equation". In: *Europhysics Letter* 17 (1992), pp. 479–484. DOI: 10.1209/0295-5075/17/6/001.

[99] D. Rafieianzab et al. "The effect of coarctation degrees on wall shear stress indices". In: *Scientific Reports* 11.1 (2021), pp. 1–13. ISSN: 20452322. DOI: 10.1038/s41598-021-92104-3.

[100] V. Raghav, S. Sastry, and N. Saikrishnan. "Experimental Assessment of Flow Fields Associated with Heart Valve Prostheses Using Particle Image Velocimetry (PIV): Recommendations for Best Practices". In: *Cardiovasc Eng Technol* 9.3 (2018), pp. 273–287. DOI: doi:10.1007/s13239-018-0348-z.

[101] M. Raissi, A. Yazdani, and G. M. Karniadakis. "Hidden fluid mechanics: Learning velocity and pressure fields from flow visualizations". In: *Science* 367.6481 (2020), pp. 1026–1030. ISSN: 10959203. DOI: 10.1126/science.aaw4741.

[102] M. Raissi1, P. Perdikaris, and G.E. Karniadakis. "Physics-informed neural networks: A deep learning framework for solving forward and inverse problems involving nonlinear partial differential equations". In: *Journal of Computational Physics* 378 (2019), 686–707. DOI: 10.1063/5.0055600.

[103] P. Ramachandran, B. Zoph, and Q. V. Le. "Searching for Activation Functions". In: *ArXiv* abs/1710.05941 (2018).

[104] M. D. Reller et al. "Prevalence of Congenital Heart Defects in Metropolitan Atlanta, 1998-2005". In: *Journal of Pediatrics* 153.6 (2008), pp. 807–813. ISSN: 00223476. DOI: 10.1016/j.jpeds.2008.05.059.

[105] V. C. Rispoli et al. "Computational fluid dynamics simulationsof blood flow regularized by 3D phase contrast MRI". In: *Biomedical Engineering Online* 14.1 (2015), p. 110. DOI: doi.org/10.1186/s12938-015-0104-7.

[106] G. A. Roth et al. "Global Burden of Cardiovascular Diseases and Risk Factors, 1990-2019: Update From the GBD 2019 Study". In: *Journal of the American College of Cardiology* 76.25 (2020), pp. 2982–3021. ISSN: 15583597. DOI: 10.1016/j.jacc.2020.11.010.

[107] S. Ruder. "An overview of gradient descent optimization algorithms". In: (Sept. 2016). URL: http://arxiv.org/abs/1609.04747.

[108] P. Sagaut. "Large Eddy Simulation for Incompressible Flows (Third ed.)" In: *Springer* (2006). DOI: 10.1017/CBO9780511840531.011.

[109] S. Saitta et al. "Evaluation of 4D flow MRI-based non-invasive pressure assessment in aortic coarctations". In: *Journal of Biomechanics* 94 (2019), pp. 13–21. ISSN: 18732380. DOI: 10.1016/j.jbiomech.2019.07.004.

[110] K. S. Saladin. *Human anatomy (3rd Edition))*. New York: McGraw-Hill, 2011.

[111] H. E. Salman and H. C. Yalcin. "Computational modeling of blood flow hemodynamics for biomechanical investigation of cardiac development and disease". In: *Journal of Cardiovascular Development and Disease* 8 (2 Feb. 2021), pp. 1–27. DOI: 10.3390/JCDD8020014.

[112] H. E. Salman et al. "Biomechanical Investigation of Disturbed Hemodynamics Induced Tissue Degeneration in Abdominal Aortic Aneurysms Using Computational and Experimental Techniques". In: *Frontiers in Bioengineering and Biotechnology* 7 (May 2019). DOI: 10.3389/fbioe.2019.00111.

[113] R. Schmidt and K. Singh. "Meshmixer: an interface for rapid mesh composition". In: *In: ACM SIGGRAPH Talks; 2010; Los Angeles, NY, USA* 301 (2003). DOI: https://doi.org/10.1145/1837026.1837034.

[114] T. W. Secomb. "Hemodynamics". In: *Comprehensive Physiology* 6 (2 Apr. 2016), pp. 975–1003. ISSN: 20404603. DOI: 10.1002/cphy.c150038.

[115] C. Shu, X. D. Niu, and Y. T. Chew. "Theory of the lattice Boltzmann method: From the Boltzmann equation to the lattice Boltzmann equation". In: *Physical Review E* 56 (1997), R6811–R6817. DOI: 10.1103/PhysRevE.56.6811.

[116] J. Smagorinsky. "General Circulation Experiments with the Primitive Equations". In: *Monthly Weather Review* 91 (3 2006), pp. 99–164. DOI: 10.1175/1520-0493(1963)091<0099:GCEWTP>2.3.CO;2.

[117] J. Smagorinsky. "General Circulation Experiments with the Primitive Equations. Part I, the Basic Experiment". In: *Monthly Weather Review* 91(3) (1963), pp. 99–164. DOI: 10.1175/1520-0493(1963)091<0099:GCEWTP>2.3.CO;2.

[118] G. Soulat, P. McCarthy, and M. Markl. "4D Flow with MRI". In: *Annual Review of Biomedical Engineering* 22 (2020), pp. 103–126. ISSN: 15454274. DOI: 10.1146/annurev-bioeng-100219-110055.

[119] Z. Stankovic et al. "4D flow imaging with MRI". In: *Cardiovascular diagnosis and therapy* 4.2 (2014), pp. 173–192. DOI: 10.3978/j.issn.2223-3652.2014.01.02. URL: http://cdt.amegroups.com/article/view/3630/4523.

[120] H. C. Stary et al. "A Definition of Advanced Types of Atherosclerotic Lesions and a Histological Classification of Atherosclerosis". In: *Circulation* 92 (1995), pp. 1355–1374. DOI: 10.1161/01.CIR.92.5.1355.

[121] P. D. Stein and H. N. Sabbah. "Turbulent blood flow in the ascending aorta of humans with normal and diseased aortic valves". In: *Circulation Research* 39.1 (1976), pp. 58–65. ISSN: 00097330. DOI: 10.1161/01.RES.39.1.58.

[122] D. A. Steinman. "Image-Based Computational Fluid Dynamics Modeling in Realistic Arterial Geometries". In: *Annals of Biomedical Engineering* 30 (2002), 483–497. DOI: doi.org/10.1114/1.1467679.

[123] P. H. Stone et al. "Effect of endothelial shear stress on the progression of coronary artery disease, vascular remodeling, and in-stent restenosis in humans: In vivo 6-month follow-up study". In: *Circulation* 108 (4 July 2003), pp. 438–444. ISSN: 00097322. DOI: 10.1161/01.CIR.0000080882.35274.AD.

[124] C. Strecker et al. "Carotid geometry is an independent predictor of wall thickness - A 3D cardiovascular magnetic resonance study in patients with high cardiovascular risk". In: *Journal of Cardiovascular Magnetic Resonance* 22 (1 Sept. 2020). ISSN: 1532429X. DOI: 10.1186/s12968-020-00657-5.

[125] M. A. Syed, S. V. Raman, and O. P. Simonetti. *Basic Principles of Cardiovascular MRI: Physics and Imaging Techniques*. Springer, 2015.

[126] A. Taebi et al. "Hepatic arterial tree segmentation: Towards patient-specific dosimetry for liver cancer radioembolization". In: *Journal of Nuclear Medicine* 60 (supplement 1 2019), p. 122. DOI: 10.1007/s00270-005-0227-5.

[127] T. R. Taha. *An Introduction to Parallel Computational Fluid Dynamics*. Vol. 6. 4. 2005, pp. 78–78. ISBN: 9780131274983. DOI: 10.1109/mcc.1998.736434.

[128] F. P. P. Tan et al. "Analysis of flow patterns in a patient-specific thoracic aortic aneurysm model". In: *Computers and Structures* 87.11-12 (2009), pp. 680–690. DOI: 10.1016/j.compstruc.2008.09.007.

[129] M. Tanaka et al. "Spiral systolic blood flow in the ascending aorta and aortic arch analyzed by echo-dynamography". In: *Journal of Cardiology* 56.1 (2010), pp. 97–110. ISSN: 09145087. DOI: 10.1016/j.jjcc.2010.03.008.

[130] O. Tanweer et al. "A Comparative Review of the Hemodynamics and Pathogenesis of Cerebral and Abdominal Aortic Aneurysms: Lessons to Learn From Each Other". In: *Journal of Cerebrovascular and Endovascular Neurosurgery* 16 (4 2014), p. 335. ISSN: 2234-8565. DOI: 10.7461/jcen.2014.16.4.335.

[131] C. A. Taylor and C. A. Figueroa. "Patient-specific modeling of cardiovascular mechanics". In: *Annual Review of Biomedical Engineering* 11 (Aug. 2009), pp. 109–134. ISSN: 15239829. DOI: 10.1146/annurev.bioeng.10.061807.160521.

[132] H. Tomita et al. "Relationship between hemodynamics and atherosclerosis in aortic arches of apolipoprotein E-null mice on 129S6/SvEvTac and C57BL/6J genetic backgrounds". In: *Atherosclerosis* 220 (1 Jan. 2012), pp. 78–85. ISSN: 00219150. DOI: 10.1016/j.atherosclerosis.2011.10.020.

[133] R.J. Traystman. *Primer on Cerebrovascular Diseases (2nd Edition)*. Academic Press, 2017.

[134] H. Tsukui et al. "coronary anastomosis provides lower energy loss in coronary artery bypass grafting". In: 32 (1 2013), pp. 83–89. DOI: 10.1007/s00380-016-0880-4.

[135] A. Vali et al. "Computational fluid dynamics modelingof contrast transport in basilar aneurysms following flow-altering surgeries". In: *Journal of Biomechanics* 50.12 (2017), pp. 195–201. DOI: 10.1016/j.jbiomech.2016.11.028.

[136] Y. Wang and S. Elghobashi. "On locating the obstruction in the upper airway via numerical simulation". In: *Respiratory Physiology and Neurobiology* 193.1 (2014), pp. 1–10. ISSN: 15699048. DOI: 10.1016/j.resp.2013.12.009.

[137] J. Warren, D. Manning, and J. Pennell. *Cardiovascular Magnetic Resonance*. Elsevier, 2018.

[138] A. L. Wentland, T. M. Grist, and O. Wieben. "Repeatability and Internal Consistency of Abdominal 2D and 4D Phase Contrast MR Flow Measurements". In: *Academic Radiology* 20.6 (2013), pp. 699–704. ISSN: 10766332. DOI: 10.1016/j.acra.2012.12.019. URL: http://dx.doi.org/10.1016/j.acra.2012.12.019.

[139] J. J. White and R. L. Dalman. "Gaining new insights into early abdominal aortic aneurysm disease". In: *The Permanente Journal* 12.2 (2008), p. 10. DOI: 10.7812/tpp/07-130.

[140] D. A. Wolf-Gladrow. "Lattic-gas Cellular Automata and Lattice Boltzmann Models: An Introduction". In: *New York: Springer* (2000).

[141] D. T. Wymer et al. "Phase-Contrast MRI : Physics , Tech- niques , and Clinical Applications". In: *RadioGraphics* 40 (2020), pp. 122–140. DOI: 10.1148/rg.2020190039.

[142] H. Xu, W. Zhang, and Y. Wang. "Explore missing flow dynamics by physics-informed deep learning: The parameterized governing systems". In: *Physics of Fluids* 33.9 (2021). ISSN: 10897666. DOI: 10.1063/5.0062377. arXiv: 2008.12266.

[143] Z. Xu et al. "A mesh quality discrimination method based on convolutional neural network". In: *2020 IEEE International Conference on Artificial Intelligence and Computer Applications (ICAICA)* (2020), pp. 481–486. DOI: 10.1109/ICAICA50127.2020.9182623.

[144] J. Zhong et al. "Fast Virtual Stenting with Active Contour Models in Intracranical Aneurysm". In: *Scientific Reports* 6.February (2016), pp. 1–9. ISSN: 20452322. DOI: 10.1038/srep21724.

[145] M. Ziegler et al. "Exploring the Relationships Between Hemodynamic Stresses in the Carotid Arteries". In: *Frontiers in Cardiovascular Medicine* 7 (Feb. 2021). ISSN: 2297055X. DOI: 10.3389/fcvm.2020.617755.

List of Figures

List of Tables

Acknowledgements

I would like to thank my supervisor, Prof. Martin Uecker, for his constant support and for giving me enough freedom to try out my ideas.

I sincerely thank the thesis committee: Prof. Martin Uecker, Prof. Ulrich Paritz and Prof. Susann Boretius. I thank them for monitoring my progress and helping me with scientific questions and personal matters.

I would like to thank the collaborators PD Dr. med. Michael Steinmetz and Dr. Yong Wang. Their expertise was very important for the completion of the project. Thanks to Dr. Mueed Azhar, Ansgar Adler for their help with the experiments.

Many thanks to all the members of our research group. The regular progress reports have broadened my horizon and given me many valuable experiences. Special thanks to Dr. Xiaoqing Wang, Martin Schilling, Guanxiong Luo and Yuxiao Luo for their valuable comments during the revision process of the thesis.

Finally, I would also like to thank my family and the friends I have made over the years for their unconditional support.